# Analysis of Multilayer Coatings by Electron Microscopy

Thesis submitted in accordance with the requirements of the University of Liverpool for the Degree of Doctor in Philosophy by Helen Jane Davock

**September 1998**

**Acknowledgements**

Primarily, I would like to thank Gordon Tatlock firstly for his time, encouragement and expertise. Secondly, for persuading me to study materials at Liverpool in the first place.

I would also like to thank all of the research group for their help and banter. Also, the Head of Department for the use of the facilities, EPSRC for funding and Peter Goodhew for his support.

The interest and skills of Rik Brydson and Bob Keyse have been essential for this research and are very much appreciated.

Many thanks to Walter Weaver and Penny Neal from BNFL Springfields for resurrecting this work with such interesting samples.

Many thanks are due to my parents and grandparents for their continuing love and support (especially of a financial nature) and Barry for his understanding and patience.

*For my Parents, Elise and John*

## Abstract

Multilayer coatings are currently creating much research interest, due to the vastly improved properties that they produce over their single layer counterparts. Two systems of multilayer coatings have been studied, primarily by using electron microscopy. Uniformity, microstructure, composition, interlayer interactions and, where possible, hardness have all been determined.

The first system analysed was $TiB_2$/Al, a very hard material paired with a relatively soft one. This coating exhibited a reasonable degree of uniformity and little interaction was found between the individual layers. However, the microstructure of the $TiB_2$ layers led to unexpected PEELS results and interpretation of these became one of the principal goals of this project.

Differences in the B K-edge spectra in $TiB_2$ exhibited a range of fine structure that had not previously been reported. It is thought that the combination of the textured film and the nm probe of the STEM enabled the variety of fine structures to be revealed. Effects of ion beam thinning, beam damage, thickness, impurities and orientation have been extensively studied. The orientation of the sample with respect to the electron beam in materials such as $TiB_2$, had previously not been considered significant. Data is presented to prove otherwise.

The second coating system to be examined was Cu/Al. These also produced unexpected results since alternating layers of pure Cu and Al were not found. Even more surprising was the discovery that coatings with different individual layer thickness had different compositions from each other. This result is very significant, since property data comparisons have been carried out between them previously. Multilayer coatings in the nm range are very difficult to categorise, but in this project it is shown that such analysis cannot be overlooked if meaningful comparisons are to be made about improvements in properties.

Hardness measurements, X-ray diffraction and a limited amount of differential scanning calorimetry were also used to characterise the films and interactions between them. The Cu/Al system was shown to be dominated by interfacial oxide films, formed during deposition.

## Publications

**PEELS Analysis and the Microstructure of $TiB_2$ /Al Multilayer Coatings.**
H. J. Davock, G. J. Tatlock, K. J. Lawson and J. R. Nicholls
*Proceedings 11th European Congress on Electron Microscopy (1996)*

**Factors affecting the ELNES of the boron K-edge in titanium diboride in a multilayer coating.**
H. J. Davock, G. J. Tatlock, R. Brydson, K. J. Lawson and J. R. Nicholls
*Electron Microscopy and Analysis Group Conf. EMAG97 (1997)*

**Identifying parameters controlling ELNES of bulk materials – a route to understanding bonding in nanoscale precipitates, interfaces and defects**
R. Brydson, A. J. Scott, K. Lie and H. J. Davock
*Proc. 14th International Congress on Electron Microscopy, ICEM (1998) Vol. 3, 605*

**Electronic structure of $TiB_2$: Orientation dependent ELNES and the effect of the core hole at the B K-edge.**
K. Lie, R. Brydson, H. Davock, *Phys. Rev. B, In Press*

**Analysis of Nanoparticles using STEM.**
H. J. Davock, P. J. Goodhew, A. Ibraheem, A. Papworth, J. Fink, R. Murray
*International Congress on Imaging Science, ICPS (1998)*

# Contents

# Figure List

## Chapter 1: Introduction



## Chapter 2: Literature Review



## Chapter 3: Experimental Methods

**Chapter 4: $TiB_2$/Al Results**



**Chapter 5: Cu/Al Results**

**Chapter 6: Discussion**

# *Chapter 1*

## *Introduction*

Chapter 1 provides a brief introduction to the history of coatings in general and then concentrates on the evolution of multilayers. What constitutes a multilayer coating is described along with reasons, why at present, there is so much research interest in this topic. The primary objectives of this project are also discussed along with collaborations with other research groups in an attempt to achieve them.

§

## 1.1 Why Coat?

Surface coatings have evolved and developed significantly over the years. This is due to continuing interest and research, as a consequence of demand from the many differing fields of science and technology that utilise such products. From microelectronics to the home improvement industry, they all use coatings for a variety of reasons that include better properties, an aesthetic finish and a cheaper cost for similar or improved quality. It is the financial benefits that have ultimately driven industry to strive for new and improved coating technology. For example, as far back as 1920, the estimated cost of wastage due to the corrosion of the world's iron and steel was £700,000,000 [1].

Early types of coatings must include printing and painting. This technology has progressed over many years to produce a wide variety of different coatings for very different applications. For instance, during the Gulf War, Tornado fighter jets were subjected to hostile environments on a regular basis, that they had not previously encountered i.e. sand. This increased the wear on certain parts of the aircraft. Research into high impact and wear resistant coatings to avoid such occurrences could save millions of pounds.

The fact that some kitchen knives can stay sharp for 25 years, is also due to high performance coatings. A hard film, such as TiN, is coated on one side of the blade. As the blade is used, it is the softer steel side that wears away towards the coating, hence maintaining the sharp edge.

Some of the many different kinds of coatings are described below:

## 1.2 Types of Coatings

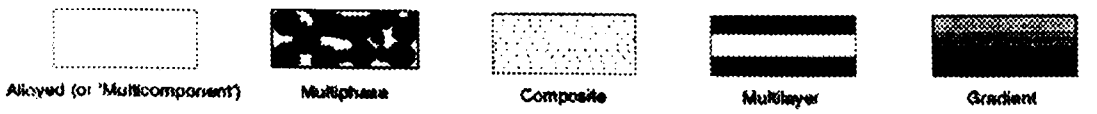


*Figure 1.1:Various types of coating [2]*

The simplest type of coating is a single layer of a material whether alloyed or not. An example of this is the galvanising of steel by coating with a layer of zinc. Zinc is actually more active than steel and hence is a sacrificial layer, however the corrosion product of zinc oxide can itself stifle further reaction. The white colour of zinc oxide is also considered preferential to the rust colour of iron oxide [1].

Single layer films are used for a multitude of reasons, aesthetic, prevention of corrosion and in the case of Schulz *et. al.* [3], for the prevention of wear

on tools. Hard TiN coatings on such articles have been the object of much research over recent years [4, 5].

However, no coating of this form can have all the properties at the highest level. For instance, if hardness is to be at a maximum, then brittleness cannot usually be avoided [2]. This has led to a growing interest over the years, to combine several materials to create a film with optimum properties.

Multiphase, composite, multilayer and gradient coatings are all different kinds of coating but with one common theme. They all consist of a combination of phases to try and produce an optimum coating for its particular application.

Multiphase and composite coatings are very similar. A composite coating is when one phase is dispersed in a matrix of another. In multiphase coatings, both of the phases are equally present and neither is continuous [2].

Dullaire *et. al.* [6] studied composite coatings of TiC particles dispersed in an Fe matrix to produce films that were more resistant to crack propagation than the TiN ceramic, but still with impressive wear

resistance. Also cited were examples of multiphase coatings which still included the combination of a hard ceramic with a metallic phase, but in equal proportions e.g. $TiB_2$-Fe and TiC-Fe.

Even though multilayer and gradient coatings combine phases, as with composite and multiphase, they differ in that they both change composition *through* the depth of the coating. The transition in composition is gradual in gradient coatings, but distinct and periodic in multilayers. An example of a gradient coating is TiN/TiCN/TiC [2]. A typical multilayer coating is W/WC.

### 1.3 . Birth of Multilayers

In recent years it is multilayer coatings that have produced much interest, with many research groups pairing various materials on differing substrates. This has been in an attempt to achieve improved properties over their single layer counterparts.

The idea of pairing layers together to achieve better coatings is not a new one. Bond coats were perhaps the birth of *multiple* coatings. A layer is pre-coated on a substrate to enable the main layer to adhere more effectively. A classic example of such is a paint primer. Another example

of pairing layers is Ti/TiN [7]. Many double or triple layer coatings have been, and still are, subjects of research projects.

However it is the combination of pairs of layers repeated periodically, often hundreds of times, which produce *multilayer* coatings as we now know them. It is the particular combination of the materials and the individual layer thicknesses, which are thought to contribute to some of the vastly improved properties that have been reported. This is especially thought to be the case when such layers are in the nm thickness range.

## 1.4 $TiB_2$/Al Multilayer Coatings

The concept behind the pairing of these two materials was the combination of a very hard material with one that is relatively soft. The objective was to produce a novel wear resistant coating for possible use in aircraft. Very hard materials such as ceramics are good in wear applications as coatings, as long as they remain attached to the substrate. Unfortunately hard materials are invariably, also very brittle. Combined with a ductile material, such as aluminium in a multilayer coating, it is hoped that some of these problems can be overcome. Any cracks that form in the hard layer are thought to be deflected at the interface. Even if

a layer is totally removed, it is not catastrophic. There are still many more below.

## 1.5 Cu/Al Multilayer Coatings

If the principle behind $TiB_2$/Al coatings is to pair very different materials, the same is certainly not the case for Cu/Al coatings. In comparison to $TiB_2$/Al the physical properties of Cu/Al are very similar indeed. However, if the goal is to try and establish reasons for the improved properties of multilayer coatings (such as lowering the individual layer thickness) then cheap, widely available materials that are simple to coat, such as Cu and Al, are ideal. These samples were made at Salford University for BNFL.

## 1.6 Objectives

The initial objectives of this project were to study the microstructure and composition of $TiB_2$/Al multilayer coatings. These results were then to be compared with property measurements taken at Cranfield University, who also produced the samples. The ultimate goal was to tailor the individual layer thickness and microstructure to produce the best performance out of this system. Unfortunately it became apparent that

these goals could not be achieved at Cranfield in the time available, hence the aims changed direction to studying $TiB_2$ itself, especially using Parallel Electron Energy-Loss Spectroscopy (PEELS).

Later on in the project some Cu/Al coatings, with varying individual layer thicknesses became available to enable some of the initial objectives to be achieved on this different multilayer system. In fact, the acquisition of these samples also provided an interesting comparison to the $TiB_2$/Al system. The coatings were made by different magnetron processing methods and use a relatively soft aluminium layer combined, in one case with hard $TiB_2$ and the other, relatively soft Cu layers.

§

# Chapter 2

## *Literature Review*

Chapter 2 consists of a review of literature relevant to this project. It starts with processing methods and equipment used in the production of coatings, multilayers in particular. Another important aspect to consider is the formation of microstructure in coatings produced by such methods. This is followed by a section dedicated to multilayers themselves including theories to attempt to explain the vast mechanical property improvement seen. A large part of this work has involved the interpretation of EELS data and hence it was deemed necessary to consider other findings in this field. Finally the structure and properties of the specific materials used in the multilayer coatings are reviewed.

§

## 2.1 Processing

Even though the processing of coatings has been beyond the objectives of this project, it is imperative to have an appreciation of what is involved. The method of processing chosen and parameters used, ultimately influence the form of the resulting film. There are many methods that can be used for depositing multilayer films, including arc evaporation, chemical vapour deposition (CVD) and ion plating. However, one of the most popular, and for the basis of this project the most relevant, is physical vapour deposition (PVD). Magnetron sputtering is the PVD method that has been used to form both of the multilayer systems in this project. This section outlines the principles of such methods and the effects of tailoring various parameters.

### 2.1.1 Principles of Sputter Deposition

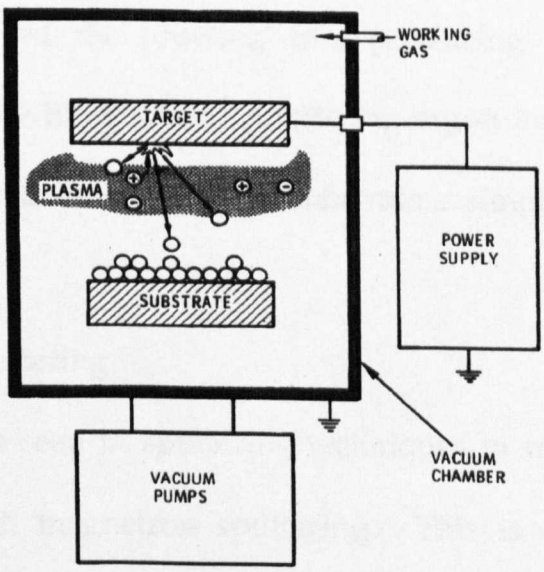


*Figure 2.1: The basis of sputter deposition [8].*

The basis of sputter deposition involves the removal of material from a target to produce a coating on a substrate. The whole system is contained in a vacuum chamber and initiated by a sputtering gas that provides a medium for a plasma to be maintained. An inert gas such as argon is usually used for such a task, although xenon is an alternative. The target has a negative voltage applied to it (either DC or RF). Subsequently, argon ions from the plasma are accelerated towards the target and remove the coating material either as ions or as atoms. These can then in turn deposit on the substrate surface.

The substrate can be kept under a number of conditions: grounded, floating or biased. *Floating* is when the substrate is not earthed and the number of electrons and ions reaching the substrate is equal. No current flows and the substrate has a self-potential. *Biased* is when a large negative voltage is applied to the substrate, sputtering ions are strongly attracted and bombard the growing film producing a much denser coating. However the likelihood of sputtering argon into the coating is greatly increased. *Grounded* is when the substrate is simply earthed [9].

### 2.1.2 Magnetron Sputtering

Many improvements seen in sputtering techniques in recent times have been associated with magnetron sputtering. This is due to the high number of industrial users that this method attracts. Such industries

include magnetic recording, solar, microelectronics and metallurgical coatings [10]. However, more improvements can be made. This is especially so in reducing the cost and the reliability of the coating as highlighted by Window [11].

Magnetron sputtering offers many advantages over other sputtering methods and coating techniques. Firstly the deposition rate is high and produces very uniform layers. Bombardment of the film occurs during the process, which can result in more dense films [11], fewer voids and a preferred texture [10] (this is especially important with a low temperature process such as PVD). Stress is also created which can increase the hardness of the film. However, for thicker films this can result in delamination [11].

### 2.1.2.1 Types of Magnetrons

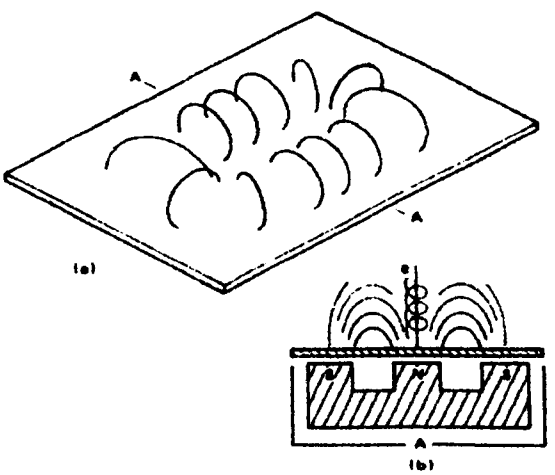

*Figure 2.2: A typical magnetron showing field lines [12].*

A typical magnetron is illustrated in Figure 2.2. It consists of a water-cooled target connected to an array of magnets arranged in such a way as to produce a field as shown. This magnetic field confines electrons within the

plasma close to target hence increases the ionisation of the sputtering gas in this region by two orders of magnitude. Subsequently magnetron sputtering can operate with a lower gas pressure (0.1-0.2 Pa [12]). This produces a correspondingly improved deposition rate, both from an increase in the material removed from the target, and the ease with which it can travel to the substrate. This latter effect is due to the lower operating pressure, which results in fewer collisions. The cathode voltage can be around -500V with respect to the anode. Ions in the plasma are accelerated towards the target removing material and creating secondary electrons, which are trapped by the magnetic field and produce more ionisation before reaching the anodes.

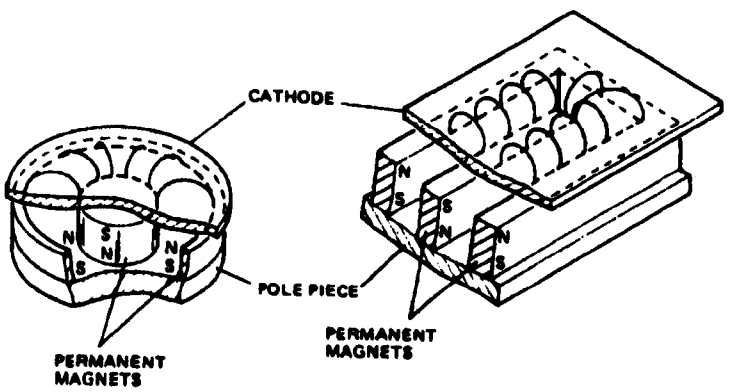


*Figure 2.3:Circular and rectangular sources [12].*

Typical magnetrons are usually rectangular or disc-like (Figure 2.3). A disadvantage of magnetron sputtering is the uneven erosion of target material as most material is removed only from the region where the magnetic field resides.

### 2.1.2.2 RF/DC

An advantage of a DC magnetron is the control that is achieved over the amount of bombardment on the growing film by changing the unbalance. However, DC is only of use for conducting targets. In the case of an insulating target problems arise. This is because DC on an insulating target can result in charging because electrons will collect on the target surface. Subsequently Ar ions will not be attracted to the target and sputtering will cease. For such insulating targets a RF source is used. RF is a type of AC current but at radio frequency.

At 50Hz the mains frequency gives time for electrons to accumulate on the surface. However, this is overcome by using a RF power supply since a plasma is produced throughout the chamber and hence high bombardments are achieved. Unfortunately these are difficult to tailor, in contrast to DC methods [13]. The energies of energetic neutrals are reduced in comparison to DC (due to lower cathode potential) hence there is less chance of inert gas incorporation in the film.

### 2.1.2.3 Inert Gas

Inert gas atoms constantly bombard the substrate whilst the film is growing. However the energy of such atoms is usually <1eV and has little effect on the film growth. Only atoms with large amounts of energy can affect the film. These are called energetic neutrals. They are usually

caused by the inert gas being considerably lighter than the sputtering atom. In such a case when the gas ion hits the target, there is an increased chance of it being neutralised and reflected back with a significant amount of energy and affecting the growing film. Such effects are likely to be overcome by using a heavier gas; xenon has been used to account for this effect. However because the expense is greatly increased for xenon, argon is the most common inert gas used [10].

### 2.1.2.4 Balanced Magnetron Sputtering

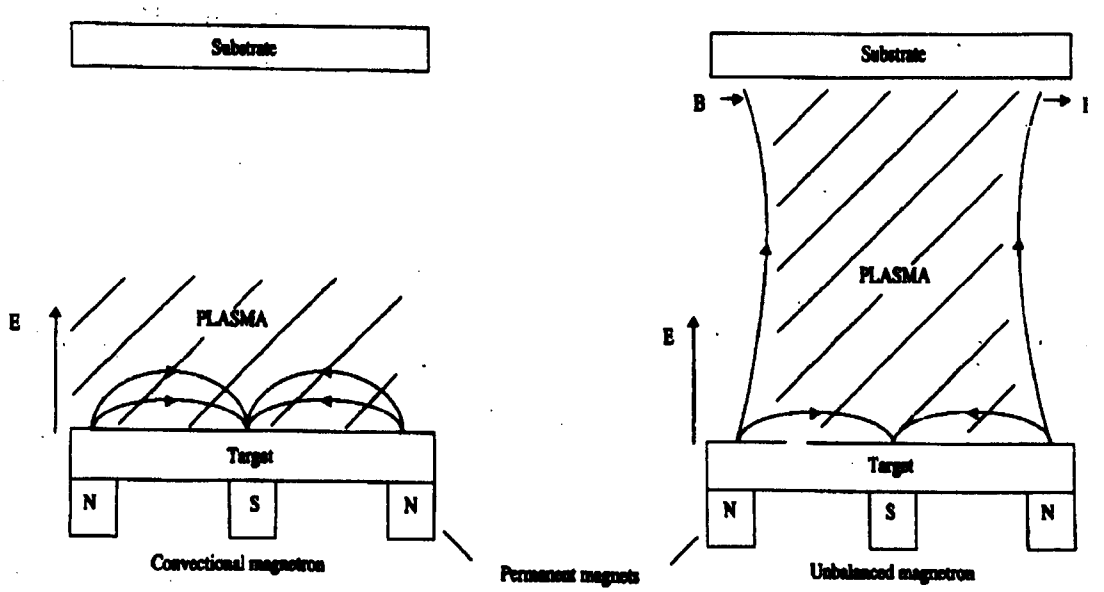


*Figure 2.4: (a) Balanced magnetron sputtering (b) Unbalanced magnetron sputtering [9].*

Figure 2.4(a) [9] shows the principle of balanced magnetron sputtering. The plasma is held very close to the substrate and may only extend 6cm from the target. A substrate that lies outside this region may not be

subjected to enough ion bombardment, which can modify the growing film and produce films of inferior quality. This can be overcome by using unbalanced magnetron sputtering.

#### 2.1.2.5 Unbalanced Magnetron Sputtering

In an unbalanced magnetron (Figure 2.4 (b)) the outer magnets are strengthened so that the magnetic field is not purely confined to the region close to the target but also flows out towards the substrate [14]. Now a dense plasma is created between the target and the substrate, as well as in the region close to the magnetron. The close target field is still present to confine secondary electrons but is not as strong as in the balanced magnetron. Some do escape and follow the magnetic field, bombarding the film growing on the substrate. As neutrality must be maintained, ions and electrons simultaneously cause bombardment of the film.

For this reason the substrate is no longer restricted to being positioned in regions so close to the target. High quality films are still produced at up to 20cm from the target, allowing a greater range of shapes to be coated [9]. Hence, unbalanced magnetron sputtering is more attractive to industry due to its versatility, greater deposition rates and the high levels of bombardment on the growing film [15].

### 2.1.3 Magnetron Techniques for Multilayer Coatings

One of the attractions of magnetron sputtering is that a number of targets of differing materials can be contained within the coating system. This allows the rapid production of multilayer and multiphase coatings.

Figure 2.5 is an example of an unbalanced arrangement of magnetrons for producing a multilayer coating. The substrate table rotates and in so doing, a layer of material is put down every time the substrate passes an individual target. Therefore the thickness of the individual layers within such a multilayer coating can be tailored according to the power applied to the individual targets and the rotation speed of the table. Shutters are included in some cases to prevent cross contamination [16]. Other users turn off the non-coating target when alternate layers are deposited [17]. The table does not have to continually rotate and the individual thickness is then determined by the length of time in front of the magnetron before it is turned to the other.

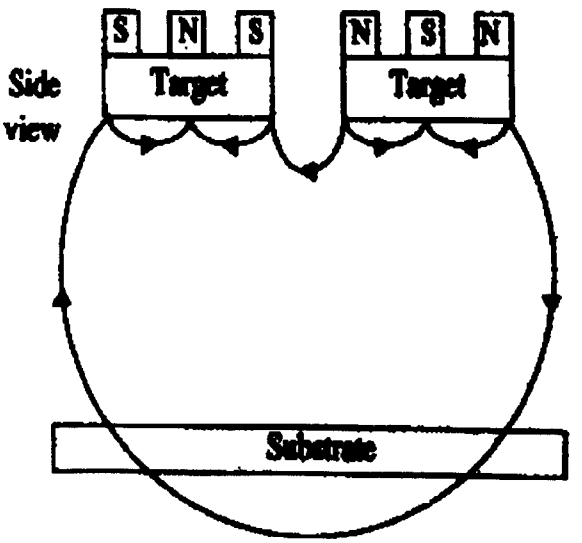


*Figure 2.5 Dual magnetrons for co-deposition [9].*

These techniques can be used for more than two targets. This situation is much more complex and such a system has negatively biased surfaces at the top and bottom of the coating chamber to reflect any electrons, which come from each end of the magnetic trap [11].

Rotatable magnetrons have been used [10]. The magnet is stationary whilst the target rotates over it. This method is large-scale and is advantageous for reactive gas methods, due to the continual cleaning of the target as it traverses through the sputter region. Any build-up of contaminates around the sputtering region that would usually be associated with such a method is reduced and hence so is the possibility of arcing [10]. Also the wastage of the target would be reduced.

§

## 2.2 The Microstructure of PVD Coatings

The microstructure formed within the growing film ultimately determines the properties. In this section, theories predicting the type of microstructure developed are examined along with processing parameters that can affect it. The consequences of the choice of substrate, additions of bias to the substrate and texture formation are also considered.

One of the overriding factors in producing a distinctive PVD microstructure is that the sputtered target material approaches the substrate from a limited set of directions. As a result of this, the film usually grows in the form of columns that are perpendicular to the substrate. This structure is illustrated in Figure 2.6 [18].

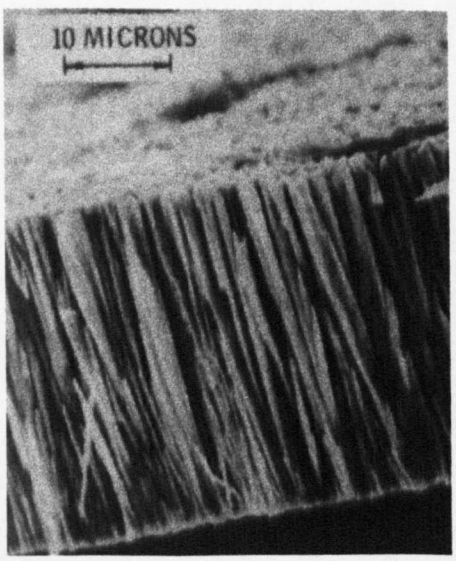


*Figure 2.6: Sputtered chromium <110> [18].*

This anisotropic microstructure has a substantial influence over the properties of such thin films [19]. It has been reported that PVD coatings are significantly harder when tested parallel to their growth direction compared with values derived from the other two orthogonal directions [20]. However, such a microstructure has disadvantages

as well. It gains an ability to absorb or desorb moisture from the atmosphere. Also such distinct columns can provide fast diffusion paths throughout the structure [21]. Apart from the angle of deposition, this kind of processing is also sensitive to temperature, pressure, the inert gas used, the rate of deposition, the target materials, as well as the substrate chosen. Any slight variation of any of the deposition conditions can have a profound effect on the microstructure and hence the resulting properties [19].

### 2.2.1 Structural Zone Models

Many attempts have been made to model film morphology but as yet it is impossible to predict the properties of vapour deposited coatings, from knowledge of their deposition conditions alone [22].

Little is understood about the formation of the microstructure in thin films, despite many theoretical models proposed in the last thirty years.

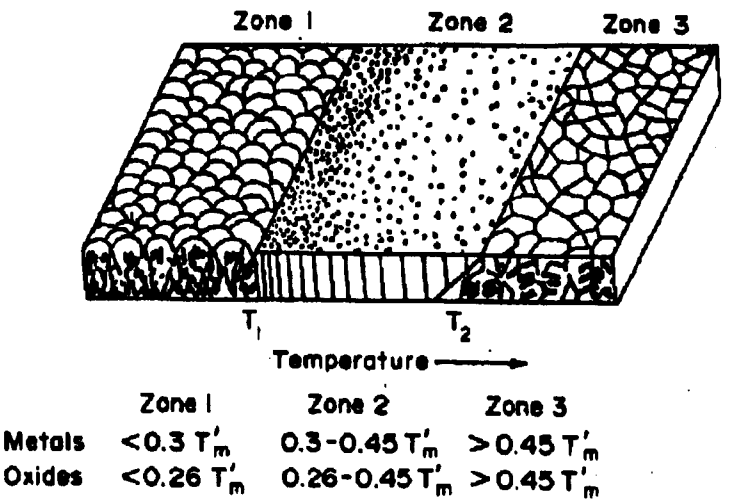


*Figure 2.7: Original Zone Model by Movachan and Demchishin [23]*

In 1969, Movachan and Demchishin [23] were the first to classify such microstructures in a Structural Zone Model (SZM) as shown in Figure 2.7. Three distinct zones were classified: zones 1, 2 and 3.

These were characterised by taking the ratio of substrate temperature, (T), to the melting temperature of the sputtered film, ($T_m$), where the temperature is expressed in Kelvin. The main drawback of this original model was that it only considered pure metals. In 1977, Thornton [24] rectified this, he not only used different materials, but also considered the sputtering gas used. Thornton found the actual temperatures needed to achieve a certain structure was higher

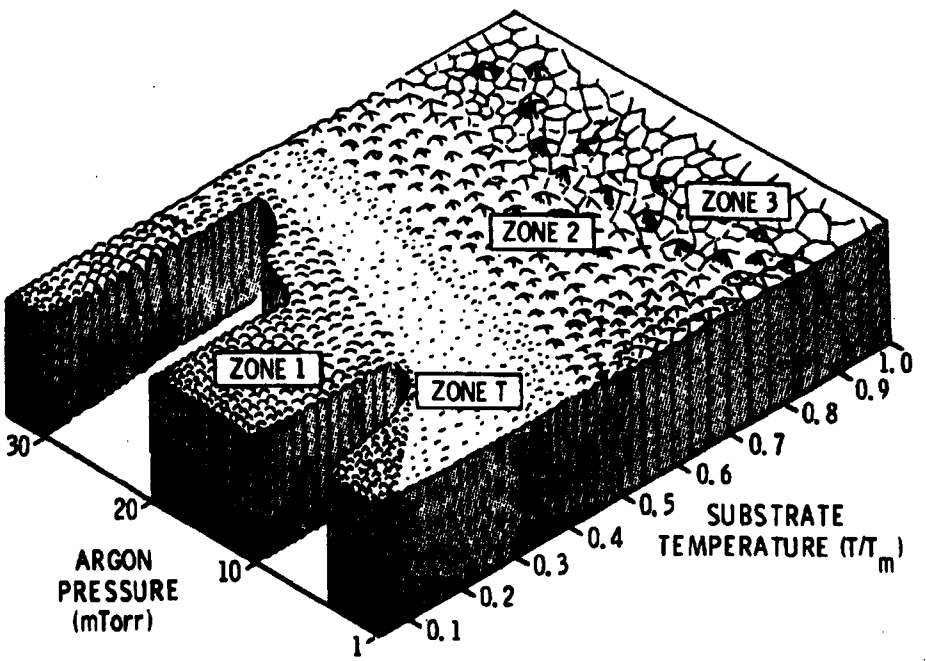


*Figure 2.8: Structural zone model by Thornton [24].*

than originally suggested, due to an increase in gas pressure. Even so, these temperatures are only guidelines, as the transitions are not considered abrupt. Figure 2.8 shows Thornton's model.

Another zone was also added, known as zone T, which consists of poorly defined, fibrous grains. The four zones defined by Thornton are described below: -

**Zone 1($T/T_m$ < 0.25-0.3)**

Zone 1 structure (shown in Figure 2.9) corresponds to having little adatom mobility, due to the low temperature. It consists of tapered columns with domed tops, due to the limited number of nuclei. It has a high level of residual stress and a high dislocation density [18].

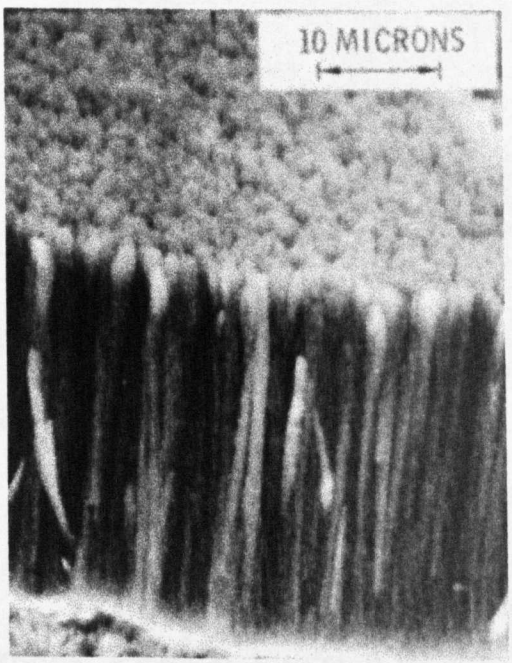


*Figure 2.9: Zone 1 sputtered aluminium <100> $T/T_m$ =0.08[18]*

**Zone 2 ($0.3<T/T_m<0.5$)**

In zone 2 (Figure 2.10) surface diffusion becomes more important. The structure has a full density of a straight columnar morphology, with a smoother surface topography. The grain size increases with condensation temperature.

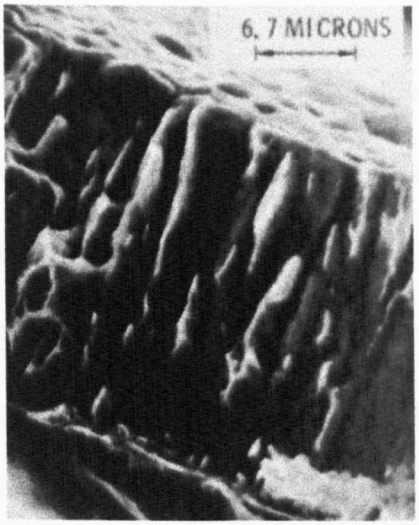


*Figure 2.10: Zone 2 copper <110>T/Tm= 0.5 [18]*

**Zone 3 ($T/T_m>0.5$)**

At even higher temperatures, the structure goes to a fully equiaxed grain morphology (Figure 2.11) as bulk diffusion becomes the dominant transport process. This structure can not always be seen in high melting temperature

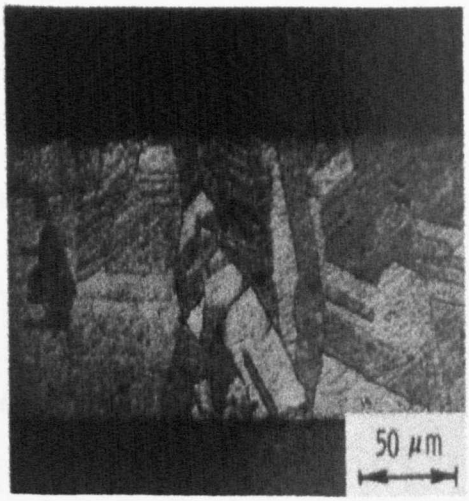


*Figure 2.11: Zone 3 copper [8]*

**Zone T**

Figure 2.12, consists of small fibrous grains that are poorly defined but dense, and hence do not suffer from the void problems that can be seen with a pure zone 1 structure.

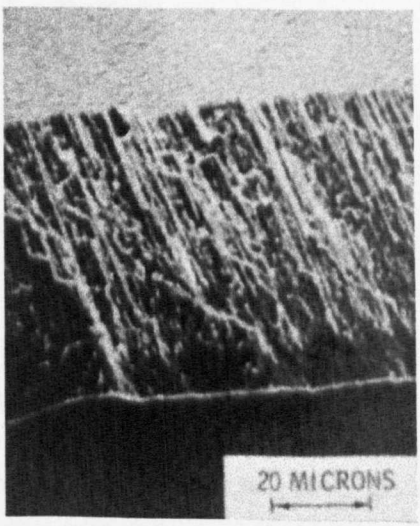


*Figure 2.12: Zone T copper <111> T/Tm=0.2 [8]*

### 2.2.2 Effect of Processing Parameters

Putting a bias on a substrate as described in section 2.1.1, increases the bombardment of the growing film. If the bias is large enough the momentum exchange causes coating atoms to fill voided boundaries. Therefore zone 1 structures can be overcome and zone T type structures are formed. However increasing the bombardment by using a bias creates higher energy gas ions, which can be trapped within the growing film [8]. Messier *et. al.* [25], suggested improvements to the SZM's to also consider the effect of the growing film thickness, temperature and bombardment. In this model (Figure 2.13) all the levels of column-void sizes are considered and collected in sub groups 1a, 1b, 1c, 1d and 1e.

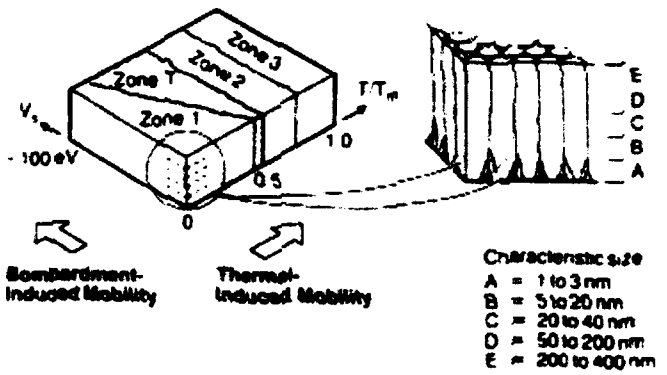


*Figure 2.13:Messier's SZM improvements*

This model shows that with increasing ion bombardment the unattractive zone 1 structure can be avoided, and a denser zone T structure is formed. Such improvements in the resulting microstructure can also be achieved by thermal induced mobility. Void filling is thought to occur not only by the coating of atoms into such regions, but also by impact induced surface

diffusion and local heating in the region, allowing recrystallisation [26, 27].

### 2.2.3 Effect of Substrate on Microstructure

One important factor that is left out of the SZM's is the effect of the substrate material. The type of substrate can be fundamentally important, not only can it dictate the size and orientation of grains in the growing film, but it is also crucial in determining the amount of stress contained within the coating [28, 29]. It is the degree of mismatch between the expansion coefficients of coating and substrate that determines whether such stresses are tensile or compressive. Such a stress will have a profound effect on the growing film in terms of microstructure, porosity and adhesion [19]. Almost all sputtered coatings are in a state of stress [8]. Such stress is usually greater for high melting point materials.

### 2.2.4 Texture in PVD Coatings

Texture is when there is a preferred orientation of growing crystallites. The development of texture that occurs in all zones (apart from equiaxed zone 3) is of major importance when attempting to relate the microstructure to the properties. For types 1, T and 2 the microstructural-induced anisotropy, which develops during growth can result in vastly

improved physical properties. The development of texture in PVD coatings occurs in three stages [28].

- *Nucleation-* Sputtered material from the target nucleates on the substrate. The form of such crystallites in terms of size and orientation is determined by the processing parameters and the nature of the substrate.
- *Competitive growth-* specifically oriented nuclei will grow faster than other crystallites but are not necessarily in the majority.
- *Steady growth-* a steady state of growth will occur when the film achieves its preferred direction of growth.

An additional factor that must be considered in the microstructural development of PVD films, is that the structure becomes less dense as it grows outwards. Consequently, thicker coatings of otherwise similar materials, might appear softer than thinner coatings since the indentation will be sampling greater porosity [20, 30].

§

## 2.3 Multilayer Coatings

Although research into multilayer coatings is a relatively new field there are many groups studying a wide variety of systems. This section describes improvements in properties that have been reported along with theories to attempt to explain such phenomena. The rôle of the interfaces between individual layers, growth and interactions are also addressed.

### 2.3.1 Improvements in Properties

There are many reported improvements for a number of properties in multilayer coatings of varying systems. This section highlights such improvements with respect to the materials used, microstructure, the period and thickness of the layers and the load used.

The importance of the period of the layers was shown by Setoyama *et. al.* in 1996 [31]. A clear dependence of the hardness performance of TiN/VN multilayers was reported. This is shown in Figure 2.14. Knoop hardness tests were used with a light load of 50g. Such a light load was used to try and eliminate the contribution to the hardness resulting from the substrate. To further account for this possible error, the overall thickness of the multilayer was grown to 1.3μm.

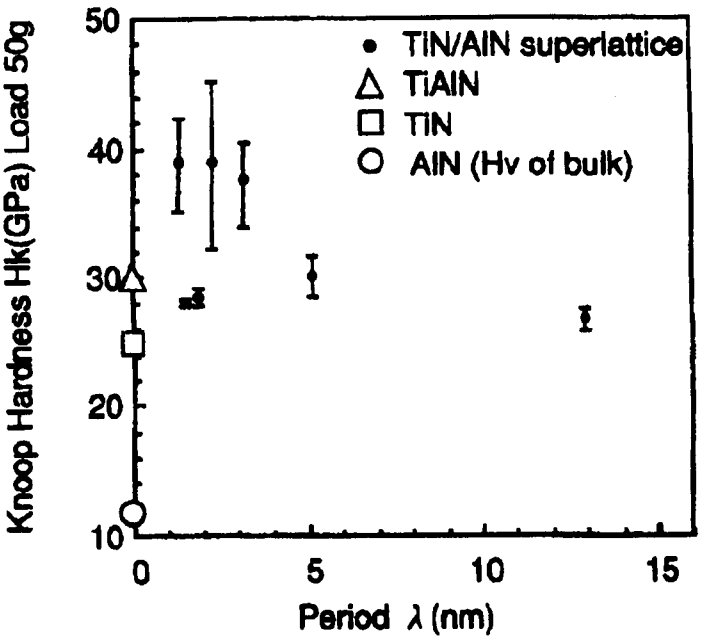


*Figure 2.14: Hardness results with respect to individual layer thickness [31].*

The improvement in hardness illustrated in Figure 2.14 is approximately twice the value that would be obtained for either of the individual layers as a single phase coating.

In 1989 Ruff *et. al.* [32], found an increased wear resistance in multilayers of Ni/Cu. This improvement was also concluded to be as a result of the individual layer spacing of the multilayer. Earlier work [33] on single layers showed that the nickel had double the wear resistance of copper. However, all of the multilayer samples tested showed an improvement on single layer values. In 1991, this original work was modified when

studies were carried out with even smaller layer thicknesses than those used previously i.e. 3.8 nm. Wear results on the varying thickness multilayer coatings is shown in Figure 2.15 [34].

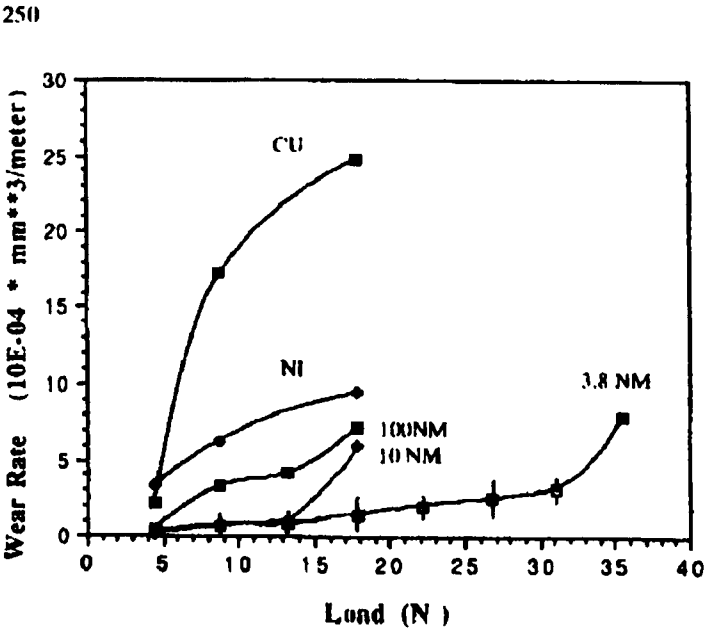


*Figure 2.15: Wear rate vs. load for various multilayer coatings and their single layer counterparts [34].*

All of the multilayers out perform the single coatings and a clear dependency is shown between the individual layer thickness and performance. However, it is thought that below a critical individual thickness the critical load changes from a standard Hall-Petch type dependence $(size)^{-1/2}$ to a $(size)^{-1}$dependence.

It is not just coatings with a large number of layers that exhibit improvements. Yang *et. al.* [35] in 1996, looked at $TiB_2$/TiN double layers, to combine what they define as the hardest metallic material in $TiB_2$ with a tougher (less brittle) hard coating like TiN. In fact there is a raging debate into whether $TiB_2$ is metallic or not and this is discussed in Section 3.6. However this research does highlight the fact that even just a double layer with one interface showed an increase in wear resistance. This improvement proved to be totally independent of which layer was on the surface.

Even though Yang *et. al.*, [35] established an improvement in wear resistance with just a single interface, Holleck *et. al.*, [36] gave strong evidence for the relationship between crack resistance and the number of interfaces that were contained within the total coating (Figure 2.16).

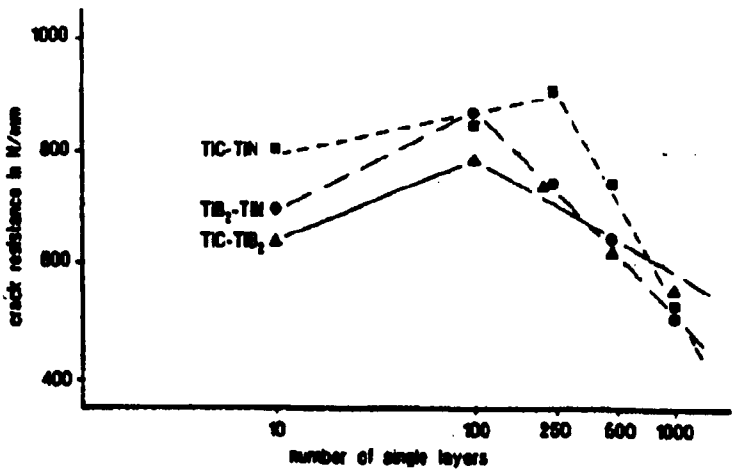


*Figure 2.16: Crack resistance vs. number of layers*

They suggested that there could be an optimum number of interfaces for maximum performance. Evidence for this was cited in terms of a multilayer coating ($TiB_2$/TiC) in which the optimum number of layers seemed to be about 100. This was explained in terms of crack deflection and energy dissipation at the phase boundaries. They suggest that there is a decreasing resistance as the number of interfaces increases past 100, due to the increasing volume of amorphous interface structure. These theories were modified in 1991 [37] when TEM investigations showed no interface zones.

Quesnel *et. al.*, [38] studied the erosion performance of W/WC multilayers. They found a clear dependence on impingement angle of the test to the performance of the layers. However regardless of the angle of the tests they too found that the thinner individual layer thicknesses produced the best performance.

In contrast Barzen *et. al.*, [39] when studying $Cr_3C_2$/SiC multilayers found that a thicker set of layers performed better. Below an individual thickness of 10nm comparatively poor results were obtained. However this was thought to be as a result of the interface zone becoming more significant.

Larsson *et. al.*, [40] related the improvements in a TiN/NbN coating to the relative amount of NbN. Figure 2.17 shows that as the amount of NbN increases so does the hardness. The HSS (high speed steel) and CC (cemented carbide) references in the key refer to the substrate of the multilayer. The 10/5 multilayer (10nmTiN/5nmNbN) exhibited the highest hardness and also had the most individual layers.

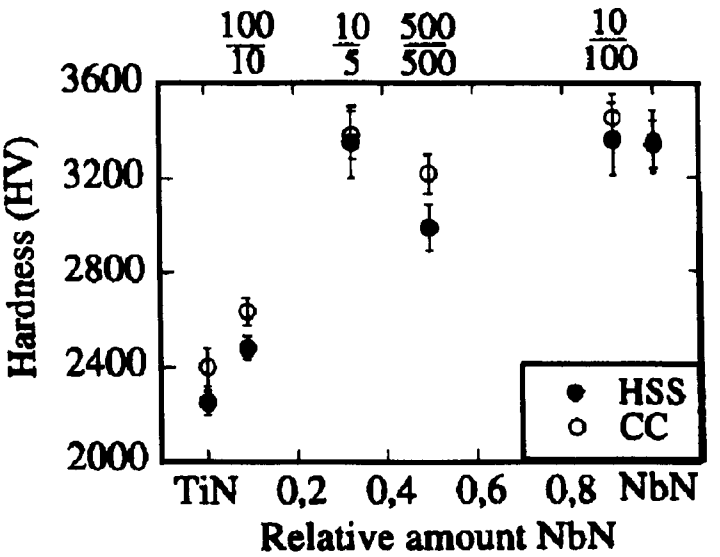


*Figure 2.17: Hardness with respect to the quantity of NbN.in TiN/NbN [40].*

Hubler *et. al.*, [41] is one of few to report discouraging results for multilayer coatings. Figure 2.18 shows the TiN single film as the harder coating as compared to Ti/TiN multilayers (with individual layer thickness <100nm). An increased content of Ti within the multilayer proved detrimental.

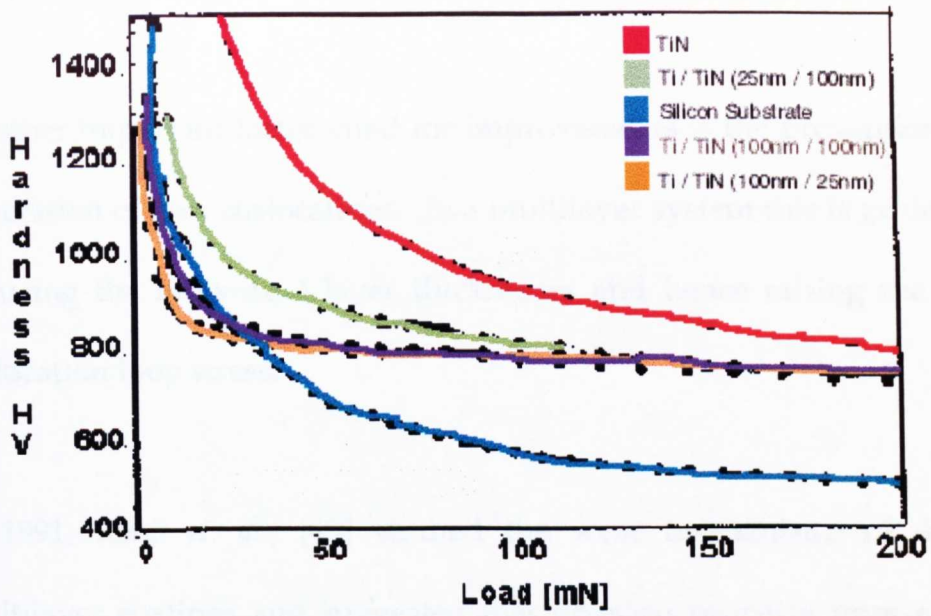


*Figure 2.18: Illustrates the superior hardness of a single TiN layer compared to multilayers [41].*

### 2.3.2 Effect of the Interface

In 1970, Koehler [42] suggested that *'a multilayer system of two suitable metals should have a resistance to plastic deformation greater than that from the same metals in a homogenous state'* and credited the improvement to energy barriers to dislocation movement formed at the interfaces.

To enable plastic deformation to take place dislocation glide and multiplication on a large scale is needed. Incoherent alternating layers of differing materials provide glide mismatch. As a result, glide dislocations are pinned by interfacial dislocations giving strength by the enhanced resistance to dislocation movement.

Another important factor cited for improvements is the prevention of the generation of new dislocations. In a multilayer system this is achieved by reducing the individual layer thicknesses and hence raising the critical dislocation loop stress.

In 1991, Renji *et. al.,* [43] studied the wear mechanisms of differing multilayer coatings and suggested that physical property improvements come from the removal of material layer by layer; any cracks that form are said to be deflected at interfaces.

The importance of crack deflection at interfaces was also reported by Holleck *et. al.,* [44] as they attempted to explain increased wear resistance in TiC/$TiB_2$ coatings ( Figure 2.19).

Other explanations for crack deflection at interfaces include; in very thin layers (sub 10nm) higher proportions of atoms lie close to the interface [45] and a charge transfer effect between layers [34]. Such multilayer interfaces are also thought to effect dislocation movement in a similar way to that of orientation change at grain boundaries [46].

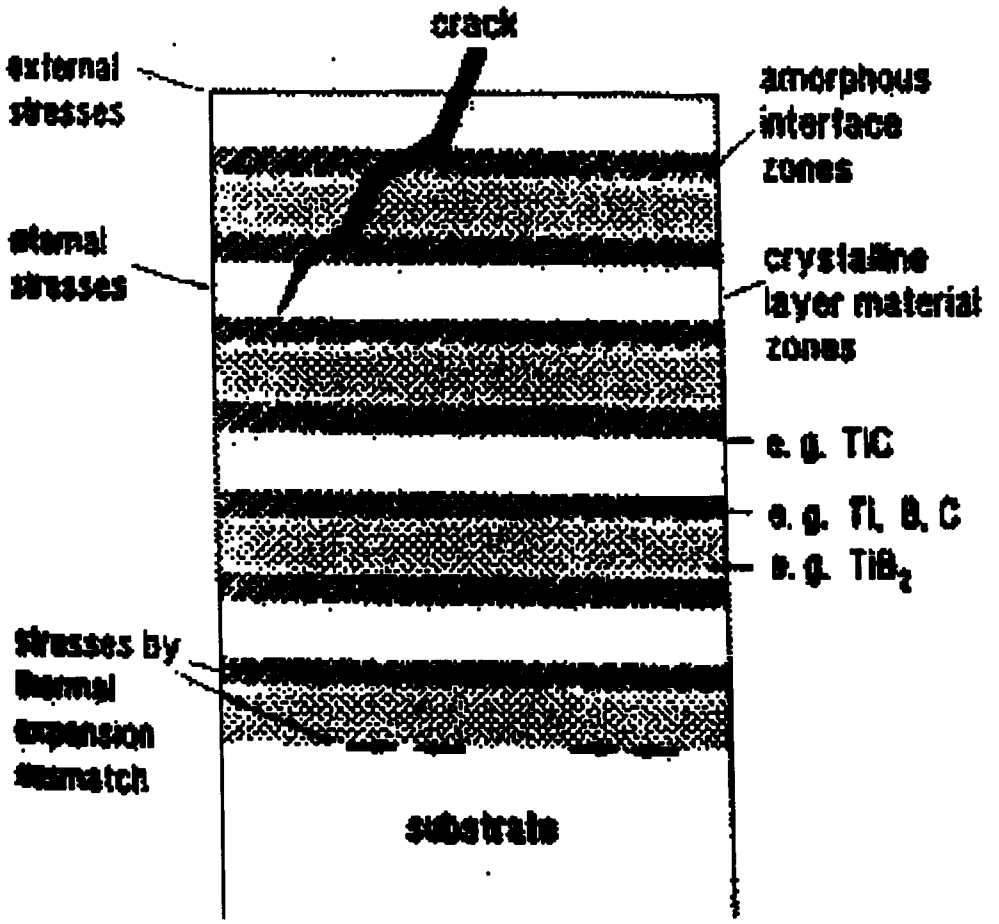


*Figure 2.19: Crack deflection in multilayer coatings [44]*

### 2.3.3 Growth of Multilayers

Setoyma *et. al.*, [31] carried out work on several coatings of AlN/TiN with differing periods. It was found that in the coating with a very small period of 3nm, the AlN adopted the NaCl crystal structure, usually only achieved at very high pressures. Such a structure was coherent with the NaCl structure of the TiN. However, this unexpected structure of AlN was not adopted for the larger periods such as 35nm where the usual wurtzite form was seen.

Cawley *et. al.*, [47] highlighted the difficulties in imaging the columnar grain boundaries and also showed evidence of columns that are carried throughout many layers. In agreement with the work of Setoyma *et. al.*, [28] they found this with the small period coatings at only 2.6 nm.

Cawley *et. al.*, [47] also showed PEELS analysis from both layers in a ZrN/TiAlN multilayer to try and establish whether there was any intermixing of the individual layers. Differences in the fine structure are seen in the nitrogen edge, indicating that the nitrogen present in the two layers was bonded differently.

Holleck *et. al.*, [36] showed that when sputtering $TiB_2$ onto either TiC or TiN an intermixed boundary is formed. It was established that $TiB_2$ grows in an amorphous state for 5nm on the carbide/boride mixed phase and for 10 nm on the nitride/boride mixed phase. Hence it was concluded that consequently there might be strong lattice distortion.

In the case of a $TiB_2$/TiC multilayer (both individual layers ~20nm) the TiC layers are epitaxial in the {111} planes and $TiB_2$ layers are partially crystalline. However if the $TiB_2$ layers are reduced to 5 nm then the crystallinity is lost and the structure is amorphous. This then has little

influence on the nucleation of the subsequent TiC layers, which now grow in the <200> direction.

Holleck *et. al.*, [36] also did work on sequential (using a continually rotating substrate table) coatings of TiC/$TiB_2$, $TiB_2$/TiN and TiC/ TiN with differing numbers of layers ranging from 10-1000 but all with a final coating thickness of 5 μm. It was found that epitaxial growth occurs for TiC on the hexagonal mixed boride phases to about 20 nm when the number of crystal defects increases and the growth becomes oriented to the {100} plane, which is the structure observed in monolayers.

Studies of the microstructure of $TiB_2$ showed different structures. Some grains without preferred orientation were almost spherical with a diameter of about 10nm. Grains with preferred orientation still have the same diameter but are collected into bundles and are columnar. It is not until a layer thickness of ~50nm that the spherical grains give way to the columnar structure. Then the hexagonal crystals grow preferentially in the <001> direction. It is the large number of defects in the first 50 nm that produces the equiaxed structure preventing the columnar growth [37]. Work done by Grovenor *et. al.*, [48] and Hentzell *et. al.*, [49] concluded that a change in texture could have an effect on properties similar to that caused by the interfaces.

Larsson *et. al.*, [40] studied a superlattice coating of TiN/NbN 10nm/5nm. They showed evidence of columns growing throughout the layers. However this phenomenon was not seen close to the interface.

### 2.3.4 Mixing and Interdiffusion

Setomya *et. al.*, [31] showed that interfaces between AlN/TiN were incomplete and 'wavy' due to slight interdiffusion or mixing. Analysis did not show any evidence of other phases and with a period of 3nm it is unlikely that a uniform layer could be formed.

Holleck *et. al.*, [36] found when sputtering TiC onto TiN or vice-versa a mixed phase of Ti(C, N) is formed with a width of approximately 3-4 nm. When sputtering TiN or TiC onto $TiB_2$, phases of Ti(B, C) and Ti (B, N) were formed respectively and the subsequent growth of the TiC or TiN was epitaxial. The width of the phase boundary was smaller in these cases i.e. only ~1nm.

Cawley *et. al.*, [47] did not find abrupt changes in composition across the individual layers in a ZrN/TiAlN film. However this was over a period of 2.6nm and hence the suggestion of intermixing, although probable, is unqualified as it would be almost impossible to ensure a totally parallel

interface to the beam and to be in a position to discount beam broadening with such thin individual layers. Also with such thin layers it is possible that they may not have formed fully, as Setomya *et. al.*, [31] found with a 3nm period coating.

§

## 2.4 Electron Energy-Loss Spectroscopy (EELS)

EELS has been such an integral part of this project, that it was deemed necessary to devote a section on how other research groups have used this tool, especially with respect to using it to identify a specific phase.

### 2.4.1 Introduction

When an incident electron passes through a sufficiently thin sample, interactions can occur resulting in a loss of energy. The size of such an 'energy-loss' is characteristic of the sample. EELS is a technique with a high spatial resolution and when utilised on the HB601 STEM with its probe of 1nm, can be a very powerful tool. A disadvantage of EELS however, is that only a specific energy-loss can be detected in any one spectra. This is overcome by using Parallel Electron Energy-Loss Spectroscopy (PEELS), where a range of energy-loss can be detected

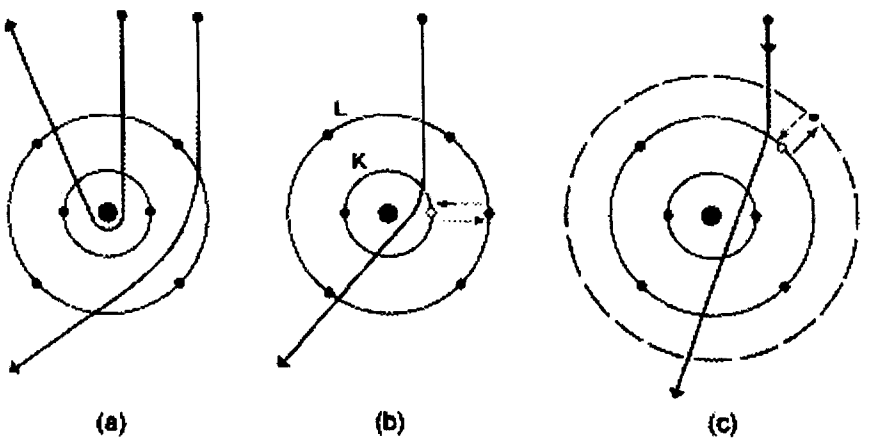


*Figure 2.20: Example of electron scattering by (a) Elastic scattering caused by Coulomb attraction by the nucleus (b)Inelastic scattering by inner-shell electrons and (c) by outer-shell electrons [50].*

simultaneously.

When incident electrons interact with an atom they do so via electrostatic (Coulomb) forces [50]. Some of these electrons are scattered as shown above in Figure 2.20. For *elastic scattering*, the incident electron passes close to the large electric field of the nucleus resulting in large angle deflections, termed as Rutherford scattering. If such an angle exceeds $90^0$ then the electron is backscattered. However incident electrons that travel close to the nucleus are in the minority, most interact further afield. *Inelastic scattering* results from incident electrons interacting with atomic electrons, as shown in Figure 2.20 (b) and (c). It is such interactions that lead to the formation of EELS spectra.

### 2.4.2 The Spectrum

The main features in an energy-loss spectrum are described below [50, 51]:

*Zero-Loss*: Contains all of the elastically scattered electrons and phonon scattered components.

*Low Loss*: between 0-50 eV, results from the excitation of electrons in delocalised orbitals extending over several atomic sites. This region is dominated by excitations of valence electrons known as plasmons.

*Core-Loss*: From 50eV-~2000eV forms as a result of the excitation of core electrons to unoccupied states above the Fermi level. Therefore features in this region contain information about the atomic character of the specimen.

*White Lines:* White lines occur in $L_{2,3}$ edges of transition metals and $M_{4,5}$ edges of rare earths. $L_{2,3}$ edges relate to transitions between 2p and unoccupied 3d states. For metallic copper the d band is totally full and hence no white lines are present. However in the case of CuO some d-levels are available as electrons are transferred to oxygen, hence white lines can occur. This is shown in Figure 2.21 below.

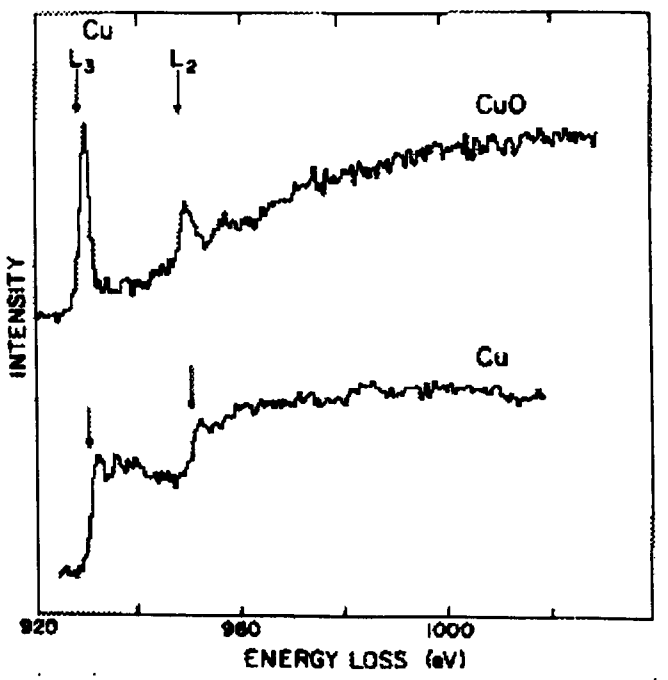


*Figure 2.21: Comparison of Cu-L in pure copper and CuO [50].*

The relative magnitude of the binding energy of L2 tends to be higher than L3 due to spin orbit splitting and hence practically, the L3 edge is usually the most intense of the two peaks. Theoretically it is double L2, but this is often not reflected in the experimental data [50].

### 2.4.3 Fine Structure

EELS atlases that show standard shapes of edges, have been developed for many elements in different compounds. These are continually being extended with the additional research into fine structure, and they enable us to probe materials and extract much more information than ever before. Figure 2.22 shows an example of how the spectra can be used as 'fingerprints' for a specific compound [52].

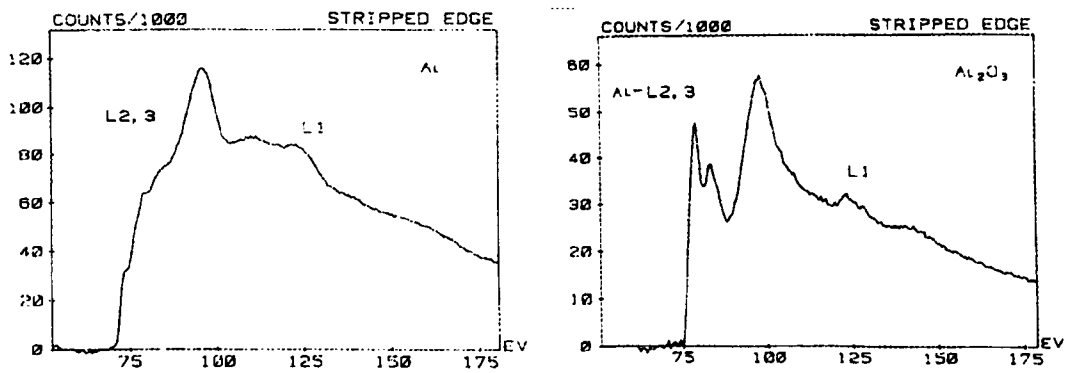


*Figure 2.22: Al L-Edge in (a) Pure Al (b) Alumina.*

### 2.4.4 ELNES

Electron energy-loss near edge structure (ELNES) occurs within 50 eV of the core edge. It is of particular interest due to the information it holds about nearest neighbours and bonding states. The structure arises as a result of electron transitions from the atomic core of the atom to unoccupied states above the Fermi-level. The fine edge structure (created at a precise energy loss) for such a transition is so specific that it can be used as a 'fingerprint' for that element in the particular compound in which it resides. This is due to ELNES being heavily dependent on not only what the surrounding atoms are, but also their co-ordination and bonding [51].

Fingerprints are usually seen more readily in complex molecules since they are more likely to have a low symmetry and a medium to long-range order. With molecules containing elements such as oxygen that cause backscattering, the ELNES is predominately made up from scattering events. The ELNES in this case is explained by molecular transitions [53].

### 2.4.5 Variation in Edge Structure

The basis behind the fingerprint is that if the same excited atom is surrounded by the same nearest neighbours, of the same co-ordination in two differing materials, it should produce the same fine structure [54]. However, this was not seen by McComb *et. al.*, [55], who found that the Si $L_{2,3}$ edge differs in zircon with respect to α-quartz even though it is the $[SiO_4]^{4-}$ tetrahedron in both cases that leads to the shape. This was put down to the large angular variance of $[SiO_4]^{4-}$ in zircon and the relatively small variance in α-quartz.

Sauer *et. al.*, [53] used ELNES to identify differing boron-oxygen compounds in a boron doped iron oxide film. In this work they found that the relative intensities of the σ* peak varied with the position of analysis. From this it was concluded that there were at least two different boron-oxygen phases present, one that contains only $BO_3$ groups and one that contains only $BO_4$ groups. Also reported was the effectiveness in using the π* peak to distinguish trigonal $BO_3$ from tetrahedral $BO_4$.

After identifying the fingerprints for these differing forms, attempts were made to quantify the amounts of these in a compound containing both.

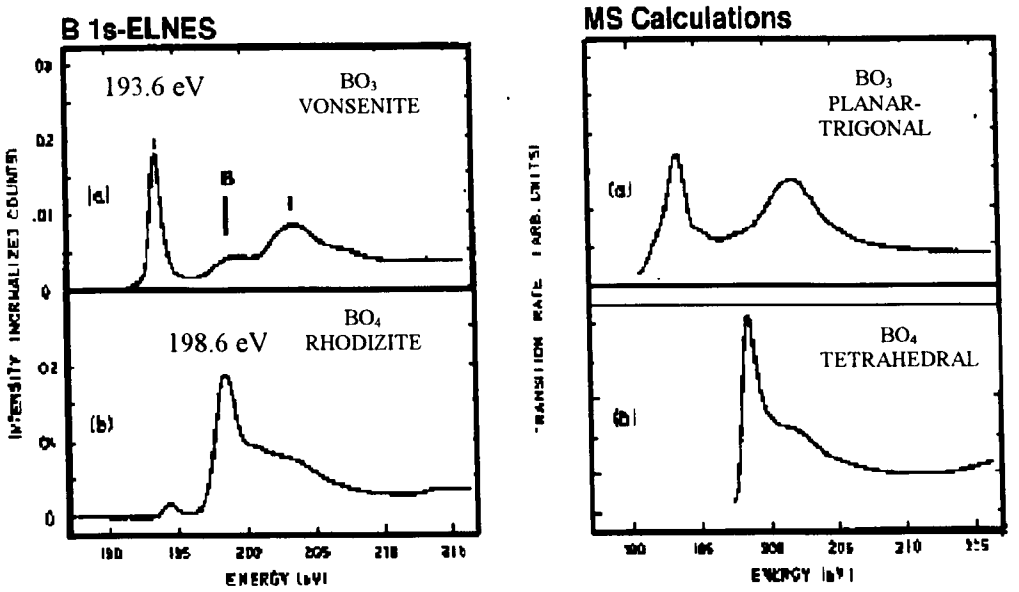


*Figure2.23: (a) Variations in the boron K-edge in $BO_3$ and $BO_4$ (b) Multiple scattering calculations for the same compounds.[53]*

Figure 2.23(a) shows the spectra obtained for $BO_3$ and $BO_4$. The differences found in the spectra are remarkable. The $BO_4$ with tetragonal symmetry, has an intense peak at 198.6 eV which relates to transitions to the $\sigma^*$ antibonding state from $B_{2p}$ states. The shoulder at slightly higher energy relates similar transitions from mainly $B_{2s}$ states.

They decided to confirm that these spectra can be used as 'fingerprints' for the presence of such clusters. This was done using ICXANES computer method [56]. Figure 2.23(b) shows the results of such calculations and in comparison to Figure 2.23(a) shows a good likeness. It was also found that since an increase of cluster size within the calculation did not have a

significant effect on the spectra, the ELNES is mostly dependent on scattering from its local neighbours.

A range of non-mineral B-K-edges have been studied by Garvie *et. al.*, [54] which are seen in Figure 2.24.

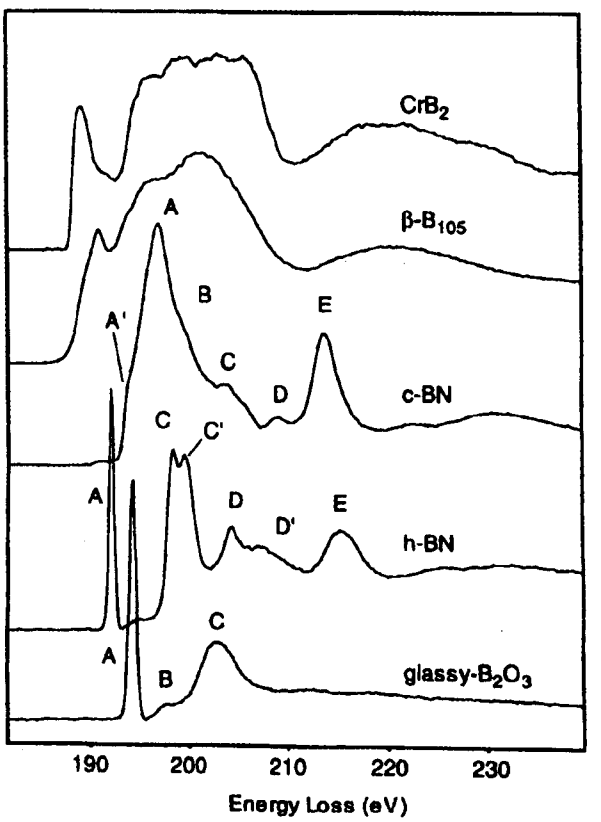


*Figure 2.24: A range of B K-edges from various materials [54]*

$\beta$-$B_{105}$ is a rhombohedral form of elemental boron with a unit cell of 105 atoms. $CrB_2$ has a likeness in shape to $\beta$-$B_{105}$ but the first peak in $CrB_2$ is at a slightly lower energy i.e. 188.6eV and is sharper. This lower energy is

thought to be due to the charge transfer from the Cr to the B. The $\pi^*$ peak at 188.6 eV is due to the presence of $sp^2$ bonding. The next feature at 200eV is due to $\sigma^*$ orbitals. In this structure the boron *'is present in layers of three-fold symmetry with each of the B atoms being $sp^2$ bonded to three other boron atoms. These boron planes are sandwiched between Cr layers'.*

### 2.4.6 Beam Damage

The work carried out by Sauer *et. al.*, [53] on B/O compounds also highlighted the problem of looking at boron-containing compounds under an electron beam, especially minerals.

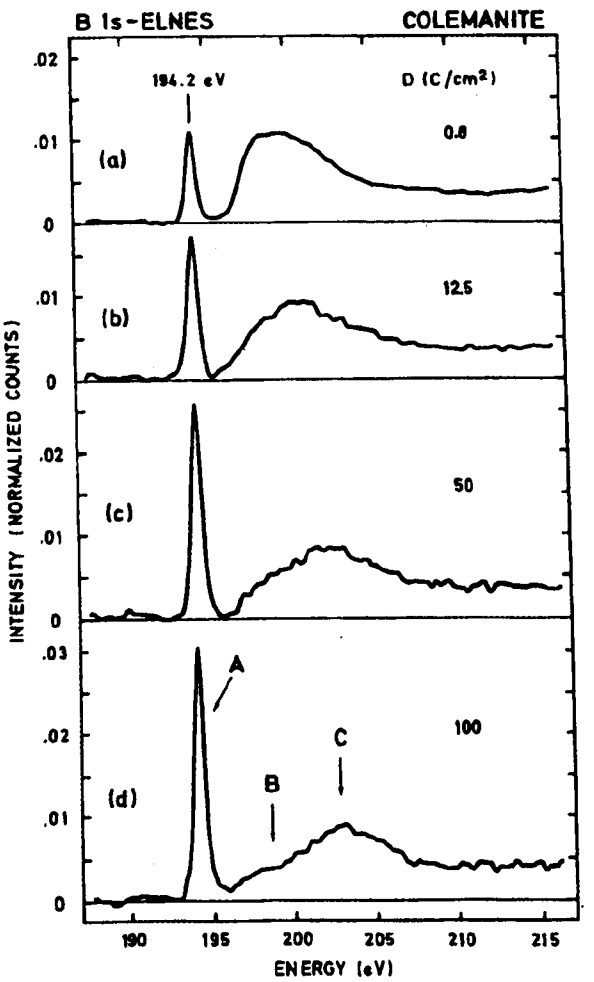


*Figure 2.25: Effect on B K-edge with electron dose [53]*

Figure 2.25 shows the extent of the effect on the boron 1s spectra with increasing electron dose on colemanite. On the principles explained above, $\pi^*$ transitions at 194.2 eV are considered to be as a consequence of the presence of $BO_3$ groups and the broad peak around 200 eV has contributions from both $BO_4$ and $BO_3$. If quantitative results are made from comparisons of these peak heights then beam damage must be considered. The larger the electron dose the higher the $\pi^*$ peak. The lowest radiation dose seemed to give expected results for the $BO_3$ : $BO_4$ ratio but similar experiments on howlite did not. The discrepancy

was put down to beam damage. However, it is thought to be due to the OH groups in these compounds which are removed under a beam especially when the high current density in the STEM probe causes heating. It was thought that $BO_4$ groups are the most likely to be affected and transform to $BO_3$ groups, hence the intensity of the $\pi^*$ peak increases and $\sigma^*$ peak decreases. After a critical dose an end product is reached, as it is then considered to only consist of $BO_3$ polyhedra.

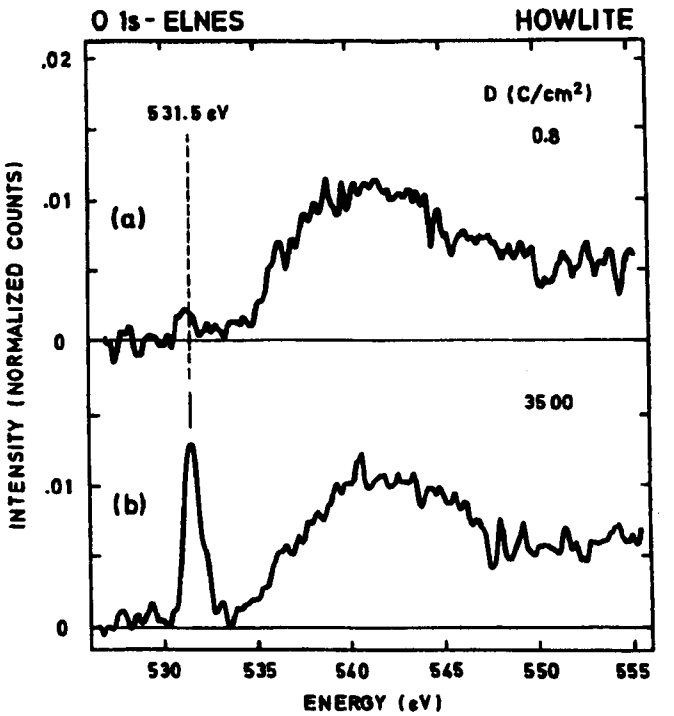


*Figure 2.26: O K-edge effect from electron dose [53]*

Figure 2.26 shows the corresponding oxygen spectra for the lowest and 'end product' dose of howlite. The main difference between the two is that in the high dose spectra a distinctive sharp peak is seen at 531.5 eV, (which is analogous to the O peak in amorphous $B_2O_3$) and in the low dose spectrum it is not present. It was assumed that this sharp peak occurs as a consequence of the transitions to the $\pi^*$ peak in the B K- edge and hence a $p\pi^*$ state is formed between the oxygen and the boron. This theory was backed up by the fact that the relative intensity of this sharp peak was proportional to the fraction of $BO_3$ groups present.

Garvie *et. al.,* [54] also stated that care must be taken whilst recording spectra of boron-containing minerals as they are easily damaged by the electron beam. For anhydrous materials such as sinhalite and rhodizite however damage is minimal even after long exposure under the beam.

### 2.4.7 Orientation Effects

The hexagonal form of BN is a layered material with boron atoms bonded to three N atoms within the plane. Such a structure shows a clear EELS spectrum dependence on the orientation of the sample with respect to the electron beam.

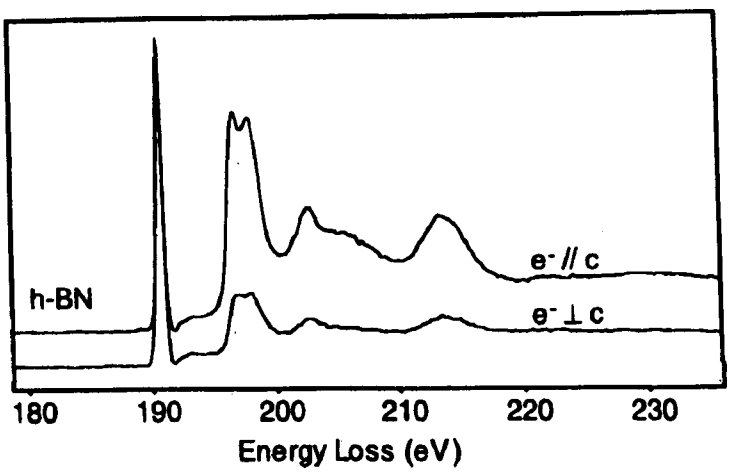


*Figure 2.27: B K-Edges from BN with the electron beam parallel and perpendicular to the a-axis, normalised to the π* peak [54]*

Such orientation dependencies of core-loss edges are thought to arise because of the directionality of the transitions to the unoccupied states [54].

### 2.4.8 Multiple Scattering (MS) Calculations

MS is *'based on the interference between the outgoing electron wave of the ejected electron and the wave which has been backscattered from the surrounding atoms'*.

Calculations were first set out for work on X-ray absorption near edge structure (XANES). The scattering properties of atoms can be calculated using muffin-tin approximations.

One major problem with the muffin tin description is that it cannot adequately describe covalent systems that possess directional bonding [51].

### 2.4.9 Molecular Orbital (MO) Calculations

This method considers interactions between atoms in terms of bands of orbitals. The degree of this interaction sets the energy width of such bands which in most cases can be directly related to the molecular orbital structure. It is possible using such a method to relate specific orbitals to features in the NES. A usual method is Linear Combination of Atomic Orbitals (LCAO) which expresses various molecular orbitals as linear combinations of a finite set of atomic orbitals, known as the basis set. Some variations of this method realise the limitations of a using limited basis set and, as with MS theory, tend to instead take a muffin tin approach instead [47].

Tain *et. al.*, [57] calculated the partial density of states (DOS) for $TiB_2$ using Linear Muffin-Tin Orbitals (LMTO) with atomic sphere approximation

(ASA). The first observation was the significant overlap of two different states Ti-3d and B-2p. It was concluded that there must be strong hybridisation between the B-2p and Ti-3d states indicating strong interlayer bonding in $TiB_2$. This gives some explanation as to why $TiB_2$ has a much higher melting point and hardness with respect to hcp Ti. This evidence of hybridisation also suggests that the role of charge transfer is not so significant in $TiB_2$. Infact it is calculated at just 0.25 electrons from Ti to B.

§

## 2.5 Structure and Properties of the Coating Materials

### 2.5.1 Titanium Diboride

Transition-metal borides of the $AlB_2$-type structure have some outstanding properties [57] and $TiB_2$ is no exception. It boasts a hardness of ~3000Hv and a melting point of 3225°C [58], has good conductivity and excellent resistance to chemical attack [59]. These unique properties explain how it has found a wide range of applications, which include; armour protection, wear-resistant coatings, cutting tools, a cathode material in molten salt electrolysis and a grain refiner [59, 60].

Wang [61] also highlighted the potential for $TiB_2$ as a reinforcement material in a high temperature composite and cited the addition of 30% $TiB_2$ into NiAl which produces a threefold increase in yield stress at 1273K; the reason for this improvement is unknown.

The effectiveness of $TiB_2$ in such applications is heavily dependent on the microstructure. However it is both difficult and expensive to obtain a fully dense structure as it usually carries a high degree of porosity. This has led to problems with brittleness [59].

### 2.5.1.1 The Structure of $TiB_2$

Parthe [62] defined the structure in 1967 as a topologically hexagonal structure in which the boron atoms form a net connection only. The ideal packing, as set out by Laves [63] is c/a=1.07; $TiB_2$ is 1.063. Tain *et. al.*, [61] described the structure as a simple hexagonal lattice in which HCP Ti layers alternate with graphite-like B layers [57]. The lattice parameters and atomic radii are shown in Table 2.1

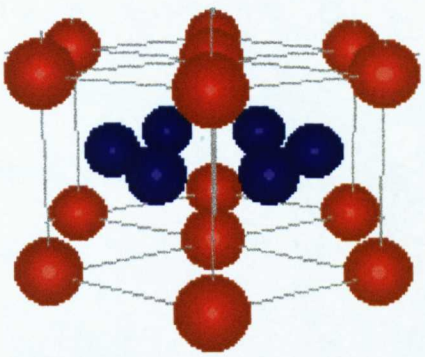

Figure 2.29: The structure of $TiB_2$ [57]

| a (Å) | c (Å) | Ti-Ti (Å) | Ti-B (Å) | B-B (Å) |
|---|---|---|---|---|
| 3.028 | 3.228 | 3.028 | 2.35 | 1.75 |

Table 2.1: *Parameters of $TiB_2$ [57].*

Little is understood about the bonding in $TiB_2$. Tain *et. al.*, [57] highlighted the importance of the interaction between the titanium and boron atoms and cited the higher melting point and hardness of $TiB_2$ with

respect to HCP titanium as evidence. A strong hybridisation of Ti 3d and B 2p states, even though from differing layers indicates strong interlayer bonding.

### 2.5.1.2 Metallic or Ceramic?

There is controversy about whether $TiB_2$ is metallic or ceramic. Many describe it a ceramic [59, 64] but others believe it to be metallic [57, 58].

Wang *et. al.*, in 1991 [61] considered $TiB_2$ to be a ceramic and reported its improved high temperature strength compared to other ceramics such as SiC and $Al_2O_3$. In contrast Tian *et. al.*, [57] presented strong evidence for the metallic behaviour of $TiB_2$.

### 2.5.1.3. $TiB_2$ Films

$TiB_2$ films have been made with a variety of techniques; magnetron sputtering [58], CVD [65], electron beam evaporation from a sintered target [66] and dynamic ion mixing [64].

Lohmann *et. al.*, [58] found during Auger depth profiling of a $TiB_2$ film that the titanium/boron ratio is greater than the stoichiometric value. This was explained by additional boron being incorporated within the coating, possibly at grain boundaries or as interstitial impurities. This

difference was much more significant with higher bias voltages. In contrast Riviere [64] presented work of Auger depth profile analysis on their ion beam assisted deposition had a B:Ti ratio less than the stoichiometric ratio. In this case the structure is considered as not being completely crystalline and it is suggested that there is a high concentration of amorphous titanium which surround the $TiB_2$ crystals. They state that without ion mixing the $TiB_2$ film is almost completely amorphous. Bombardment was crucial in producing a crystalline phase. Riviere [64] also reported the the texture as {001} and a grain size of 3nm.

Lohmann *et. al.*, [58] reported a texture which was highlighted in XRD studies. At lower biases the (001) peak predominates, however at -40V and -50V bias the (101) peak dominates. It was concluded that the crystal grows in preferred directions depending on bias voltage.

Another texture effect became apparent by studying the intensity of the peaks in the XRD spectra. These proved to be sensitive to the angle of collection. This was thought to be due to the geometry of the sample during sputtering. Some columns were non-perpendicular and are also thought to contribute to this effect. At low bias this effect is not as noticeable. Holleck [36] also found that $TiB_2$ grows in the {001} plane when sputtered. A coherency was found in their $TiB_2$/TiC multilayer

with the close packed planes. When sputtering $TiB_2$ onto TiC or TiN an intermixed boundary is formed.

**2.5.1.4 Properties**

Wert *et. al.*, [68] carried out Vickers and Knoop microhardness tests on the coatings. They acknowledged the problems with measuring hardness on very thin brittle coatings. The problem of sampling the substrate and fracturing the coating was overcome by using very small precise loads. The hardness was found to be as a rule independent of the number of layers, i.e. 20 layers not much different to 1000 layers (same overall coating thickness). Crack resistance, however, shows a strong relationship with the number of layers [36].

In contradiction to this work Hilz and Holleck [37] considered that the properties were heavily influenced by the number of phase boundaries. They had the same overall thickness but differing individual layer thicknesses. They sputtered a single layer of $TiB_2$ which showed a strong {001} texture and also reported a shift in the peaks due to a decrease in the spacing of lattice planes parallel to the substrate of 0.5%. It also highlights the random nature of the 50nm first part of the $TiB_2$ layer where there are spherical 10nm grains. Above this the grains are about 10nm in diameter and 50nm long. The direction of fastest growth in $TiB_2$ is that with the

<001> *direction* perpendicular to the substrate. The paper cites the large number of defects as a reason for the small grain size. It was reported that the texture of $TiB_2$ is distributed in the TiC/$TiB_2$ multilayer. They show, in contrast to previous Auger work, no evidence for an interface zone between TiC and $TiB_2$.

### 2.5.2 Copper and Aluminium

Much more is known about copper and aluminium than titanium diboride. They are both f. c. c. and have relatively low melting points and hardness values. They also differ from $TiB_2$ in relationship to cost and availability and it is for many of these reasons that the pair were chosen for the BNFL coatings. The orientation of growing films obviously depends on the processing conditions and substrate but many have found that Cu and Al can exhibit an orientation with their {111} planes parallel to the substrate [18, 69, 70].

#### 2.5.2.1 Copper/Aluminium Phases

The phase diagram for the binary system is shown in Figure 2.29 and although much has been reported for the Al-rich end in terms of age/precipitation hardening, much less is known about the phases in the copper rich end.

One copper/aluminium phase which has been well reported is $CuAl_2$ ($\theta$) and its formation of it via Guiner-Preston (GP) zones. It has a tetragonal structure with

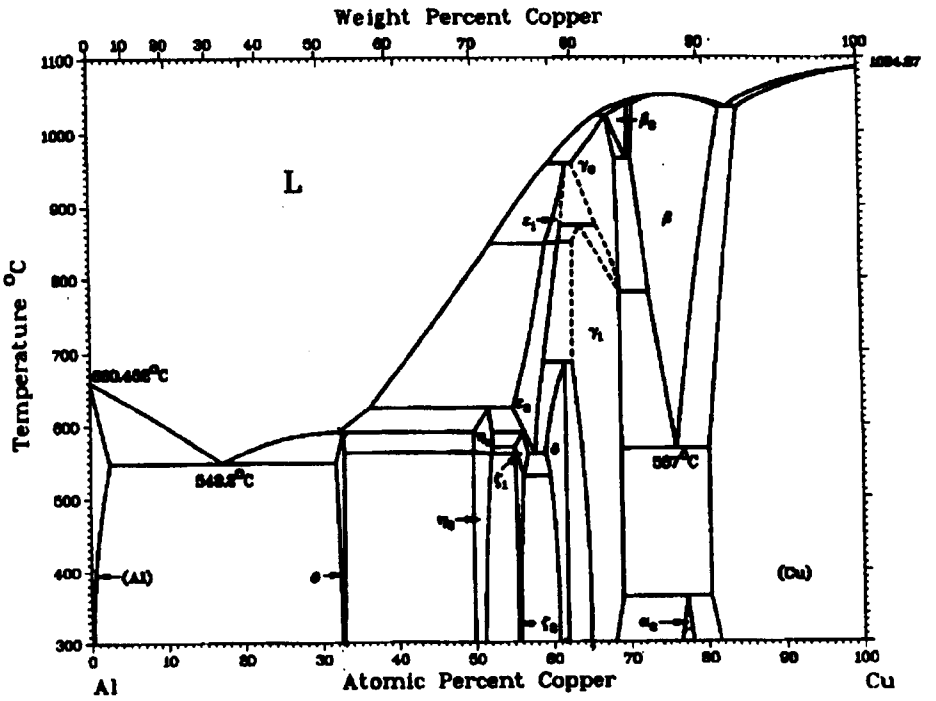


*Figure 2.29: Cu/Al phase diagram [71]*

a=6.066Å and c=4.874Å [72], and as fine precipitates in an aluminium matrix can result in a much harder structure, thought to be due to the obstruction of dislocation slip. However, a phase of pure $CuAl_2$ produces hardness values less than half that achieved with fine dispersions in an Al matrix[73].

Figure 2.30 shows the reported phases for Cu/Al alloys; from this it is clear that there is still much left to identify concerning some of these phases

**Al-Cu Crystal Structure Data**

| Phase | Composition, at.% Cu | Pearson symbol | Space group | Strukturbericht designation | Prototype |
|---|---|---|---|---|---|
| (Al) | 0 to 2.48 | *cF4* | $Fm\bar{3}m$ | *A1* | Cu |
| $\theta$, $\theta'$ | 31.9 to 33.0 | *tI12* | *I4/mcm* | *C16* | $Al_2Cu$ |
| $\eta_1$ | 49.8 to 52.4 | *oP16* or *oC16* | *Pban* or *Cmmm* | ... | ... |
| $\eta_2$ | 49.8 to 52.8 | *mC20* | *C2/m* | ... | ... |
| $\zeta_1$ | 55.2 to 59.8 | *hP42* | *P6/mmm* | ... | ... |
| $\zeta_2$ | 55.2 to 56.8 | (a) | ... | ... | ... |
| $\varepsilon_1$ | 59.4 to 62.1 | (b) | ... | ... | ... |
| $\varepsilon_2$ | 55.0 to 61.1 | *hP4* | $P\bar{6}3/mmc$ | *D8₁* | NiAs |
| $\delta$ | 59.8 to 61.9 | (c) | $R\bar{3}m$ | ... | ... |
| $\gamma_0$ | 59.8 to 69 | (d) | ... | ... | ... |
| $\gamma_1$ | 62.5 to 69 | *cP52* | $P\bar{4}3m$ | *D8₃* | $Al_4Cu_9$ |
| $\beta_0$ | 67.6 to 70.2 | (d) | ... | ... | ... |
| $\beta$ | 70.6 to 82.0 | *cI2* | $Im\bar{3}m$ | *A2* | W |
| $\alpha_2$ | 76.5 to 78 | (e) | ... | ... | ... |
| (Cu) | 80.3 to 100 | *cF4* | $Fm\bar{3}m$ | *A1* | Cu |
| **Metastable phases** | | | | | |
| $\theta'$ | ... | *tP6* | ... | ... | Distorted $CaF_2$ |
| $\beta'$ | ... | *cF16* | $Fm\bar{3}m$ | *D0₃* | $BiF_3$ |
| $Al_3Cu_2$ | 40 to 50 | *hP5* | $P\bar{3}m1$ | *D5₁₃* | $Al_3Ni_2$ |

(a) Monoclinic? (b) Cubic? (c) Rhombohedral. (d) Unknown. (e) *D0₂₂*-type long-period superlattice.

*Table 2.2: Cu/Al phases [71].*

### 2.5.2.2 Interactions

Research has been carried out on interfaces between copper and aluminium/alumina. In 1992, Hackney [74] reported theta phase growth during interdiffusion studies between copper/aluminium interfaces. Single crystal aluminium was coated on one side with nano-crystalline copper; when such a sample was heated above 340°C theta phase began to grow into the aluminium layer. It was thought that supersaturation of the

Al phase must exist for θ to nucleate and grow in the Al. Resistance to interdiffusion within the copper/aluminium couples was achieved by sputtering a carbon layer between them.

$Cu/Al_2O_3$ interfaces have been studied much more [75] and have involved the use of ELNES [69]. Dehm *et. al.* [69], used EELS to try and characterise the interface. They found the Cu L-edge had an unidentified shape, which indicated free 3-d states resulting in a white line at 933 eV. Also significantly, the O K-edge exhibited a shoulder as seen in Figure 2.31 below. This could only be explained by the presence of Cu-O bonds in this region.

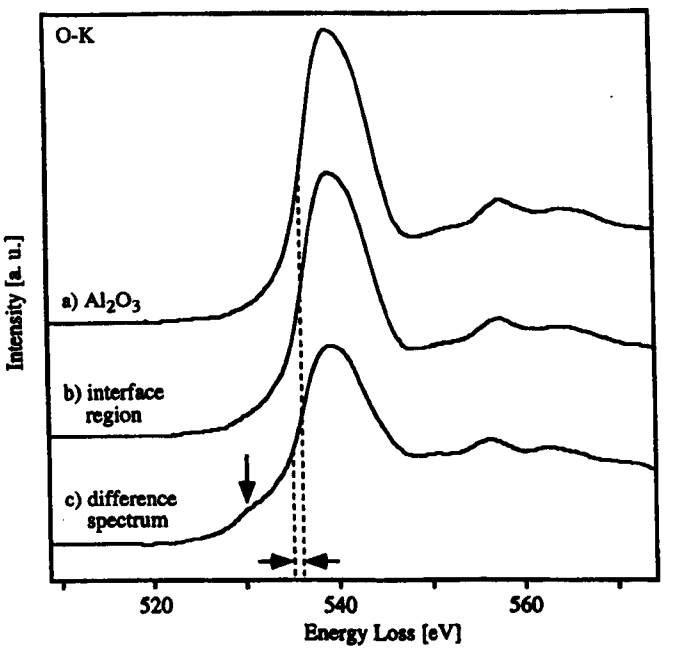


*Figure 2.30: ELNES O-K spectra from $Cu/Al_2O_3$ sample [69]*

Rogers *et. al.*, [75] reported the formation of $Cu_2O$ needles at the interface and even though thermodynamically possible, $CuAlO_2$ did not form until annealed at 1000°C under the correct partial pressure of oxygen. This was quoted at $7.2x10^{-8}$ Pa. They also highlighted the instability of $CuAlO_2$ if the partial pressure falls below $7.2x10^{-3}$ Pa, as Cu and $Al_2O_3$ are in equilibrium.

Jacob *et. al.*, [76] also identified the presence of $CuAlO_2$ after the reaction of Cu with $Al_2O_3$. They cite that the crystal structure of $CuAlO_2$ is rhombohedral with a=3.489Å and c=16.98Å.

Even though Cu and Al are well known materials it is clear that some of their alloys and phases are not so straightforward and could prove difficult to identify.

§

# Chapter 3

## *Experimental Techniques*

Chapter 3 explains experimental techniques used to achieve the aims of the project.

Novel sample preparation techniques are included along with descriptions of the three types of electron microscope used to analyse them: Auger, TEM and STEM. Other techniques used include XRD and microhardness.

§

## 3.1 Preparation of Samples for Analysis

Most samples used for this project were cross-sectional TEM samples and hence sample preparation takes up most of this section. However brief mention of the sample preparation used for Auger, XRD and hardness data are also included.

### 3.1.1 Cross-Sectional TEM Sample Preparation

For both sets of multilayer coatings, very little sample (<1cm$^2$) was available for analysis. This made it imperative to minimise mistakes during preparation and therefore extra steps had to be taken to ensure this.

The first step was to section the coating in half and glue the two faces together. This was done to double the quantity of coating that could be ion milled. Any cutting was carried out using a slow speed wire saw to minimise damage to the coating on its thin substrate.

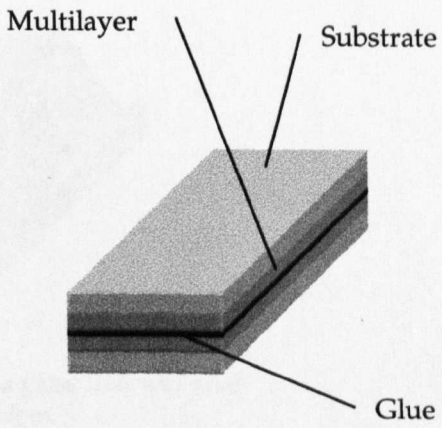


*Figure 3.1: Multilayer Sandwich*

It is very important to keep the substrates flat so that the glue layer was as thin as possible. Hence any cutting was carried out with the sample

encapsulated in thin glass slides to prevent burring. Also to avoid the glue from prematurely ion beam thinning away, silicon carbide was mixed into araldite to create the glue layer. This sandwich was cured at no more than $70^0$C for 20mins and left to dry fully for 24 hours.

When making cross-sectional samples, it is quite probable that when the sandwich is ground too thin the sandwich tears along the glue line. Due to the differential ion-milling rates of $TiB_2$ and Al, it was imperative to get the sandwich as thin as possible by mechanical methods. This increased the likelihood of such tearing. To prevent this, two glue layers were put at the sides of the sandwich to provide extra support. This is illustrated in Figure 3.2.

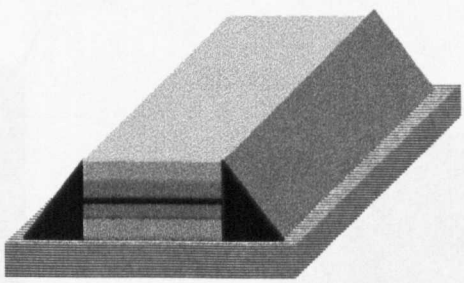

*Figure 3.2: The sandwich is stuck onto a glass slide and glue supports added to the edges.*

When the glue supports are dry another glass slide is attached with super-glue to the surface and thin strips are cut using the slow speed wire saw, as shown in Figure 3.3.

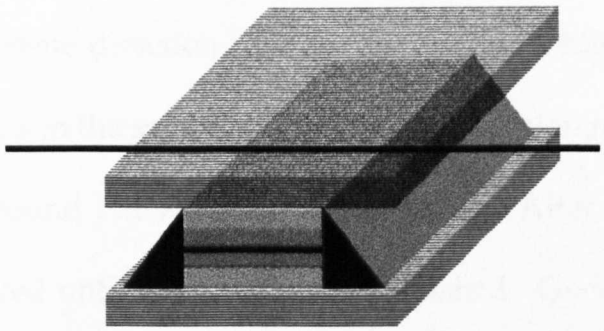

*Figure 3.3: Encapsulated in glass, thin strips are cut using a slow speed wire saw*

The resulting thin strip of the sandwich is now ready for grinding. It is first ground flat on one side and polished to ¼μm finish. The grinding was carried out using a concentric polishing jig, shown in Figure 3.4.

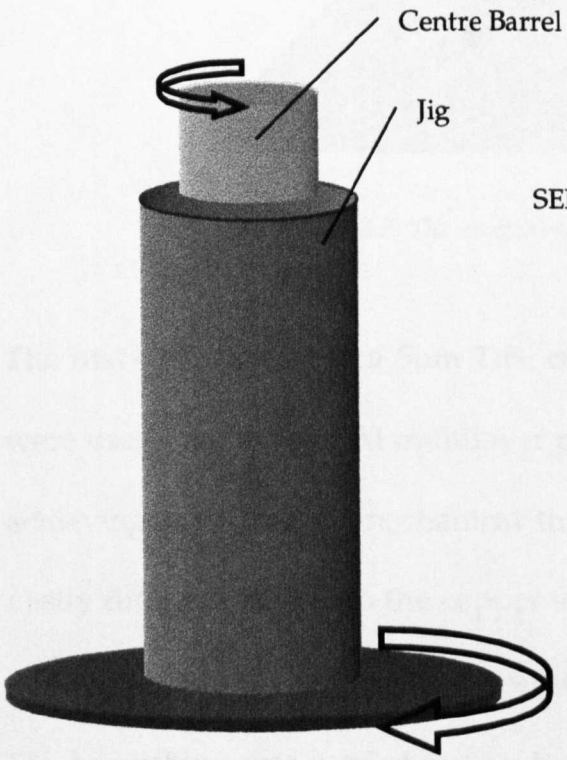


*Figure 3.4(a): Grinding Jig*

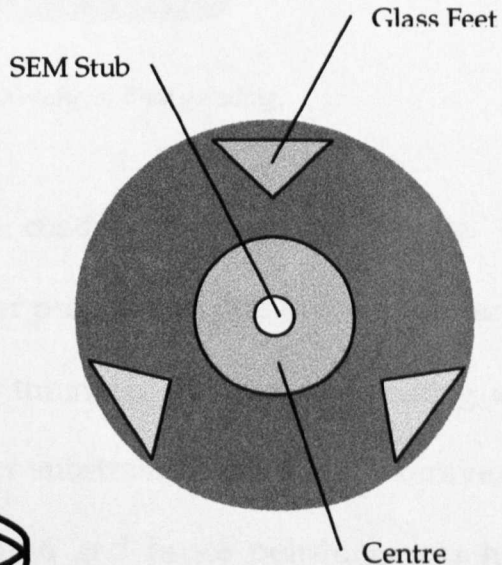


*Figure 3.4(b): Base of Grinding Jig*

Such a jig is widely used for making cross-sections. The jig is used for the main rotation action of grinding. Simultaneously, the centre barrel is turned in the opposite direction. These opposing movements prevent the formation of bevels in the sample. The SEM stub is interchangeable and to start with it is ground flat with respect to the jig. After this is done the stub is not removed until the grinding has finished. Once the first side is flat it is removed from the stub by soaking in acetone, and then fixed with super-glue to a fresh stub as shown below in Figure 3.5.

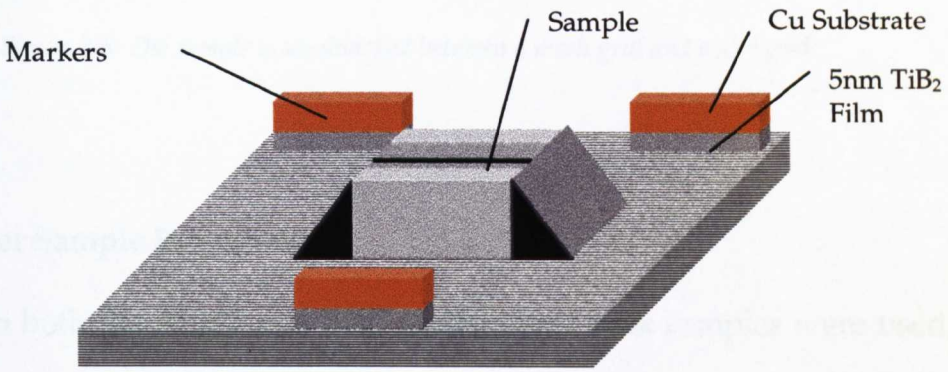


*Figure 3.5: The sample ready for final grinding.*

The markers used were a 5μm $TiB_2$ coating on a copper substrate. They were used for the $TiB_2$/Al multilayer preparation due to the importance of achieving very precise mechanical thinning. Because the coating was a vastly differing colour to the copper substrate, when the markers reached ~5μm the copper colour disappeared and hence polishing was halted. Final polishing was carried out by hand, using ¼μm diamond paste on a sheet of glass. Metadi fluid was used for lubrication.

After cleaning the sample, a mesh was stuck to it using araldite. The $TiB_2$/Al coatings and the Cu/Al had a copper and nickel mesh respectively. A slot was also attached for extra support, as the samples had to last, as shown below in Figure 3.6.

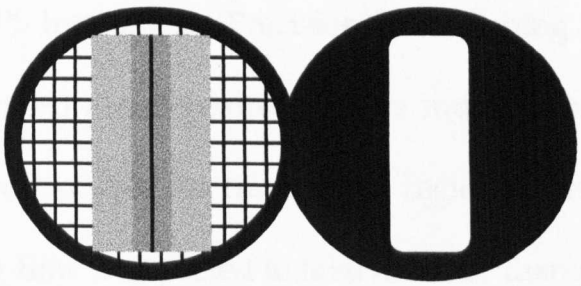

*Figure 3.6: The sample is sandwiched between a mesh grid and a slot grid.*

### 3.1.2 Other Sample Preparation

For use in both the Auger and XRD instruments bulk samples were used, in plan view. The area of sample used in both cases was approximately 1cm$^2$. For hardness tests the plan-view and cross-section samples were cold set in a mount for support.

### 3.1.3 Ion Beam Thinning

For the $TiB_2$/Al coatings the only ion beam thinner available for use was a Gatan Dual Ion Mill. Such a machine uses 4kV argon ions that impinge on the sample from both above and below (if required). This set up, used for

the $TiB_2$/Al required times of approximately 4-6 hours to achieve electron transparency.

After the acquisition of the Cu/Al coatings the department now had available a Gatan PIPS Instrument (Precision Ion Polishing System). This uses much more focused argon beams that are much more controllable, resulting in wider areas of electron transparent regions. Also due to such precision, the milling time is expected to take no more than 60 minutes for any sample. For the Cu/Al samples this time was ~15 minutes. Also the guns were turned off when the interfaces of the coatings were parallel to the incident beam. This was to avoid preferential milling along these regions.

## 3.2 Electron Microscopy Techniques

### 3.2.1 Auger

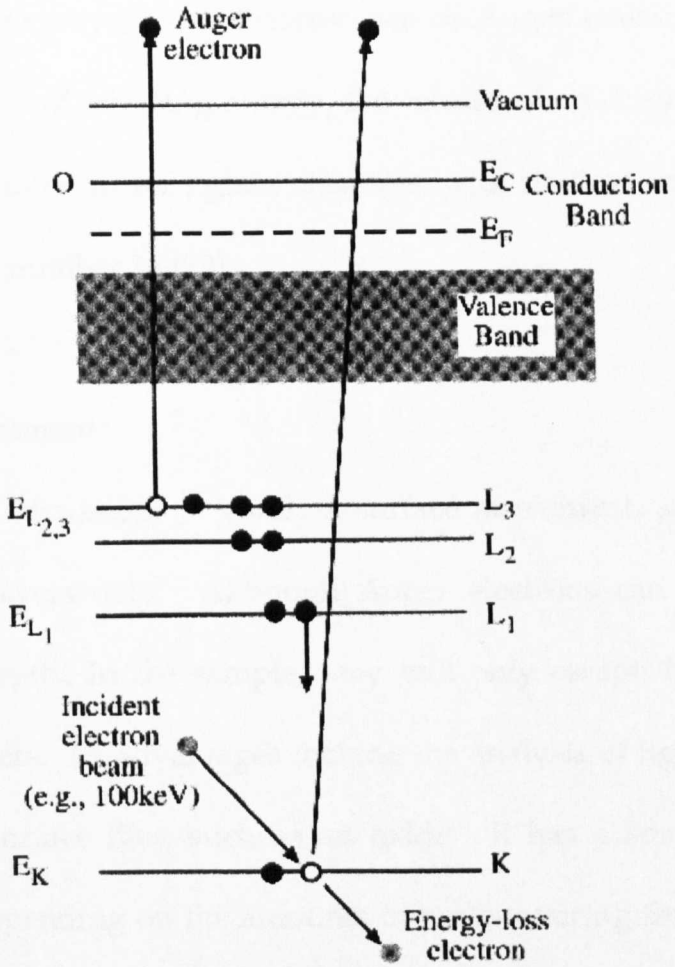


*Figure 3.7: A schematic showing the emission of an Auger electron.[89]*

Figure 3.7 shows events that can occur, resulting in production of an Auger electron. An incident electron of a specific energy $E_p$, displaces an electron in the K-shell of the atom. To do so, theoretically $E_p$ must be greater than $E_k$, the binding energy of an electron in the K-shell. However in practice it is usually necessary for $E_p$ to be at least $5E_k$ for efficient ionisation to occur [78].

The now unstable atom relaxes, by the void in the K-shell being filled by the transition of an electron from the $L_1$ shell. This results in an excess of kinetic energy within the atom of $E_K$-$E_{L1}$. Such an energy can be released in one of two ways, X-ray fluorescence or Auger emission. Of the two possible ways of releasing energy, the release of an Auger electron is the more likely to occur for lighter elements, with shallow core levels i.e. less than atomic number 34 [78].

### 3.2.1.1 Instrument

The Auger microscope is purely a surface instrument, analysing the first few monolayers only. Although Auger electrons can be generated at different depths in the sample, they will only escape from the top few surface layers. Its advantages include the analysis of light elements even in a thin surface film, such as an oxide. It has a spatial resolution of ~0.1μm, depending on the amounts of backscattering from the rest of the sample.

The main technique used for analysis on $TiB_2$/Al multilayer coatings was drilling of a crater using the ion gun and then analysing the surface. The gun uses 4kV argon ions, focused on the surface to remove material. Such a crater would be around 1mm in size, and reveal approximately 10 individual layers. The problem with analysing the layers is that there is

always the possibility of contamination from surrounding layers as a consequence of the sputtering.

### 3.2.2 Transmission Electron Microscopy (TEM)

One of the main tools used to achieve the aims of this project has been Transmission Electron Microscopy (TEM).

#### 3.2.2.1 Instrument

The microscope used was a JEOL 2000FX equipped with an ultra thin window QX2000 Link X-ray detector. This particular instrument has a tungsten filament, operating with a 200kV accelerating voltage. It also has a scanning attachment to enable linescans to be carried out.

All of the multilayer cross-sections have been studied and imaged using this machine. Apart from standard bright field imaging, dark field and selected area diffraction have been the other techniques used. The following sections briefly explain these methods.

### 3.2.2.2 Dark Field Imaging

Dark field techniques were primarily used to establish grain sizes and character in the Cu/Al samples, the principle is shown in Figure 3.8 The method used was by tilting the beam as shown in Figure 3.8(c):

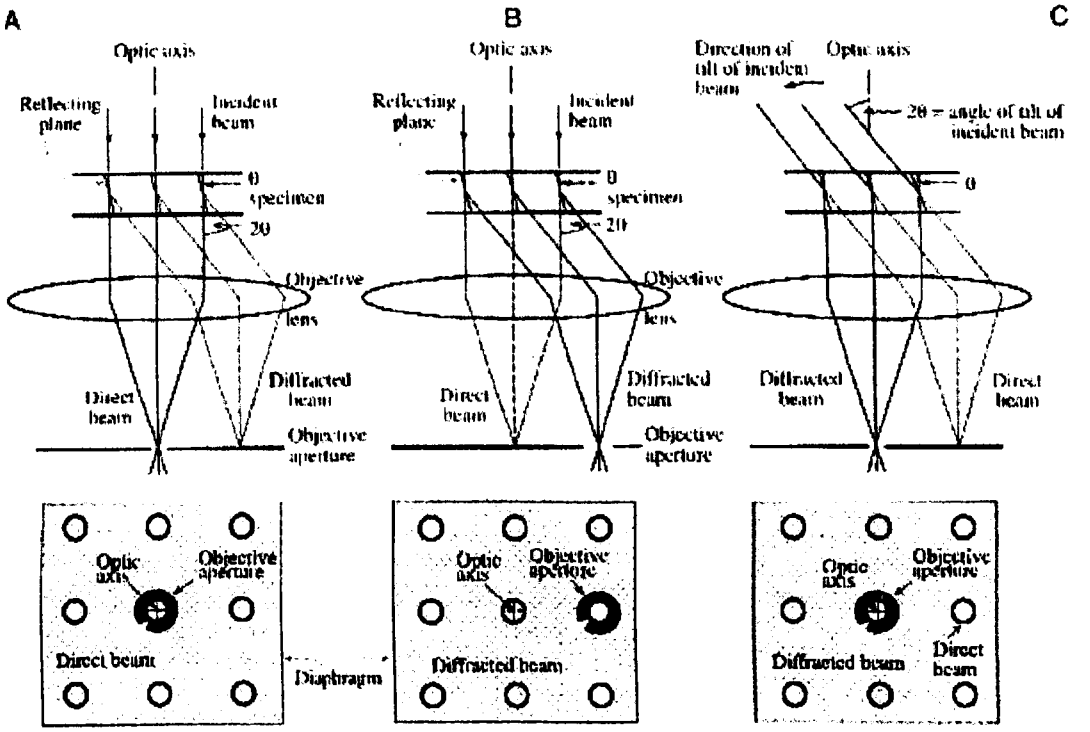


*Figure 3.8: A Schematic of the principle of dark-field imaging [77]*

The objective aperture used was the smallest available at 20μm, this was due to the complicated selected area diffraction pattern (taken from several layers) that was being used. The smallest aperture enabled as much signal as possible from other diffraction spots to be eliminated from the dark-field image. This technique would have been ideal to establish where unknown phases present reside. However such spots were so faint they were only detected after the photographic negative printing.

### 3.2.2.3 Diffraction

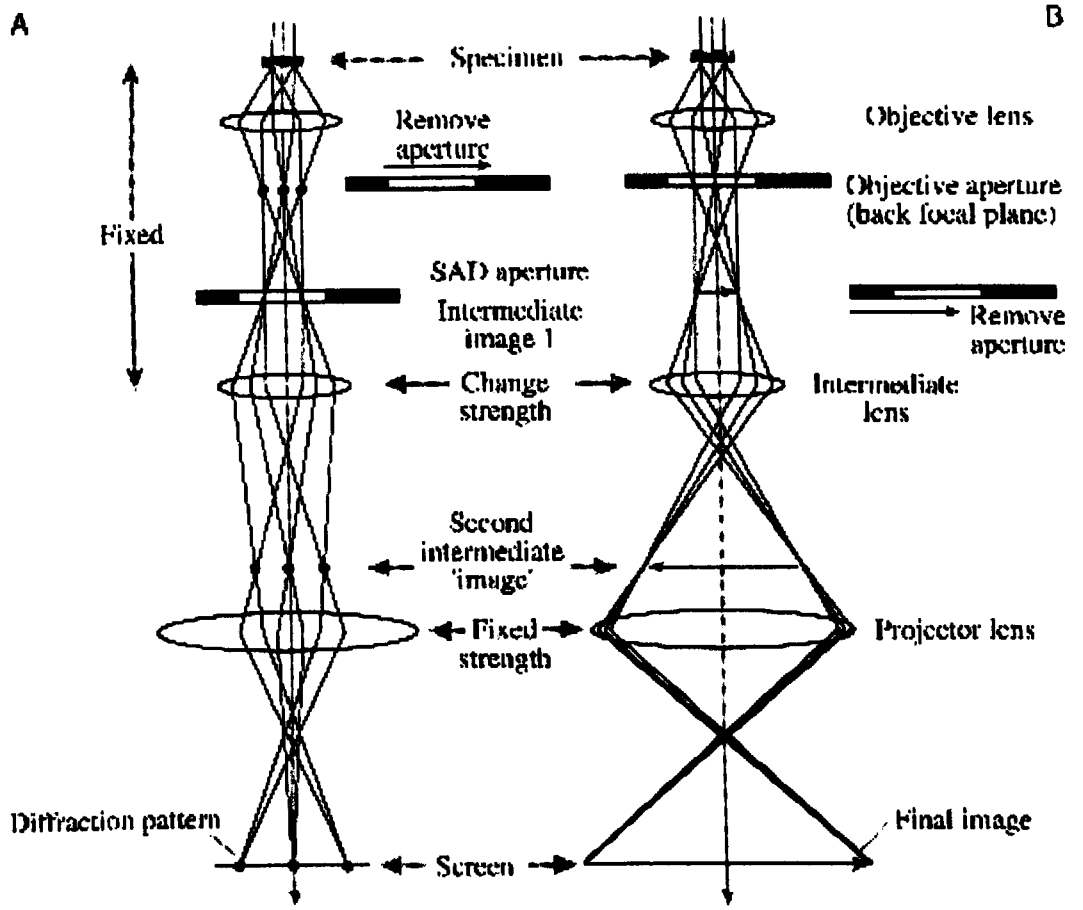


*Figure 3.9: Difference between diffraction and imaging in TEM [77]*

Selected area diffraction was carried out using the smallest possible aperture (20μm). Even with this small aperture several layers contributed to the diffraction pattern. The actual area of the sample that did contribute would be ~1μm², when taking the demagnification of the objective lens into account.

### 3.2.3 Scanning Transmission Electron Microscopy (STEM)

The majority of analysis carried out in this project was using a dedicated STEM, due largely to the restrictive size of the individual layers.

#### 3.2.3.1 Instrument

The STEM is a 100kV dedicated, cold field emission, VG HB601 UX microscope, equipped with a windowless X-ray detector and a parallel electron energy-loss spectrometer. It is primarily used for analytical studies on a nanometer scale.

#### 3.2.3.2 X-ray

Because of the near UHV conditions in the STEM, it can have a full windowless X-ray detector (Link Pentafact with an EXL$_{II}$ processing computer). This gives the advantage of analysing lighter elements and hence it can easily cope with oxygen and thankfully, boron. The apertures used for standard analysis were a 25μm virtual objective aperture (VOA), 500μm collector and a 50μm SAD. Spot analysis can be taken from very small regions as the analytical probe can be as small as 1nm. This probe can also be periodically stepped across an interface to produce a linescan. In most cases for the purpose of this project, the probe would scan 16, 32 or 64 periodic spots along a predetermined line. The time spent acquiring an EDX spectrum at each spot would be between 5 and 10 seconds

depending on the level of signal obtained and the amount of drift. There is no point in acquiring for extended times if the probe is no longer sampling the correct area. Background signals were also acquired simultaneously and removed from linescan data when appropriate.

### 3.2.3.3 PEELS

The STEM is equipped with a Gatan 666 spectrometer and for PEELS analysis the probe can be focused to 0.4nm. For the purpose of this project this was unnecessary and a probe of 1nm was used. Small apertures were used for fine structure investigations to create small convergence and collection angles. The 20μm real objective aperture has a half angle of 5.9mrads and this was paired with a 1000μm collector aperture at 6.8mrads. The number of electron volts per channel used, was 0.2eV and in most cases spectra were acquired for no longer than 10 seconds. The dark count and gain from the spectrometer were removed using the Gatan software, as was the background. Most samples were below $0.5\lambda$ ($\lambda$ = plasmon mean free path) in thickness but where necessary were deconvoluted by standard methods [50].

## 3.3 Other Techniques

### 3.3.1 XRD

There were two different XRD machines (Powder type) used to carry out this work. One based in Liverpool (McLean) and the other at BNFL Springfields (Phillips). The later was more up-to-date and fully computerised with the latest power diffraction database to hand. A Cu-target tube was used in both machines at 30kV, 25mA.

### 3.3.2 Hardness Measurements

There were two different hardness measurement methods used on the Cu/Al coatings, Vickers Microhardness and Knoop Hardness. Knoop hardness testing has a distinct advantage over Vickers hardness testing; the specialist diamond is ~30 times as long as it is deep, enabling thinner coatings to be measured. Where possible the Knoop tester at BNFL was used for the Cu/Al coatings. Unfortunately a Vickers diamond was the only one available for use on the $TiB_2$/Al coatings and did not meet the

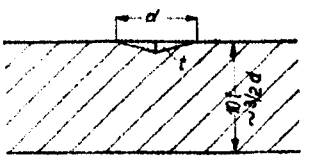


*Figure 3.10: Criteria for hardness data on thin films [79]*

criteria required to achieve adequate data on thin films as shown in Figure 3.10. The penetration of the diamond into the film should not be more than a tenth of the overall thickness of the film, if effects from the underlying substrate are to be discounted. However the diamond must sample a reasonable amount of the coating for good data to be obtained, Figure 3.11 shows such minimum penetration depths for various materials (D = Minimum permissible layer thickness or minimum diameter if a wire)

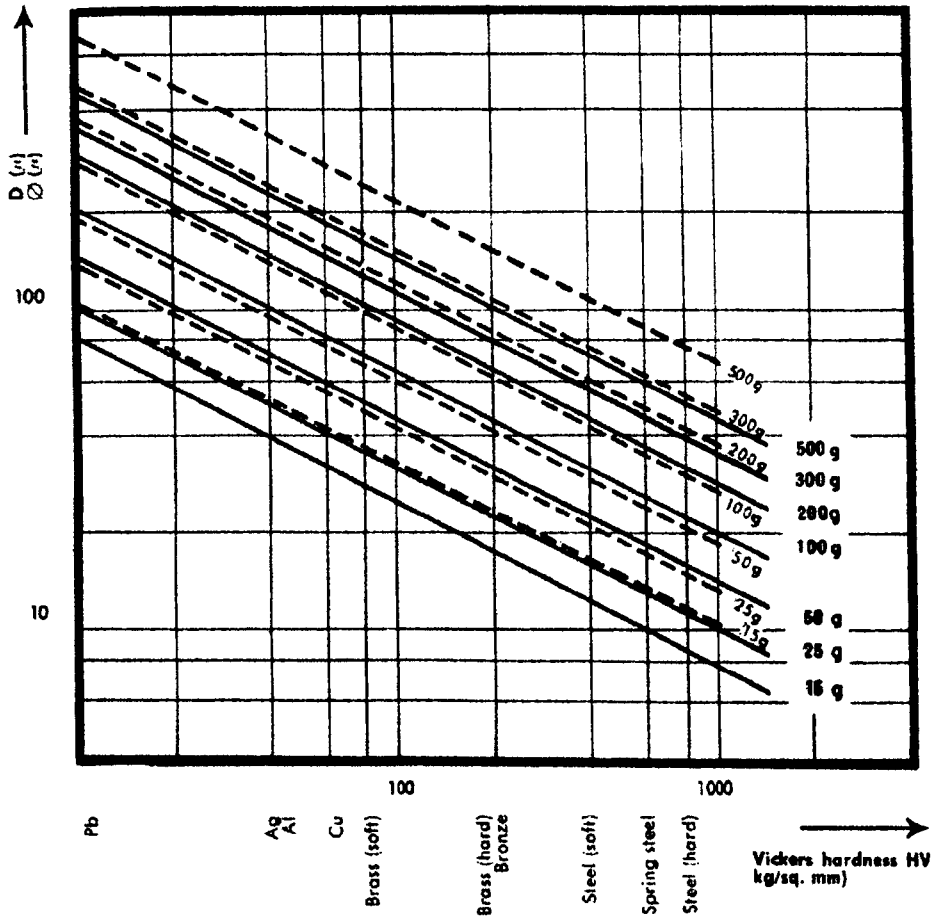


*Figure 3.11:Minimum permissible thickness of layer [79]*

This means that it is desirable to have some prior knowledge of the hardness of the film before testing. This is not always feasible, especially in the case of multilayer coatings.

So far the restrictions explained have been for data taken on plan-view films. Some data from Cu/Al samples was taken in cross section. Figure 3.12 shows that the layer needs to be twice the thickness of the indent.

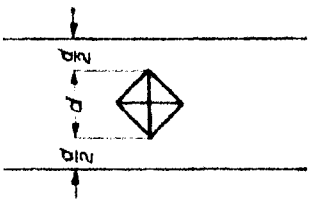

*Figure 3.12: The minimum permissible thickness of a cross-section film [79]*

For the Cu/Al coatings this at first was not possible and therefore extra thick coatings had to be made.

§

# Chapter 4

## *$TiB_2$/Al Multilayer Coatings*

Chapter 4 presents results from analysing $TiB_2$ /Al multilayer coatings. It begins with an introduction to the results chapter and also addresses the topics of layer uniformity, microstructure and composition. A special section is dedicated to the PEELS studies of $TiB_2$ itself, due to the interesting results that were obtained.

§

## INTRODUCTION TO RESULTS

Experimental work has been carried out on two different multilayer *systems*, $TiB_2$/Al and Cu/Al. Within those systems there have been different multilayer *sets*. For the purpose of this thesis a set means a multilayer coating of the same system but with differing individual layer thickness.

The results section consists of two separate chapters, one for each of the multilayer systems. These are preceded by an introduction which explains why we have been interested in the areas that have been studied. This has been put into a separate section to try to avoid the inevitable repetition that would occur due to similar studies on both types of material. There are also many experiments that have been done on only one of the systems, these will be explained in their respective sections.

There have been many debates over the years about why we see vastly improved properties with multilayer coatings. Factors quoted include; the pairing of certain materials [36], the individual layer thickness [31, 34] and the effects of the interfaces [43].

The objective of this project has been to study two multilayer systems one consisting of hard/soft layers and in contrast the other soft/soft. They have both been made using magnetron sputtering; however one using a balanced and the other an unbalanced configuration, as described in Section 2.1.2. We have been able to study the effects that these differences cause in such layered systems, and in particular have concentrated on the following aspects: uniformity, microstructure, composition, adhesion and hardness data.

The *uniformity* of the individual layers is imperative if the structure is to be classed as a multilayer coating. Primarily it was important to establish whether the coatings were in fact a sandwich of individual layers or perhaps consisted of just a single multiphase layer. Also the differences in the degree of uniformity seen in the layers was a priority to address, firstly between each multilayer set and then between the actual systems themselves. Comparisons between the two multilayer systems could divulge some information as to which process/system gives us the best uniformity.

The *microstructure* of the multilayer is paramount to the performance obtained, in its particular application. If we are to improve our understanding of these systems, the microstructure must be classified.

We have done this in a number of ways; by comparing structures seen to Thornton models, analysing grain size/shape and by classifying any preferred orientation within the films. Models predicting the microstructure in PVD methods have been well documented in the literature (see Section 2.2.1). To quantify grain size within the layers is not as simple as one would first imagine. With such structures, especially columnar structures, the grains can be ten times larger in one direction compared to another. Any preferred orientation of these grains is also important due to the anisotropic nature of such materials.

The *composition* of the individual layers is also of extreme importance to performance. Do we really have a sandwich of the materials we think we have? Is it possible that there is some mixing in the chamber, oxidation or diffusion between the layers, which could result in a structure that is not what was originally anticipated? Could this be an explanation as to why, in our case, we see vastly improved properties over the single layer counterparts?

It has been well reported that the interfaces between the layers are central to the performance of the coating (see Section 2.3.2). Firstly we set out to establish whether the interfaces are 'true' or if there is a mixing zone between the two. A zone of varying composition could have a dramatic

effect at the interface and is an area that has been studied extensively using the STEM.

*Adhesion* of the sandwich to the substrate is a necessity, and even though we have not had the capacity to carry out quantitative studies, microscopical analysis at the substrate/coating interface can reveal information about contamination. This could come as a result of poor cleaning or target contamination and could lead to poorer adhesion.

The *properties* of the multilayer must be an improvement over the substrate if it is to prove worth the expense and effort of producing the coating. There are many tests that could be carried out for wear, corrosion and hardness. Which to use, obviously depends on what improvement in properties one wishes to achieve. The work in Liverpool has concentrated on microstructural and compositional studies and, due to our limited equipment, physical property data has only been measured in terms of hardness. This has also been difficult due to achieve the relatively thin overall thickness of the film. Different techniques of measuring the hardness have been used, in some cases, both in plan view and cross-section. This has been done to test the validity of such data on a coating of this form.

## 4.0 Results from $TiB_2$ / Al Multilayer Coatings

The $TiB_2$ multilayer system has been studied using the samples that are summarised in Table 4.1. All of the $TiB_2$ samples have been made by balanced magnetron sputtering (as described in section 2.1.2.4). The quantity of samples available for study has been limited and it has been impossible to use all techniques available on all of the sets shown in Table 4.1. However information such as composition, interaction between the layers and microstructure provides a good comparison to the Cu/Al multilayers.

| Multilayer | Predicted thickness of $TiB_2$ | Predicted thickness of Al | Overall Thickness |
|---|---|---|---|
| ML54 | 200 nm | 200 nm | 4.8 μm |
| ML58 | 25 nm | 25 nm | 5 μm |
| MLO | 50 nm | 150 nm | 5 μm |

*Table 4.1: A table summarising the samples received for analysis.*

### 4.1 Uniformity and accuracy of layer thickness

The first technique used to establish whether the layers were distinct and not simply a multiphase coating (i.e. a mixture of two phases in a single layer), was Auger microscopy.

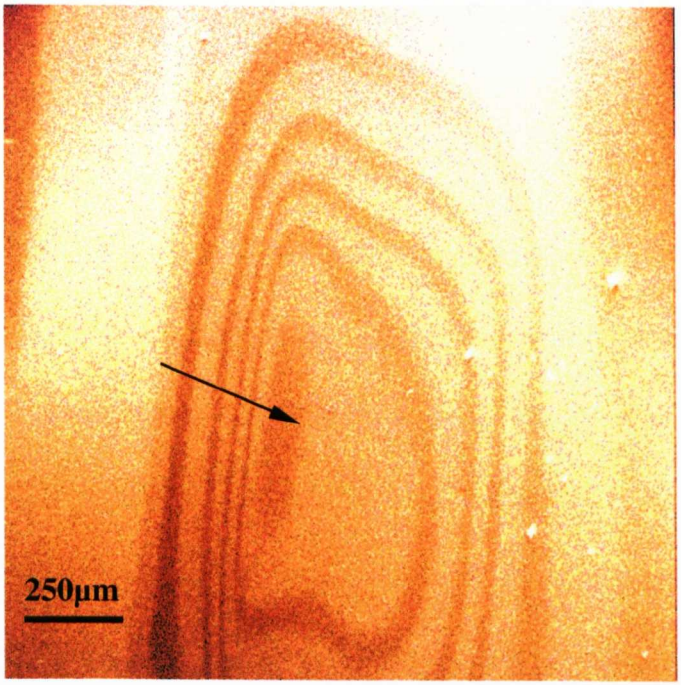


*Figure 4.1(a): Plan view image of crater*

The ion gun (as described in Section 3.2.1) was used to *drill* a small crater into the surface of the coating. Figure 4.1(a) shows the result of such a procedure and below (Figure 4.1(b)) is a schematic diagram in cross-section, to illustrate such a crater. It is possible, after ion drilling, that oxidation of the surface is enhanced and this may be a reason why we see

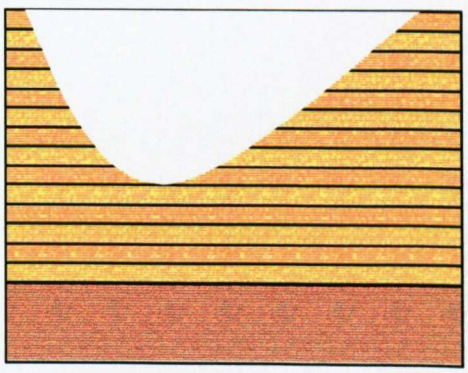

*Figure 4.1(b) Schematic of the crater*

such differences in contrast, in the secondary electron image (Figure 4.1(a)).

The existence of distinct, individual layers is revealed by such a crater experiment. Also, by using the analytical capabilities of the machine, elemental maps (Figure 4.2) demonstrate that these layers alternate in composition. Even though this is only a qualitative study, it can be deduced that the coating consists of alternating titanium/boron and aluminium rich layers. More detailed analysis of these samples by Auger electron spectroscopy are given in Section 4.3.

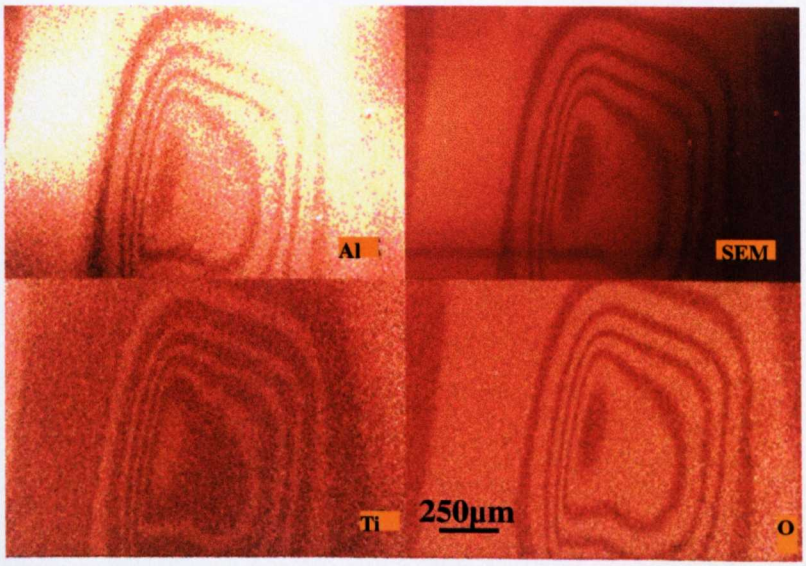


*Figure 4.2: Auger Maps*

For a more accurate picture of uniformity, and to enable us to get information of microstructure on such small-scale layers, it was inevitable

that Transmission Electron Microscopy (TEM) would be our most useful tool. Primary studies confirmed, what initially was seen in the Auger microscope, the existence of alternating layers. This is illustrated in Figure 4.3, which is ML54 (~200nm $TiB_2$ /200nm Al nominal). Such an image shows that the predicted individual layer thickness is inaccurate in this region.

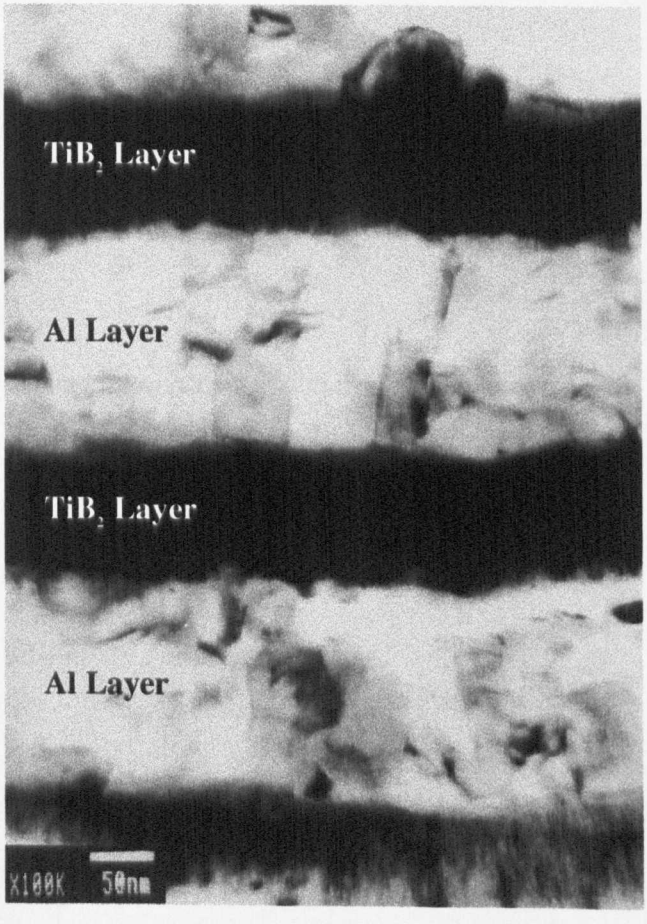


*Figure 4.3: ML54 TEM Micrograph*

Sample ML58 (~25nm $TiB_2$/25nm Al) had much thinner layers but was on a steel substrate and therefore difficult to image. Even so, Figure 4.4 shows an image of such a sample, the slight 'blurring' is due to the magnetic nature of the substrate hindering the astigmatism correction. However it does reveal the individual layers, but not of the uniformity or consistency of ML54.

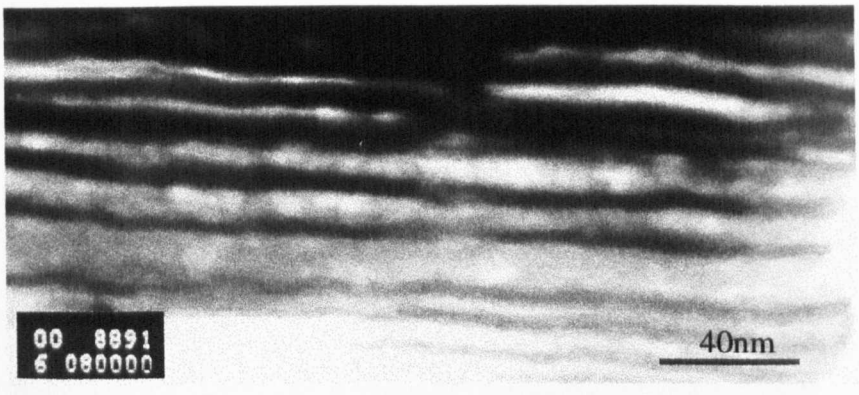


*Figure 4.4: ML58 TEM Bright-field Micrograph*

The accuracy (or otherwise) of the predicted individual layer thickness for ML54 are shown below in Table 4.2.

| Layer | Predicted (nm) | Average from experimental data (nm) | Standard Deviation |
|---|---|---|---|
| Al | 200 | 152 | 1.6 |
| $TiB_2$ | 200 | 149 | 1.1 |

*Table 4.2: Predicted and average measured layer thickness for ML54*

## 4.2 Microstructure

### 4.2.1 Grain Size/Shape and Form

Figure 4.5 shows a high magnification image of a titanium diboride layer, in which the grains are very fine and columnar. On closer inspection tapered columns are seen, indicating a zone 1 structure (zone notation is defined Section 2.2.1 [18]). The aluminium layers, however, have a much larger grain size and even though columns can be seen, in contrast to $TiB_2$ they are not tapered, and are more reminiscent of zone 2 type structures.

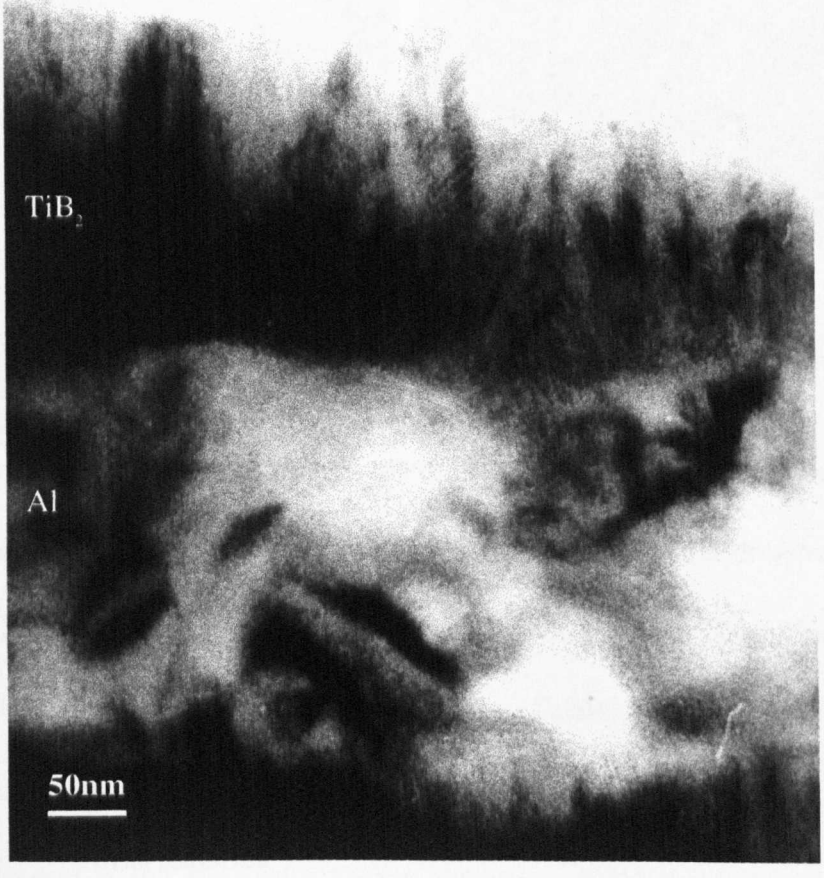


*Figure 4.5: $TiB_2$ layer (ML54)with zone 1 type structure*

The grain sizes for the individual layers are shown in Table 4.2. The aluminium layers were quite straightforward to establish, with distinct boundaries seen. Figure 4.6(a) shows those grains in a typical image, which has been used for such calculations.

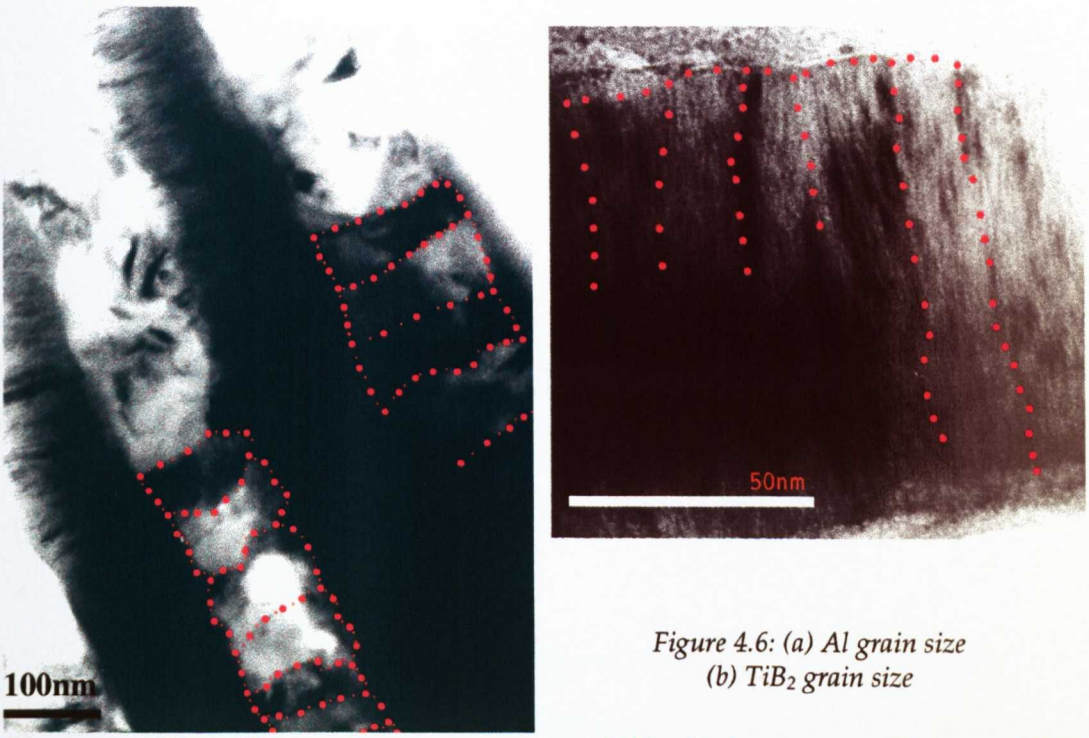


*Figure 4.6: (a) Al grain size*
*(b) $TiB_2$ grain size*

However, the $TiB_2$ grains were more difficult to image, Figure 4.6(b) shows the areas taken to be individual grains. Changes in *direction* was taken to indicate a new grain. Some grains extend the total thickness of the individual layer in which they reside. Table 4.3 shows the average grain sizes for both of the layers.

| Layer | Grain Width (nm) |
|---|---|
| $TiB_2$ | 17nm |
| Al | 62.5nm |

*Table 4.3: Grain Sizes*

## 4.3. Compositional analysis

### 4.3.1 Auger

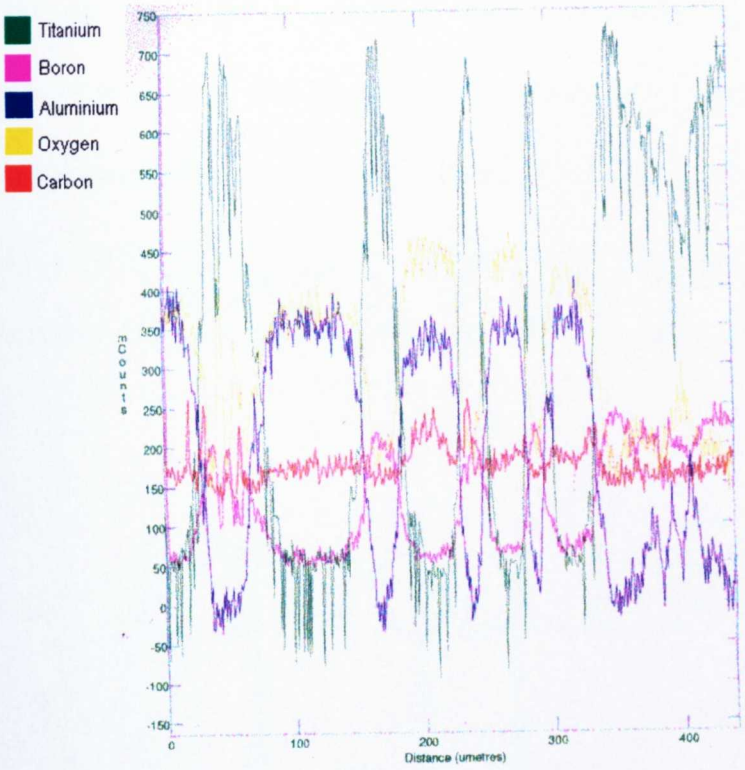


*Figure 4.7: Linescan across Auger crater*

Initial work on the coatings was carried out in an Auger microscope. Elemental linescans across the hole that was drilled (as explained in Section 4.1.) are shown in Figure 4.7. The position of the scan is shown in Figure 4.1. The interfaces are reasonably sharp, although using this technique interactions between layers are difficult to assess due to cross sputtering that occurs during the production of the hole. It comes as no surprise that the oxygen trace follows the aluminium trace very closely, however it is difficult to tell by this technique, whether this is simply a surface effect, or oxygen incorporation in the bulk.

### 4.3.2 XRD

To complement the Auger analysis it was thought that the XRD would be a good tool to establish whether the aluminium layer has oxygen incorporated within it. The majority of the sample analysed in XRD could not have been exposed to the atmosphere. This holds a distinct advantage over studies with TEM or Auger samples, which have exposed layers that are inevitably prone to surface oxidation.

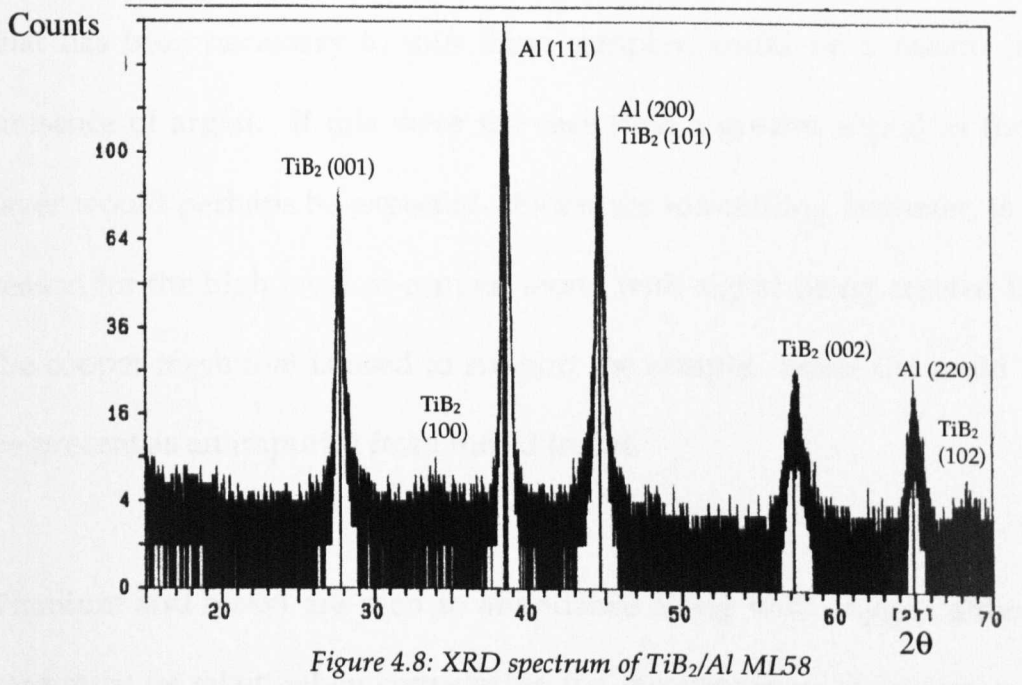


*Figure 4.8: XRD spectrum of $TiB_2$/Al ML58*

Figure 4.8 shows a typical XRD profile taken under conditions as explained in Section 3.3. It confirms that the layers are crystalline and shows the presence of aluminium and titanium diboride peaks. The lack of peaks from other compounds initially suggests that no other phases are present. This, of course, is within the limits of detection of this technique. This been further investigated in following sections.

### 4.3.3 STEM

Figure 4.9 shows a typical EDX point analysis in the $TiB_2$ layer. All the raw spectra were taken for 100 seconds, with the spectrometer optimised for the detection of boron. The first striking feature is the presence of argon, especially in the $TiB_2$ layer. Such an incorporation would be more expected in a sample that has undergone some bombardment, such as with an unbalanced magnetron process. The large amount of ion-milling that has been necessary to thin these samples, could be a reason for a presence of argon. If this were the case then a greater signal in the Al layer would perhaps be expected. Extensive ion-milling however, is one reason for the high level of copper, along with signal being created from the copper mesh that is used to support the sample. Some Cu could also be present as an impurity from the Al target.

Titanium and boron are seen in abundance along with oxygen although care must be taken when considering the incorporation of oxygen in the $TiB_2$ layer due to the strong overlap of the O-K and Ti-L edges. More investigation was necessary to decipher whether this was an oxide layer, especially considering the materials involved and their high affinity for oxygen. There is also a small percentage (of similar amounts) of Al in the $TiB_2$ layer and vice-versa, which could be due to cross-sputtering or ion-milling.

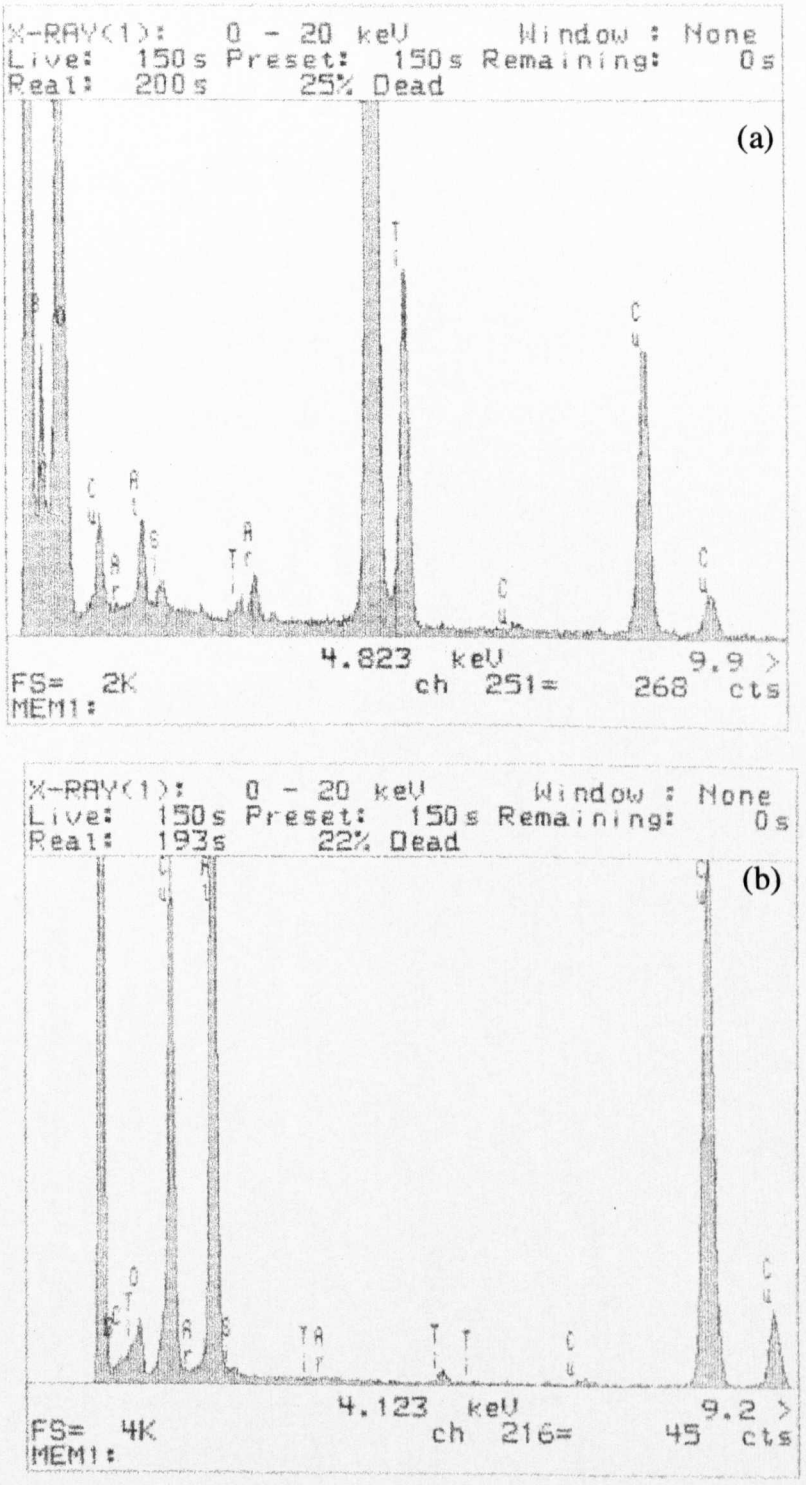


*Figure 4.9: (a) EDX from $TiB_2$ layer (b) EDX from Al Layer*

#### 4.3.3.1 Interface between layers

Figure 4.10 shows a STEM elemental EDX linescan as described in Section 3.2. The beam was scanned along a line as indicated by the arrow on the image. It starts in a $TiB_2$ layer and traverses across the interface into an adjoining aluminium layer. The eight numbered boxes show the subsequent X-ray traces that are created, the vertical line in the centre denotes the point at which the beam crosses the interface. The elements to which these traces relate, are listed in the top left hand corner, along with the number of counts obtained at the interface and the full-scale of each individual trace.

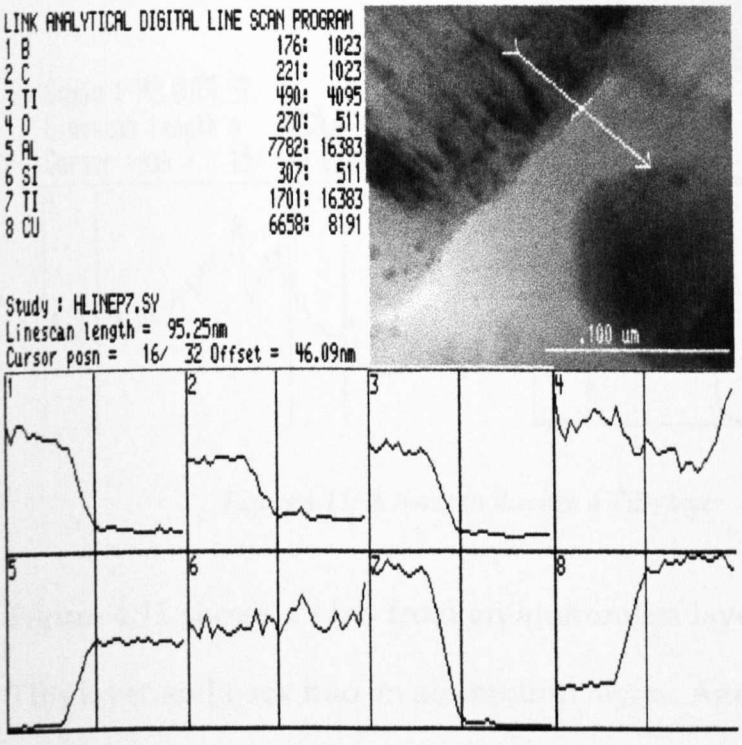


The carbon signal seems to be associated with the $TiB_2$ layer, however this is most likely to be due to the inevitable overlap of the C-K and B-K edges. There is also a presence of Si, thought to be an impurity in the Al target.

Slight overlap of the elements at the interface is seen, but it is both small and consistent in both directions. This is therefore more likely to be as a consequence of the interface not being exactly parallel to the beam, rather than conclusive proof of intermixing. Finding a parallel interface is not an easy task in any microscope, and is hindered even more in the STEM due to the small range of tilting that is available.

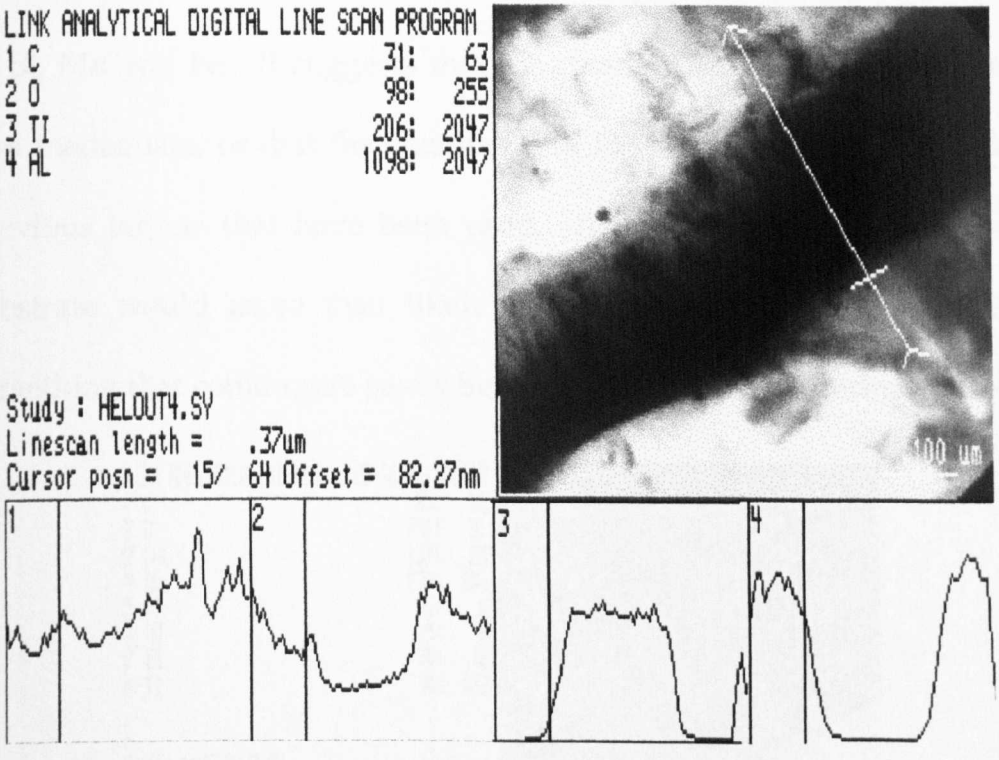


*Figure 4.11: A linescan through a $TiB_2$ layer*

Figure 4.11 shows a scan from an aluminium layer completely through a $TiB_2$ layer and back into an aluminium layer. Again slight overlap is seen but it is small and consistent.

#### 4.3.3.2 Substrate/Coating Interface

Figure 4.12 shows another linescan but this time it starts in the Cu substrate, goes through the coating interface and also the first $TiB_2$ layer. The interface between the first $TiB_2$ and first Al looks uneven, suggesting some intermixing, however such interaction is not seen in subsequent layers. It also seemed that there was a small zone between the coating and the substrate. This zone consists of many different elements such as O, Si, Mn and Fe. It suggests that the cleaning process of the substrate was inadequate, or that the chamber still has amounts of elements from previous targets that have been used. Adhesion of the coating to the substrate would more than likely be affected by this zone and it is something that could quite easily be improved in this sputtering process.

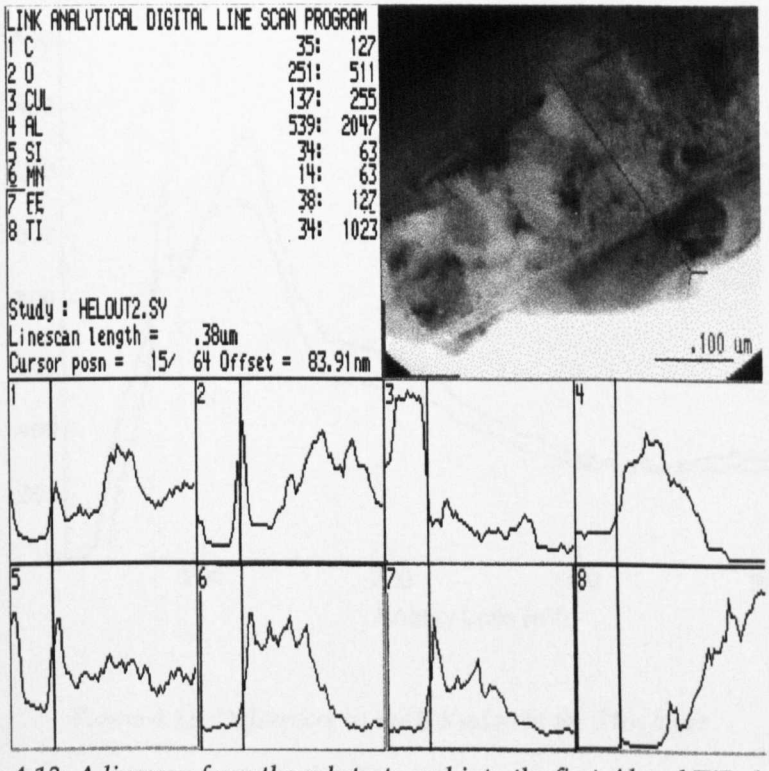


*Figure 4.12: A linescan from the substrate and into the first Al and $TiB_2$ layer*

### 4.3.4 PEELS

The effectiveness of PEELS in analysing the structure of compounds, especially those containing light elements such as boron, has been well-reported (see Section 2.4). After carrying out analysis on several areas in the $TiB_2$ layers it became apparent that different regions gave a range of ELNES (energy-loss near-edge structure) on the boron K-edge. This was unexpected, as differences in the B K-edge in $TiB_2$ have not been reported before, even though it has been the subject of ELNES analysis previously [80]. This may be due to the fact that, in this case, the sample is a highly textured coating of $TiB_2$ with a very small grain size. It became a prime goal to establish exactly why such changes have now become apparent

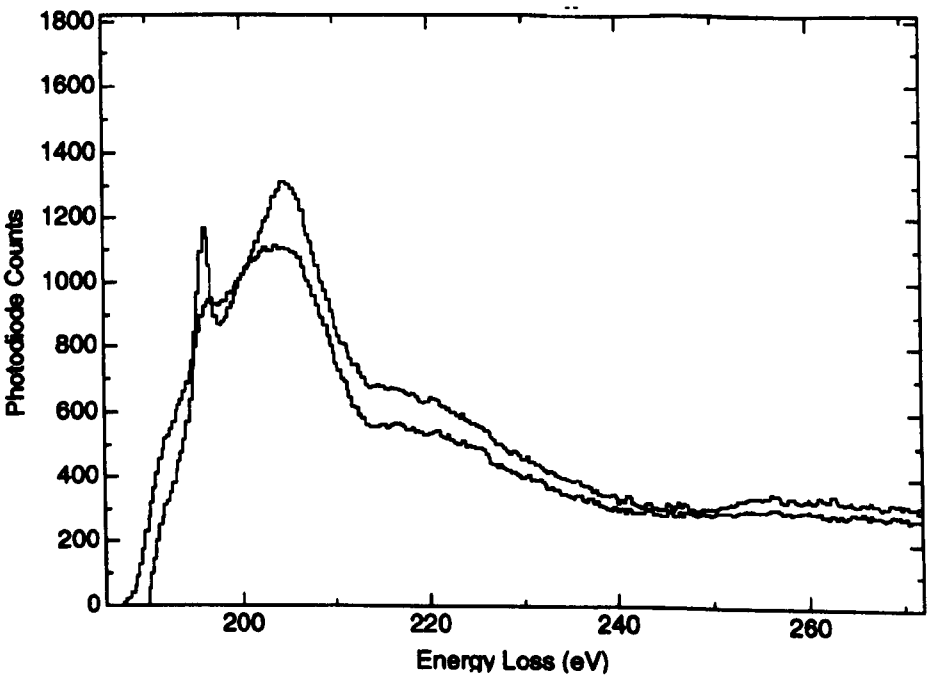


*Figure 4.13: Differences in the B K-edge in the $TiB_2$ layer*

and of course, explain the origin of them.

The differences in the B K-edges that are obtained from different regions of the layer are shown in Figure 4.13. These changes seemed to relate to contrast changes in the image, with darker areas producing different spectra to light regions. Some spectra collected were similar to that found in the literature for $TiB_2$, while others showed features more reminiscent of the fine structure from borate glasses [80].

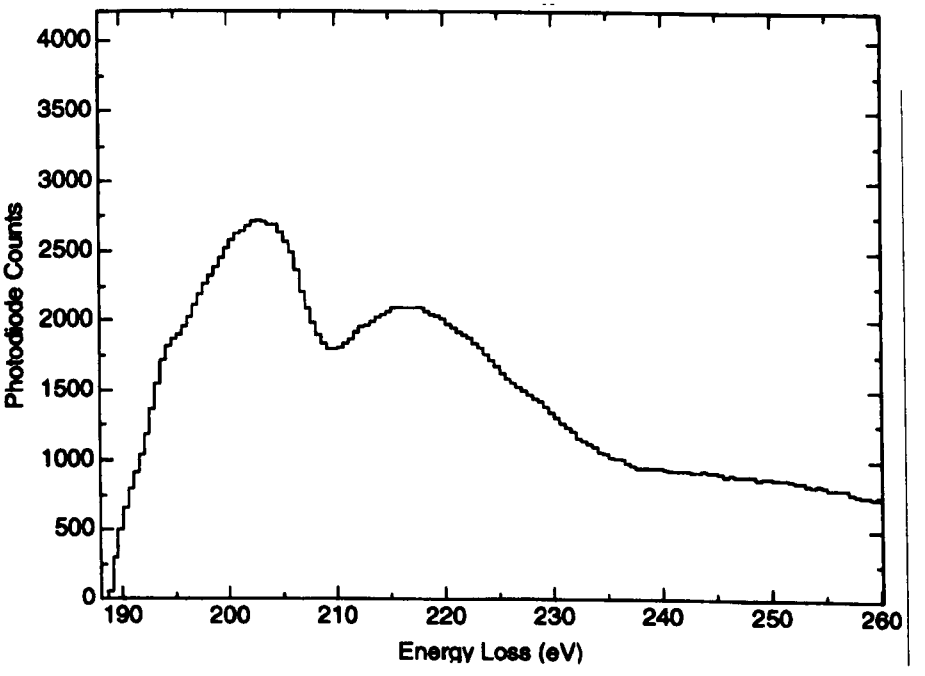


*Figure 4.14: A B K-edge from a powder standard*

To confirm the features of the edge obtained from the literature it was thought necessary to prepare a standard of $TiB_2$. A polycrystalline powder sample was used and a typical spectrum is shown in Figure 4.14. The spectrum has similar features to the literature standard, and to some

of the edges from the multilayer coating. Therefore it became necessary to address possible reasons that could contribute to the changes in edge structure.

#### 4.3.4.1 Effect of Ion-Beam Thinning

The main difference between the multilayer and the $TiB_2$ standard was that the multilayer had been subjected to ion beam thinning. Previous STEM work in Figure 4.9 showed that there were relatively large amounts of copper and argon, suggesting substantial ion beam damage. Perhaps this could have some effect on local bonding/structure and hence on the ELNES. It was consequently decided to sputter a very thin, electron transparent layer of $TiB_2$ under the same conditions as the multilayer. It

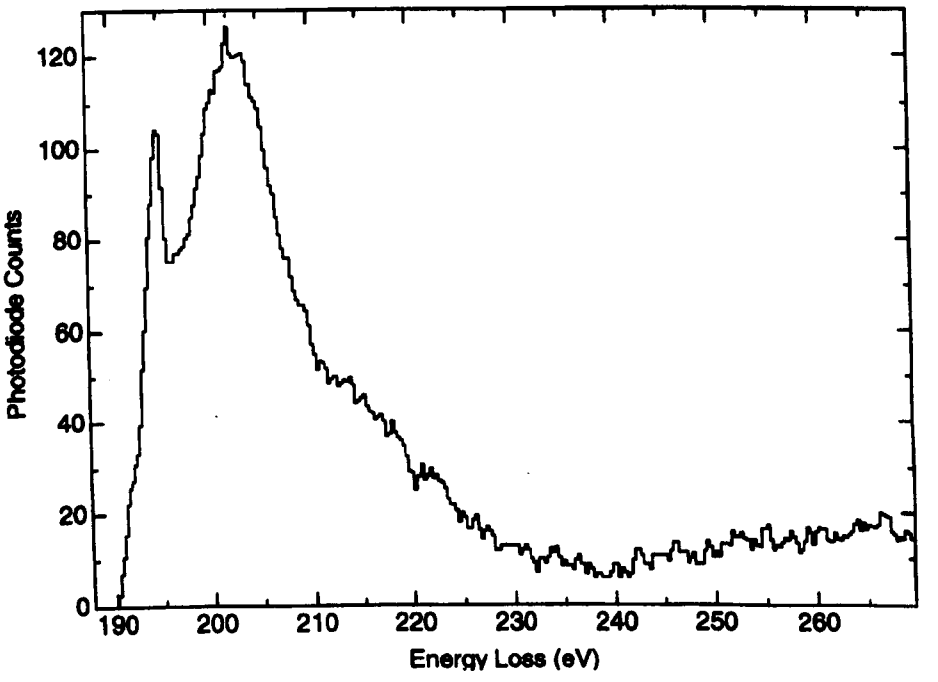


*Figure 4.15: Electron transparent $TiB_2$ thin film*

was deposited on a glass slide, from which it could be floated off onto a copper support grid. A typical spectrum from this sample is seen in Figure 4.15.

Once again a range of fine structure with features more pronounced than in the powder standard are observed. It was concluded that ion beam thinning was not the main factor in the spectral variations.

#### 4.3.4.2 Effect of Beam Damage

It was thought that perhaps taking several spectra in adjacent regions of the sample could have damaged it. It was necessary to check that this was not the reason for edge variations. Therefore a spectrum was acquired for 10secs, then immediately afterwards another was taken. Figure 4.16 shows the result, hence beam damage was also considered insignificant in causing the variations.

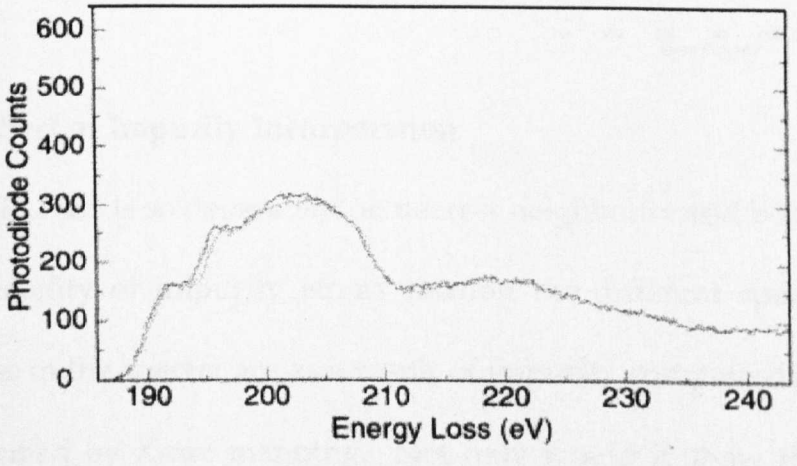


*Figure 4.16: The effect of beam damage*

#### 4.3.4.3 Effect of Sample Thickness

The sample thickness was thought unlikely to have an effect on the edge and this is confirmed in Figure 4.17. The spectra were taken along a region of similar contrast in the same grain, from the bulk towards the thin edge of the wedge. The shape of the B K-edge remains unaffected until the thinnest edge of the sample is analysed. The change in this region is thought to be due to the presence of an oxide layer surrounding the bulk. All the other spectra seem relatively unaffected and as expected the effect of thickness is minimal.

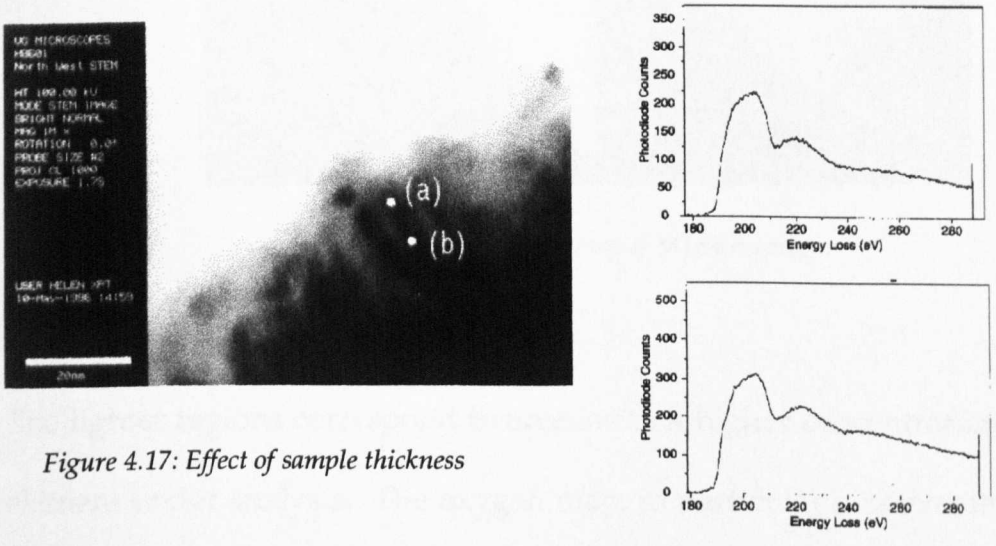


*Figure 4.17: Effect of sample thickness*

#### 4.3.4.4 Effect of Impurity Incorporation

Because ELNES is so dependent on nearest neighbours and bonding, there is a possibility of impurity atoms causing the different spectra. If the variations in the spectra are as a result of impurity compounds, this could be confirmed by X-ray mapping. Not only would it show the elements

present, but also indicate if there any preferential sites at which they are situated. Figure 4.18 shows such a map.

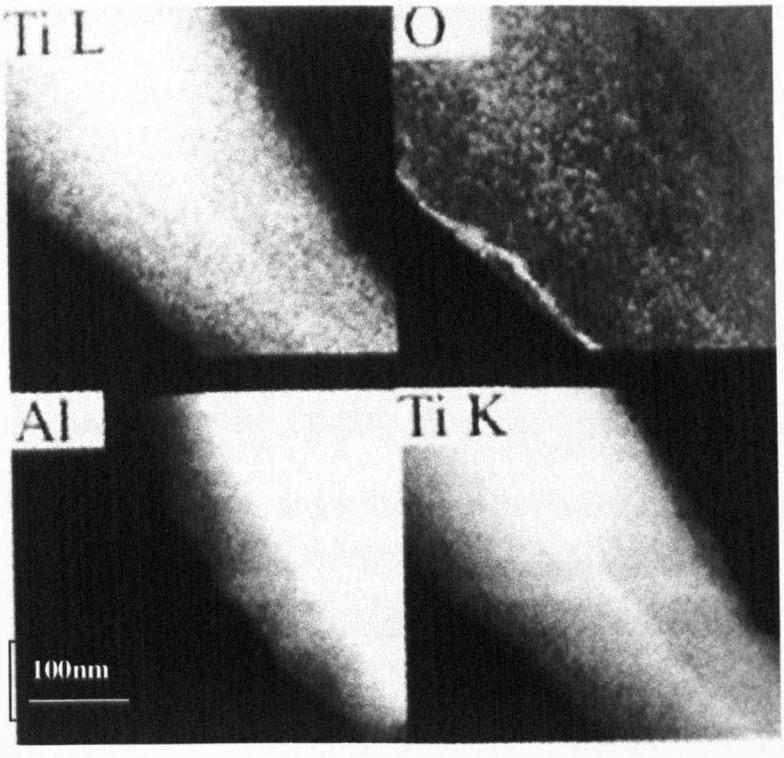


*Figure 4.18: X-ray map of ML54 coating*

The lighter regions correspond to areas with a higher concentration of the element under analysis. The oxygen map, in particular is interesting as it shows a presence in the $TiB_2$ layer as well as the aluminium. However, the most likely explanation for this, is that both titanium and aluminium have a large oxygen affinity and hence these could both be surface layers, other reasons are discussed in Chapter 6. Therefore, although incorporation of oxygen cannot be totally discounted, it seems unlikely that it is the sole reason for such B-K edge variations.

#### 4.3.4.5 Effect of Orientation

It was noticed that shape changes seemed to depend on the contrast in the image, and hence possibly the orientation of the sample with respect to the incident electron beam. To ensure that spectra were taken from the same grain, both before and after tilting, it was decided to carry out experiments on a single crystallite in a powder sample.

Figure 4.19(a) shows a spectrum with its respective diffraction pattern, the electron beam is parallel to the <$1\bar{2}1\bar{3}$> direction. Figure 4.19(b) shows a spectrum with the sample several degrees of tilt away from this axis.

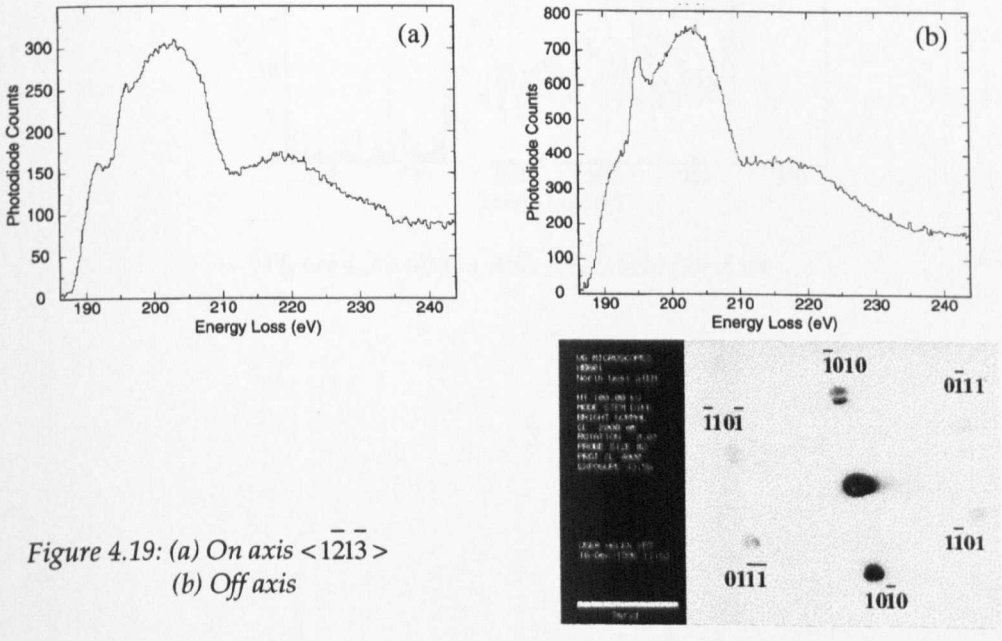


*Figure 4.19: (a) On axis <$1\bar{2}1\bar{3}$> (b) Off axis*

The change in the ELNES seen between these spectra demonstrates the dependency of the B K-edge on orientation with respect to the electron beam. Due to the previous studies of impurities in the samples it was

thought necessary to prove that these changes are independent of oxygen levels.

Figure 4.20(a) and (b) show the associated oxygen K-edges to the spectra presented in Figure 4.19. There is a small level of oxygen in each case, but the oxygen/boron ratios are constant, within experimental error.

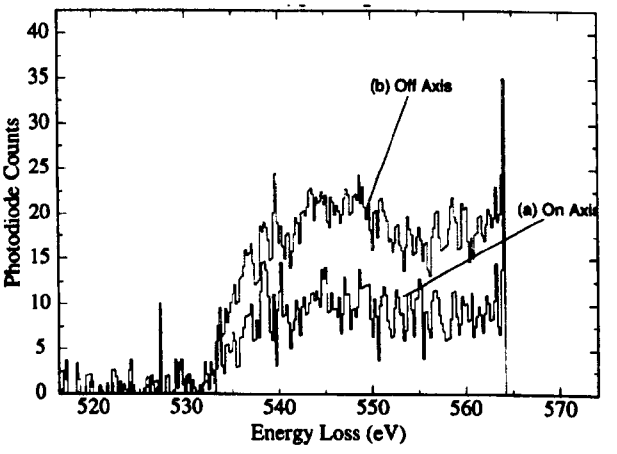


*Figure 4.20: (a) On Axis <1$\bar{2}\bar{1}$3>(b) Off Axis*

§

## 4.4 Summary of $TiB_2$/Al Results

The research started with primary Auger studies, which proved that the layers were of varying composition. Beyond this however, it became necessary to use transmission electron microscopy to obtain more detailed analysis.

TEM analysis confirmed that the layers were distinct, periodic and of a reasonable uniformity. XRD spectra confirmed that the layers were, as anticipated $TiB_2$/Al.

Linescan studies showed no clear evidence of interactions between the individual layers nor the presence of an interface zone. However, inadequate substrate cleaning was uncovered. This could have a detrimental effect on adhesion of the film.

Due to sample shortage, the focus of the project changed direction to study the B K-edge in $TiB_2$. Differences seen in the ELNES of this edge warranted further investigation, as such effects had not been reported previously. Reasons for the differences were addressed including; ion beam thinning, beam damage, sample thickness, incorporation of impurities and the orientation of the sample with respect to the electron

beam. The latter effect, is considered to be the major factor in producing the variation in fine structure of the B K-edge.

§

# Chapter 5

## *Cu/Al Multilayer Coatings*

Chapter 5 contains the results of studies on Cu/Al multilayer coatings. Uniformity and microstructure are considered but most of this chapter is devoted to the identification of phases within individual layers and interactions between them. The chapter concludes with brief but informative studies on the hardness performance of this system.

§

## 5.0 Results of Cu/Al Multilayer Coatings

The Cu/Al multilayer set has been studied using four types of coatings with differing individual layer thickness but mainly with a similar overall coating thickness. The coatings used are summarised in Table 5.1.

| Multilayer | Predicted thickness of Cu Layers | Predicted thickness of Al Layers | Overall thickness |
|---|---|---|---|
| ML1 | 253nm | 68nm | 4.8μm |
| ML2 | 908nm | 251nm | 13.7μm |
| ML3 | 24nm | 7nm | 14μm |
| ML5 | 34nm | 9nm | 13μm |

*Table 5.1: A table to summarise the predicted individual coating thickness.*

## 5.1 Uniformity and accuracy of layer thickness

Examples of the uniformity and existence of the individual layers are seen in Figures 5.1, 5.2 and 5.3 which relate to the multilayers systems ML2, ML1 and ML3 respectively. According to the growth data in table 5.1, the lighter layers will be Al and the darker Cu. ML5 unfortunately could not be studied due to its poor adhesion to the substrate.

During the coating process the individual layer thickness of the coating are determined by the speed of rotation of the substrate table, the chamber

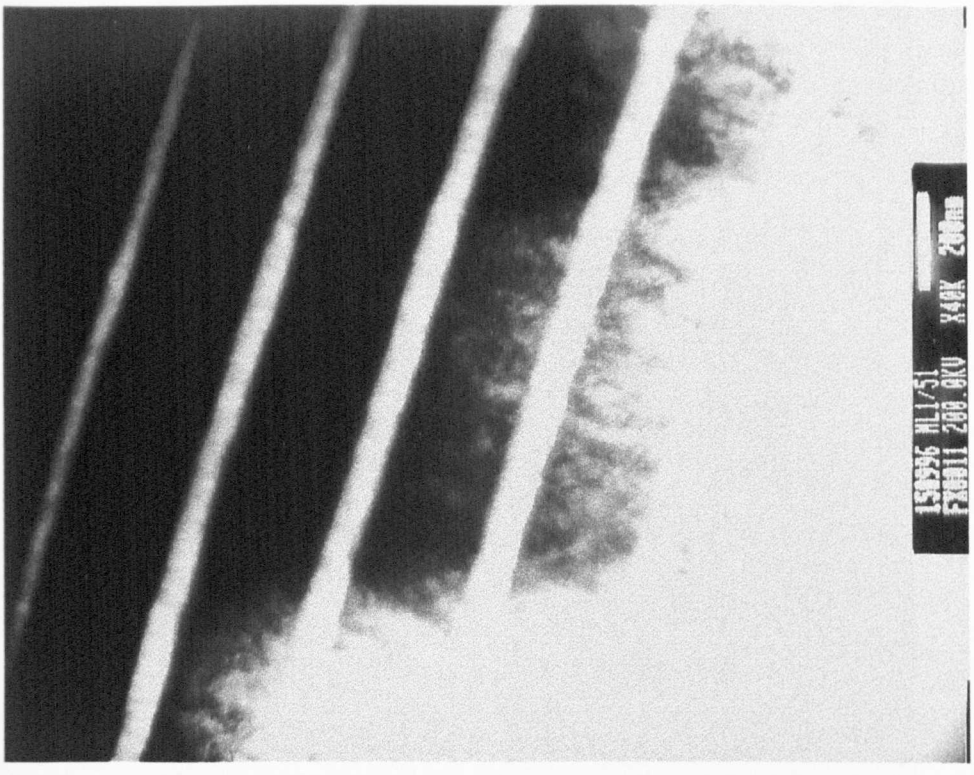

*Figure 5.2 : Low Magnification Image of ML1*

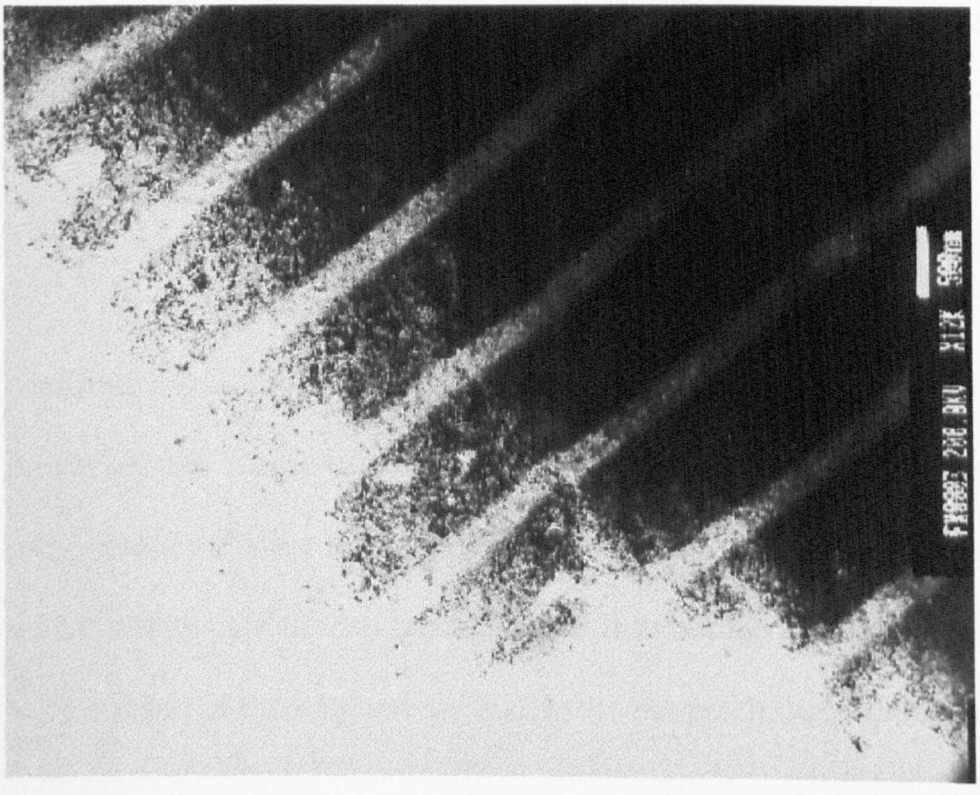

*Figure 5.1: ML2 Low Magnification Image*

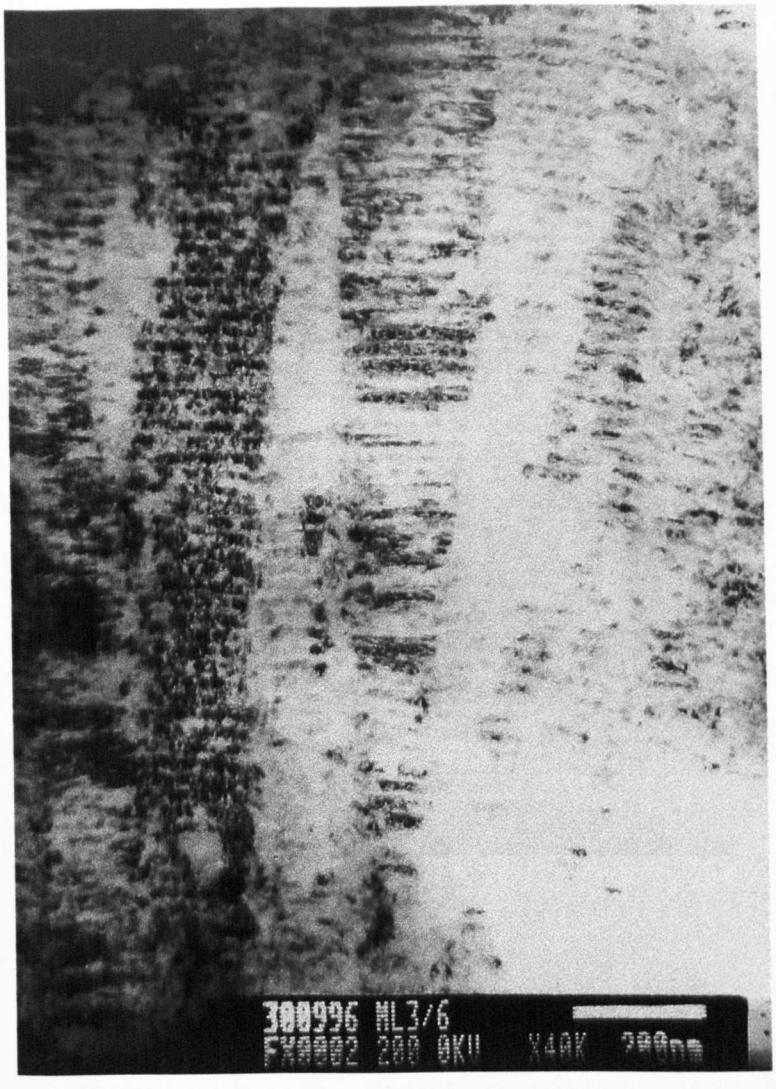


*Figure 5.3: A low magnification image of ML3*

conditions and the power of the magnetrons. The importance of the power of the magnetrons is illustrated in Figure 5.4. The layers get progressively thicker from the substrate and then reach a maximum size, which is then carried through the rest of the coating. This effect is thought to be a result of the magnetrons taking time to reach their optimum

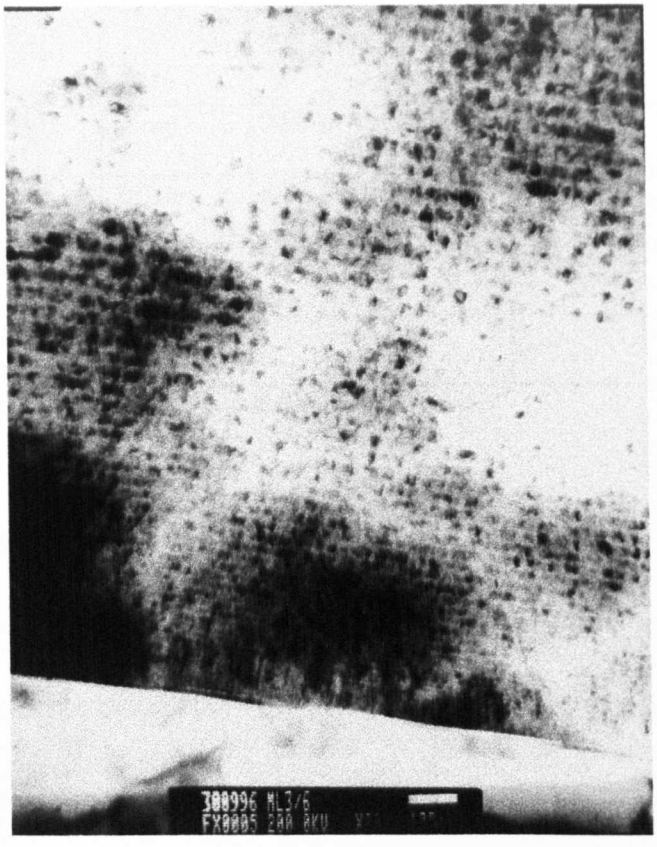


*Figure 5.4: ML3 at the coating/substrate interface, showing the layers getting progressively thicker*

performance. Therefore it is conceivable that there will be discrepancies between the predicted thickness and the actual thickness. Table 5.2 shows a comparison between the predicted thickness and the average measured thickness using TEM cross-sections. In each case, when one layer of the coating was thicker than predicted, so was the layer of alternate composition and vice-versa. The accuracy of the microscope calibration was checked and adjusted, where necessary, using a standard grating.

| Multilayer | Predicted Cu | Predicted Al | Actual Cu | Actual Al | Percentage Error Cu | Percentage Error Al |
|---|---|---|---|---|---|---|
| ML1 | 253nm | 68nm | 240nm | 67nm | -5% | -1% |
| ML2 | 908nm | 251nm | 835nm | 210nm | -8% | -16% |
| ML3 | 24nm | 7nm | 26nm | 8nm | +8% | +10% |
| ML5 | 34nm | 9nm | | | | |

*Table 5.2: Comparison of the predicted and actual layer thickness.*

## 5.2 Microstructure

Cross-sectional TEM samples were made for all the coatings to enable the study of the microstructure. Figure 5.5 shows a copper/aluminium interface of ML2.

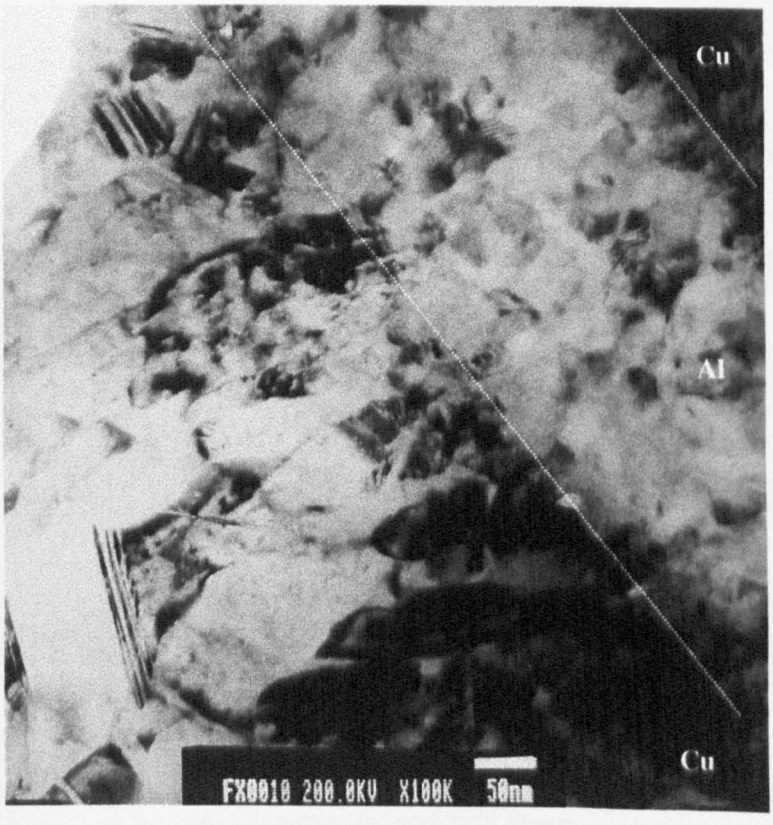


*Figure 5.5: A copper/aluminium interface in ML2*

ML2 (~908nm Cu/251nm Al) was used for all the primary studies due to it having the largest individual layer thickness and hence was easier to analyse. The first thing to notice is that the copper grains are much larger than their aluminium counterparts. This makes them easier to define and it is clear that they are not all of a uniform size.

On close inspection of Figure 5.5, zones are seen at the interface between the copper and aluminium layers. This was initially thought to be a mixing zone and has been studied in more detail in Section 5.3.1. There is also evidence of twinning in the copper layer.

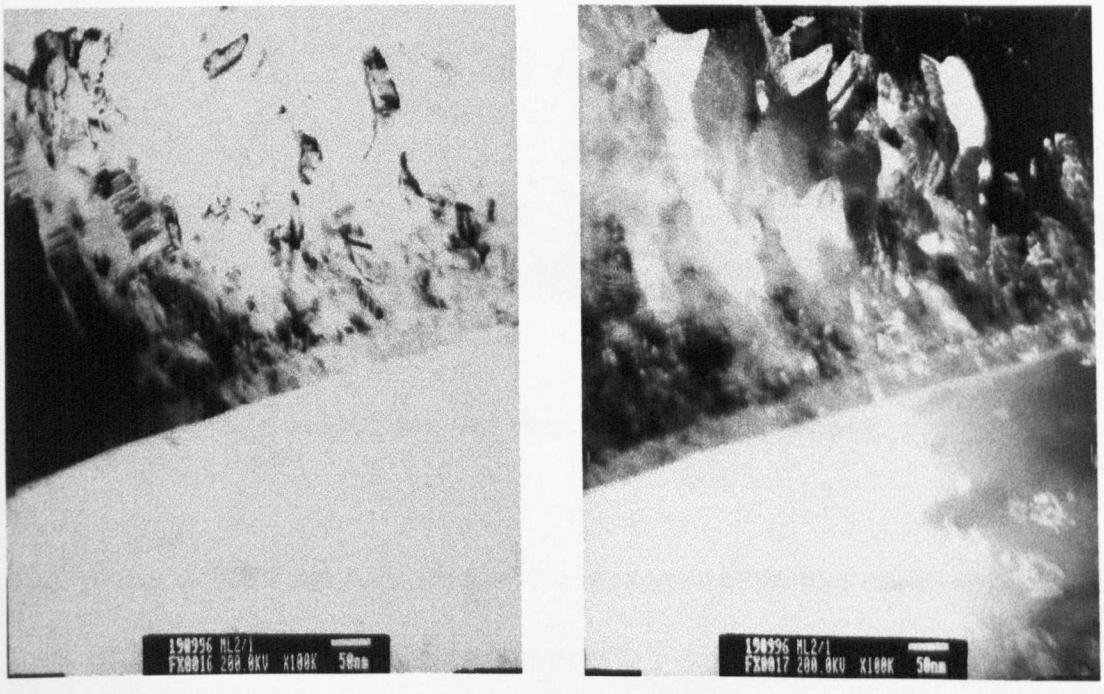


*Figure 5.6: (a) Bright field image of the substrate/coating interface of ML2*
*(b) The respective dark field image*

On close inspection of lower magnification images such as Figure 5.6, many 'column stacking' features are seen in the copper layers of ML2. Figure 5.7 shows a higher magnification dark field image of such a feature

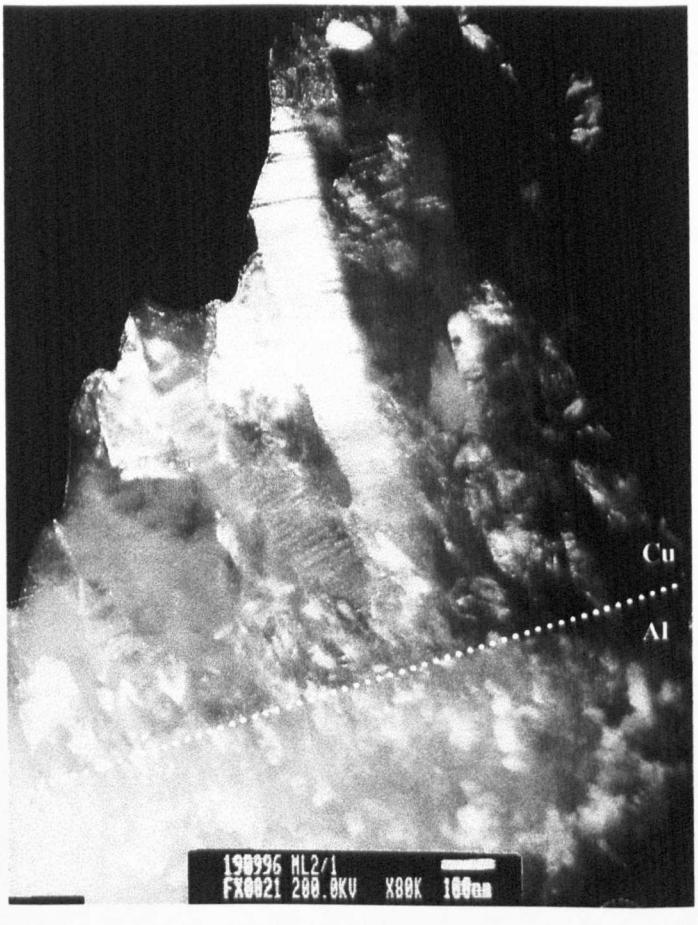


*Figure 5.7: A dark field image showing column-stacking faults*

The 'plates' within the column show a strong orientation relationship. At first, such faults were thought to be possibly microtwins, however Figure 5.8 shows a higher magnification micrograph of ML2 with a fault adjacent

to a twin. They are clearly different and remain so even on tilting the sample.

ML3 (~24nm Cu/7nm Al) also has column features that seem to carry through a multitude of individual layers (Figure 5.3). Such features, analogous to columnar grains, run throughout the superstructure. However, such features are not present in the close proximity of the substrate (Figure 5.9), they only reside in the final two-thirds of the total thickness of the film.

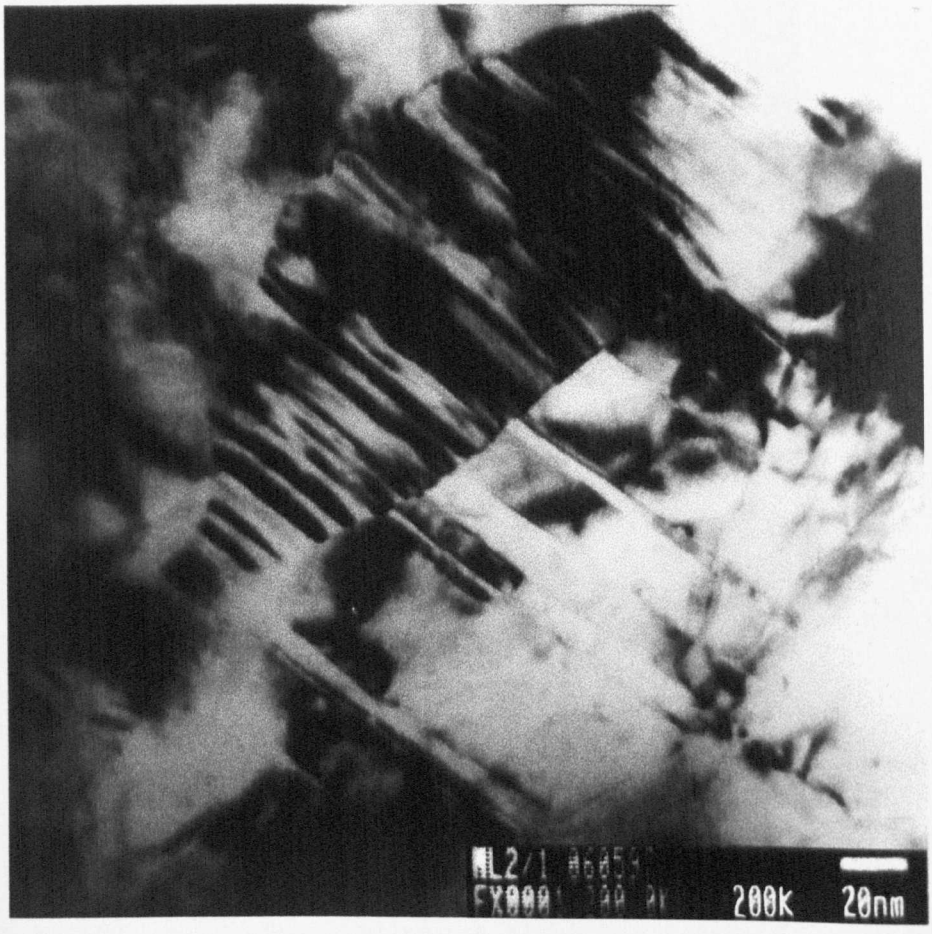


*Figure 5.8: Comparison of a staking fault and twin*

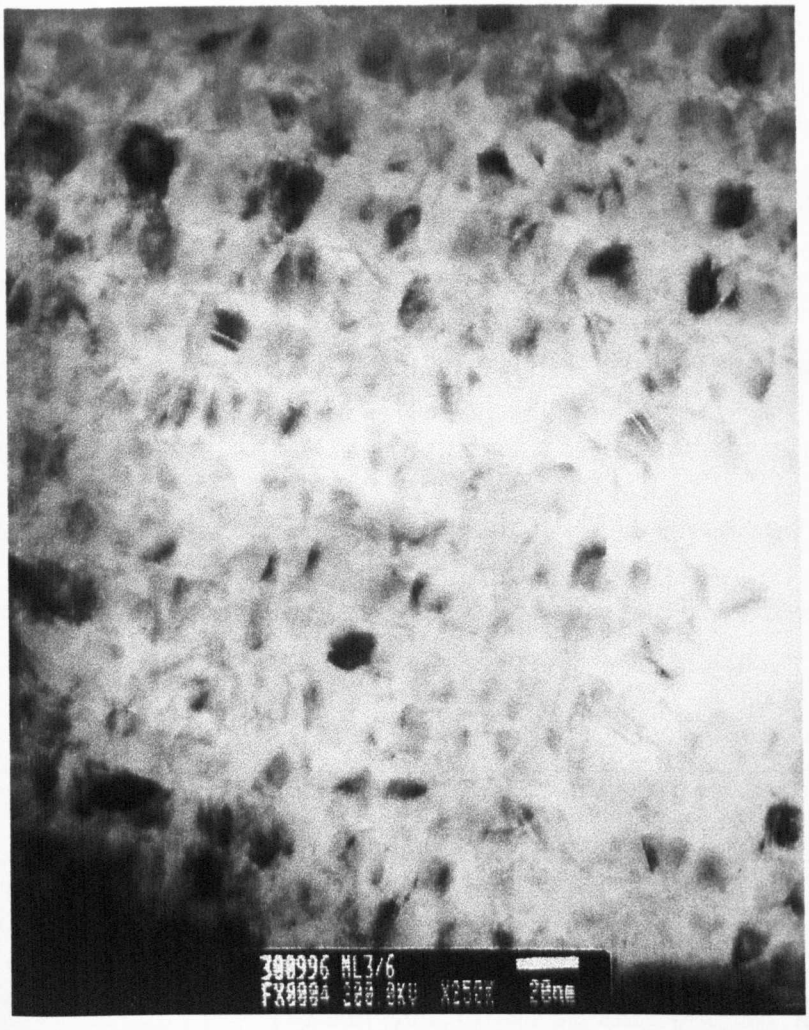


*Figure 5.9: ML3 close to the substrate*

### 5.2.1 Grain Structure

The grain size for all of the coatings has been difficult to define and subsequently we have used dark-field imaging to aid this goal. Figure 5.6 (a) and (b) shows an example of an image in bright field and dark field respectively. The measured grain sizes are contained in Table 5.3 for each of the coatings. It was considered impractical to average the grain size measurements. In ML2, the Cu grains had a wide variety of sizes and in ML3 the grains were indistinguishable in the Al layer and hence it is assumed that they extend the length of the individual layer thickness.

| Multilayer | Cu Grains (nm) | Al Grains (nm) |
|---|---|---|
| ML2 | ~80nm wide, up to layer thickness in length | ~30nm |
| ML3 | ~20nm wide, extend the full layer thickness | Assumed that they extend the full layer ~7nm |

*Table 5.3: Study of grain sizes*

The shape of the grains is easier to define. Figure 5.7 illustrates this for ML2, in the copper layers a classic columnar structure relating to zone 2 (defined as described in Section 2.2.1) is seen. In contrast the aluminium is more reminiscent of a zone 3 fully equiaxed structure (Figure 5.10). The shape and size of the grains in ML3 however, are very hard to establish.

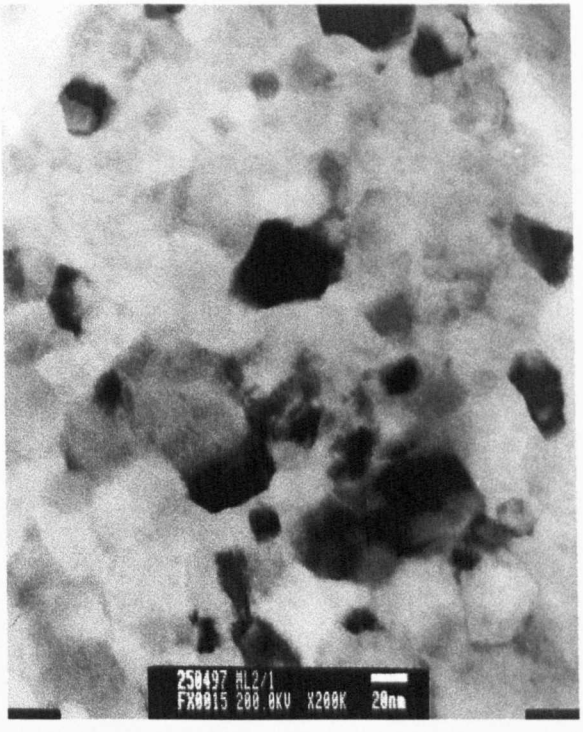


*Figure 5.10: ML2 showing the fully equiaxed structure in the aluminium layer*

### 5.2.2 At the Substrate

In the first layer of the coating, a structure can be seen for ~50 nm that is different to the bulk. This is thought to occur until the coating is thick enough to lose the influence of the underlying substrate, Figure 5.6 shows this for ML2.

### 5.2.3 Orientation

Figure 5.11 shows a selected area diffraction pattern of ML3 along with an image of the area where it was taken from (this is indexed in Figure 5.20).

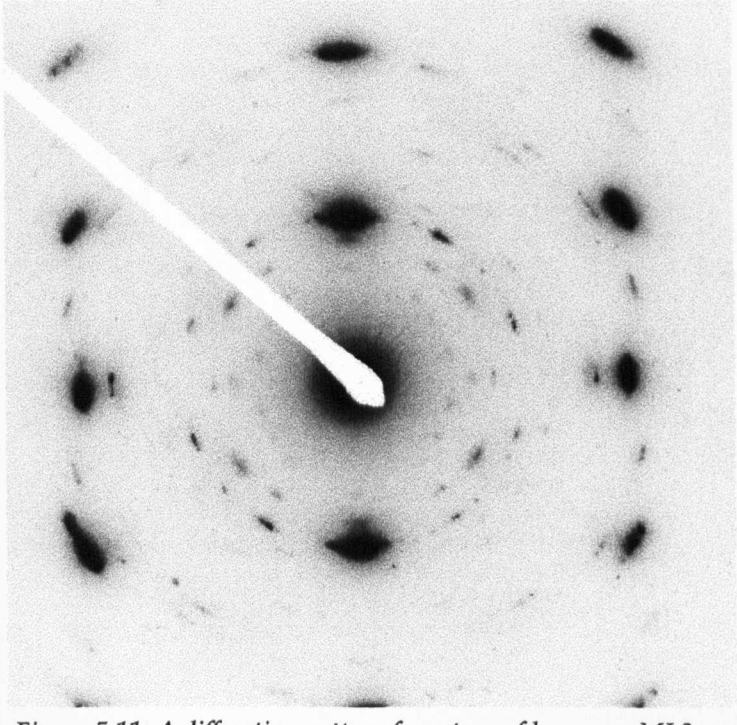

*Figure 5.11: A diffraction pattern from tens of layers on ML3*

The copper layers seem to be orientated with (111) // to the substrate and the aluminium (111) // to the substrate. This selected area pattern will have sampled tens of layers and yet a pattern with a distinct preferred orientation of both copper and aluminium is seen. This adds weight to the theory that in ML3 the layers hold a strong orientation relationship between the copper and aluminium layers. There also seems to be a

presence of other unidentified spots. This could suggest other phases, a aluminium copper alloy was thought to be a possibility. The other phase present could prove to be the interface layer that was described previously. Compositional analysis was necessary to answer such questions.

### 5.3 Compositional Analysis

Initial TEM studies of this multilayer system, gave the first indication that the individual layers were not composed of alternating Cu and Al films, as was intended.

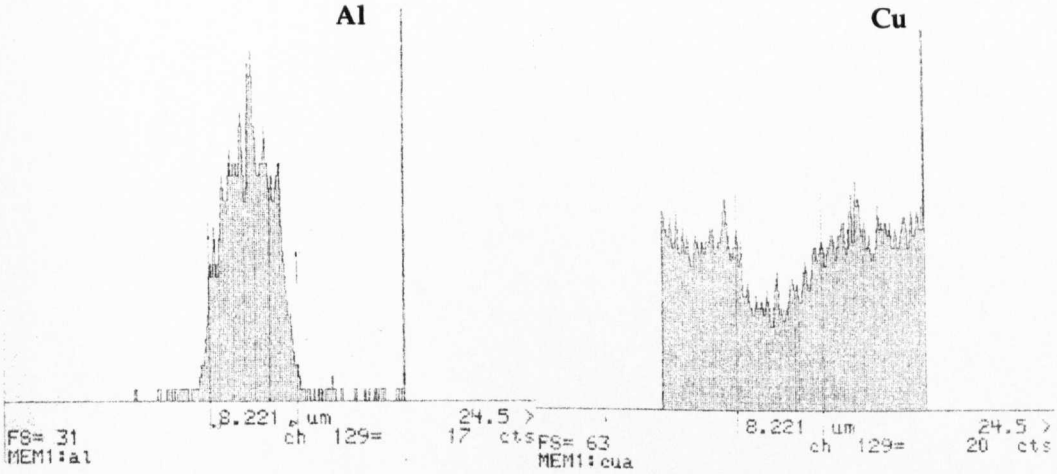


*Figure 5.12: Linescan through Cu/Al/Cu layers using TEM scanning attachment.*

Figure 5.12 shows a linescan carried out in the TEM on ML2 (nickel support grid). As expected, a strong Al peak is obtained as the beam travels through the Al layer. The Al detected seems to be constrained within the realms of its layer. However, this is not true for Cu, as it is seen throughout the linescan. This suggests that, what was originally deemed to be an aluminium layer in fact contains a significant quantity of copper.

The electron probe size using such a technique is ~20nm in diameter, and hence it is impossible to state that the tails seen in this scan are from some intermixing, or just simply as a consequence of the resolution of the machine.

It became important to establish the structure and composition of the copper that was detected in the aluminium layer. Quantitative data from the TEM in the Al layer in ML2, shown in Figure 5.13, suggests the it is in fact $CuAl_2$.

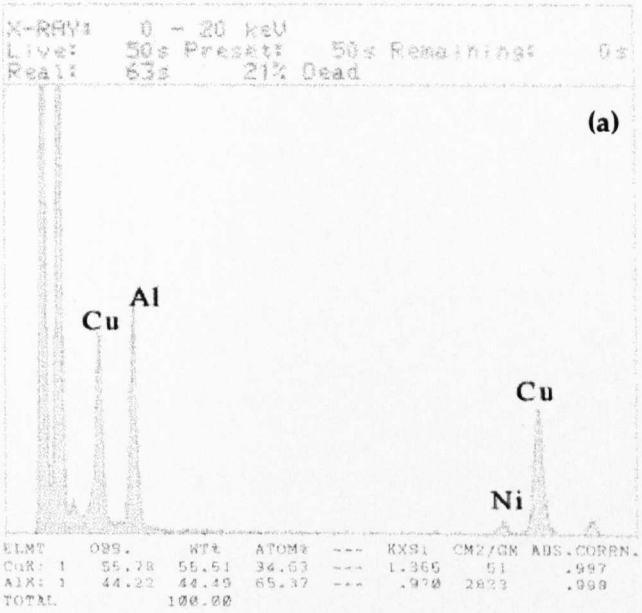


*Figure 5.13 (a): A typical X-ray spectrum from ML2 in the Al layer*

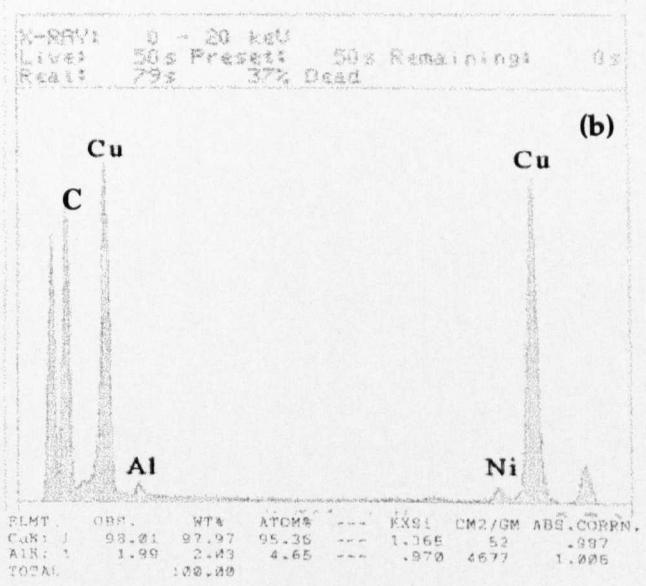


*Figure 5.13 (b): A typical X-ray spectrum in the Cu layer of ML2*

For ML3 (25nm Cu/7nm Al) diffraction patterns also indicated the presence of other phases, possibly more than one. Due to its small individual layer thickness and a possible presence of light elements such as oxygen, most of the work for this coating was carried out using the STEM due to its high resolution, windowless X-ray detector and PEELS facility.

### 5.3.1 STEM

The most striking feature of EDX spectra for ML3 (Figure 5.16) is the unexpected large amount of copper in the aluminium layer. Subsequently EDX linescans were carried out across this aluminium layer to establish whether the level of copper is constant across the coating.

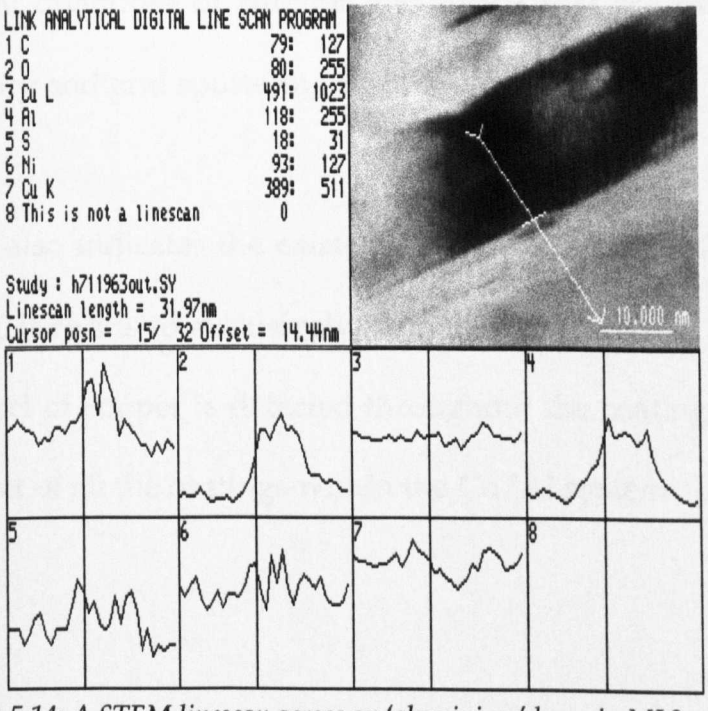


*Figure 5.14: A STEM linescan across an 'aluminium' layer in ML3.*

Figure 5.14 shows such a linescan. It clearly shows that there is a consistently high level of copper throughout the whole coating, the level does not seem to drop off at all in the aluminium layer (as was found in ML2). It became necessary to address the cause for this presence of copper, whether as consequence of processing methods, diffusion or both. The aluminium scan is also very interesting; as expected the intensity of the signal drops off in the copper layers, but peaks in the scan close to the interface, which could indicate a change in composition. Also there seems to be a level of oxygen associated with the aluminium that is too high to be simply dismissed as a surface effect. This layer could actually consist of a copper aluminium oxide and not aluminium, which would help to explain the astonishing hardness data for this coating (see Section 5.4). There are also nominal quantities of sulphur and nickel that are thought to arise from impurity and grid sputtering respectively.

Figure 5.15 also indicates the existence of an oxide in ML2; however for this coating, it seems to exclusively reside at the interface. Once again, a constant level of copper is detected throughout the coating, this seems to be an artefact of all the coatings within the Cu/Al system.

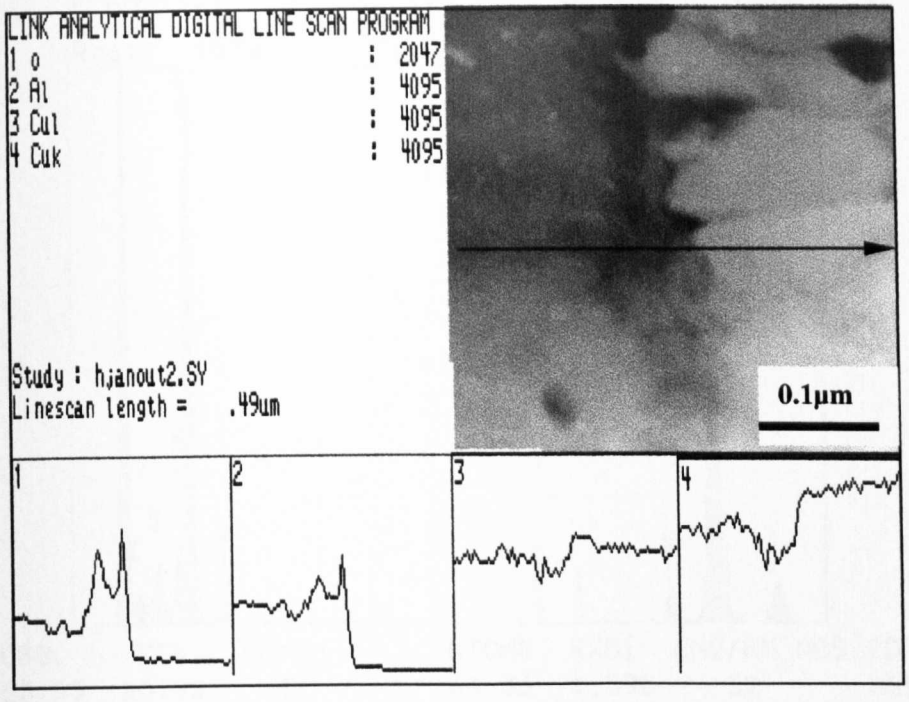


*Figure 5.15: A STEM linescan from an Al layer into a Cu layer in ML2*

It was noticed from several linescans, that the drop in the copper signal that was present in early TEM work was now not quite so significant. It was decided to carry out some more X-ray quantification in the aluminium layer. Typical results from this are illustrated in Figure 5.16 and 5.17. They show that now there is a much higher quantity of copper in the aluminium layer for both coatings, than was found previously. This gave an indication of time dependent interactions between the individual layers. Also unlike ML2, ML3 seems to have much more oxygen associated with its aluminium layer (Figure 5.16(a)).

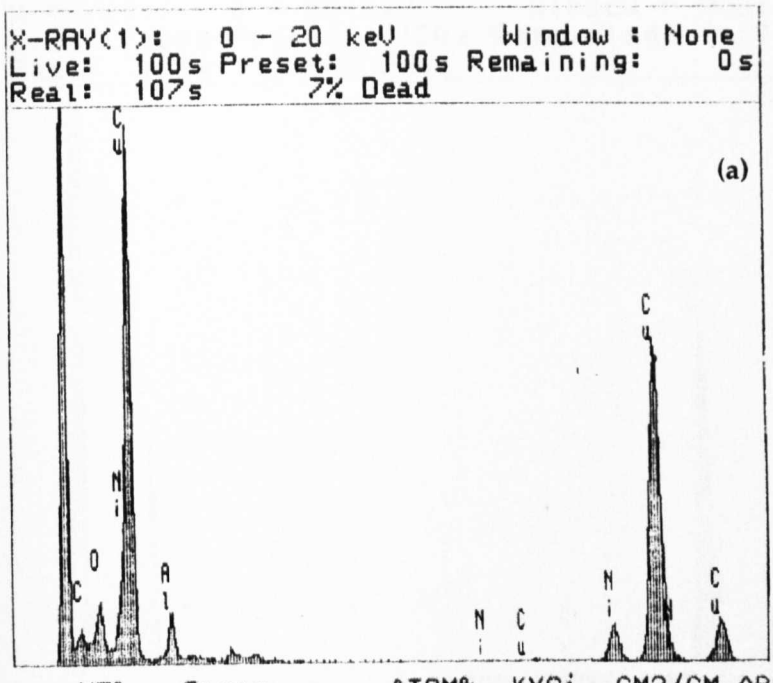


| ELMT | OBS. | WT% | Error | ATOM% | KXSi | CM2/GM | ABS.CORRN |
|---|---|---|---|---|---|---|---|
| CuK: 3 | 83.59 | 80.95 | .42 | 64.33 | 1.590 | 52 | .861 |
| AlK: 3 | 16.41 | 19.05 | .42 | 35.67 | 1.055 | 3934 | 1.032 |
| TOTAL | | 100.00 | | | | | |

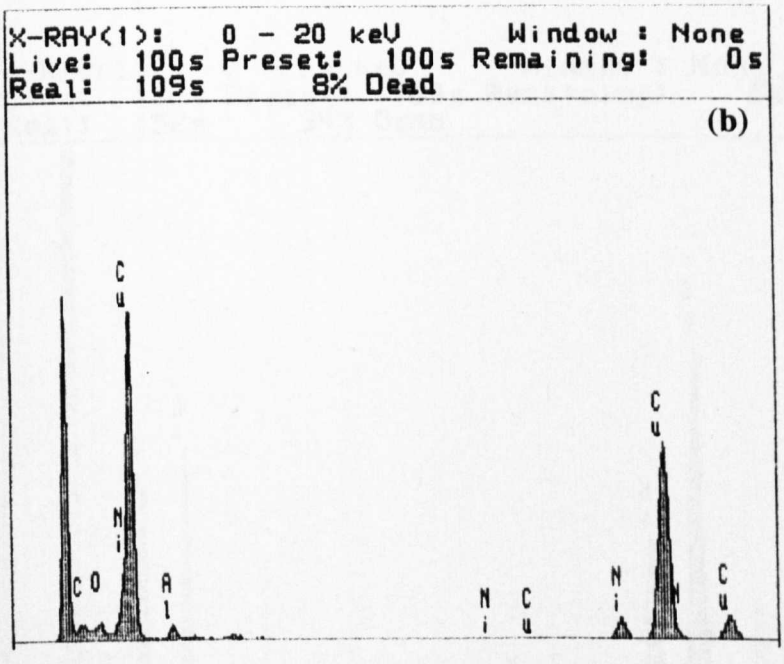


| ELMT | OBS. | WT% | Error | ATOM% | KXSi | CM2/GM | ABS.CORRN |
|---|---|---|---|---|---|---|---|
| CuK: 3 | 97.31 | 96.99 | .19 | 93.19 | 1.590 | 52 | .922 |
| AlK: 3 | 2.69 | 3.01 | .19 | 6.81 | 1.055 | 4635 | 1.035 |
| TOTAL | | 100.00 | | | | | |

*Figure 5.16: X-ray quantification in ML3 (a) Aluminium layer (b) Copper layer*

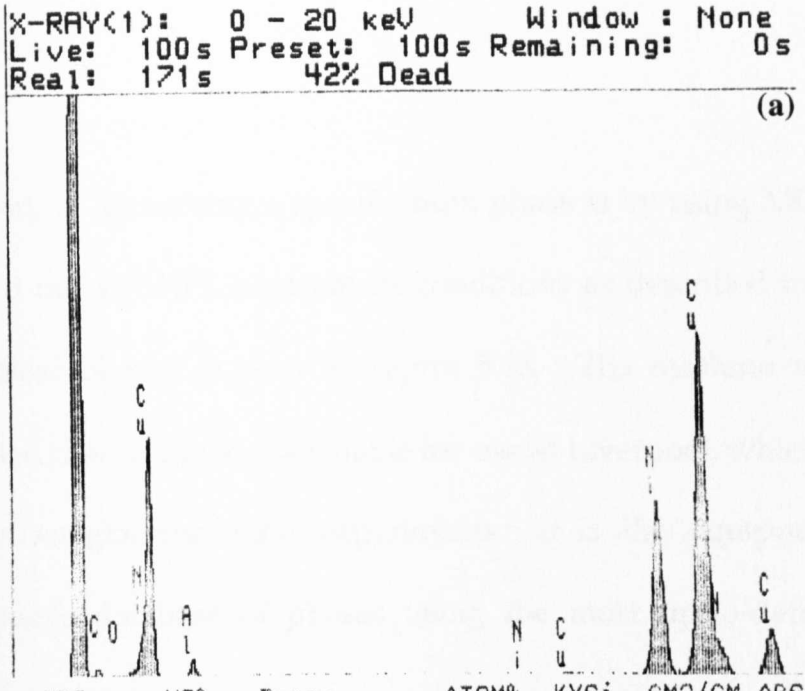


| ELMT | OBS. | WT% | Error | ATOM% | KXSi | CM2/GM | ABS.CORRN |
|---|---|---|---|---|---|---|---|
| CuK: 3 | 98.22 | 97.89 | .15 | 95.17 | 1.590 | 52 | .888 |
| AlK: 3 | 1.78 | 2.11 | .15 | 4.83 | 1.055 | 4674 | 1.054 |
| TOTAL | | 100.00 | | | | | |

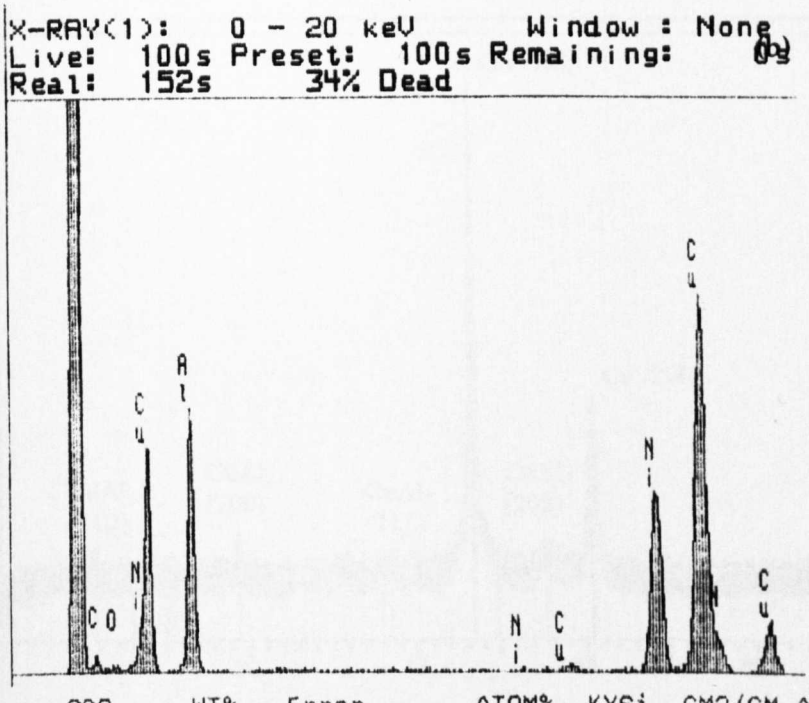


| ELMT | OBS. | WT% | Error | ATOM% | KXSi | CM2/GM | ABS.CORRN |
|---|---|---|---|---|---|---|---|
| CuK: 3 | 79.75 | 77.41 | .48 | 59.26 | 1.590 | 52 | .887 |
| AlK: 3 | 20.25 | 22.59 | .48 | 40.74 | 1.055 | 3779 | 1.020 |
| TOTAL | | 100.00 | | | | | |

*Figure 5.17: X-ray quantification in ML2 (a) Copper layer (b) Aluminium layer*

### 5.3.2 XRD

Another way of identifying a specific bulk phase is by using XRD, which was carried out at BNFL (instrument conditions as described in Chapter 3). A typical 2θ plot is seen in Figure 5.18. The machine was more sophisticated than the model available for use at Liverpool, which enabled it to carry out glancing angle experiments. It is also equipped with a comprehensive database of phases using the most up-to-date powder diffraction data.

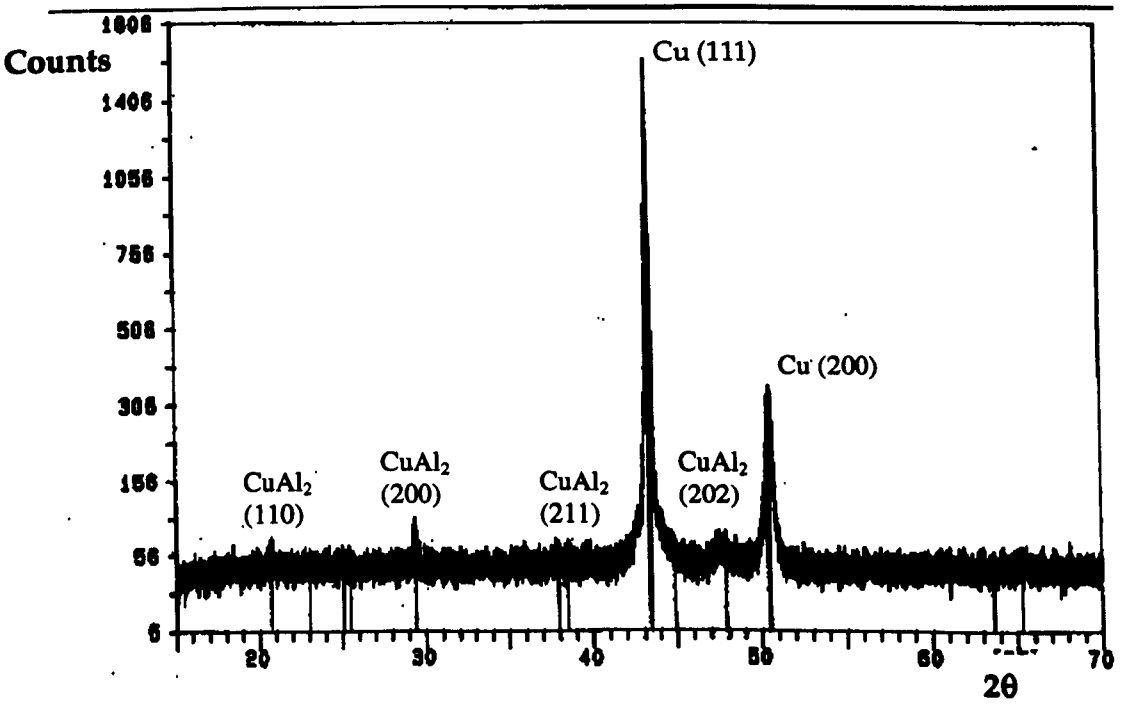


*Figure 5.18: XRD result on ML2 taken at BNFL*

The only Cu/Al coating available for XRD analysis at BNFL was ML2. The diffractometer trace surprisingly indicates that there is no pure aluminium present in the sample, (within the limits of detection). Also no oxides were detected, but the amount present at the interfaces could be beyond detection by this method. The strong intense peaks correspond to Cu reflections and, although low in intensity, the others seem to relate to $CuAl_2$, consistent with the quantitative EDX data in Figure 5.13 (a).

Figure 5.19 shows an XRD spectrum taken at Liverpool on sample ML3. Unfortunately this only confirms the presence of pure copper and no other phases. This was explained by the high texture and the number of interfaces that were being sampled.

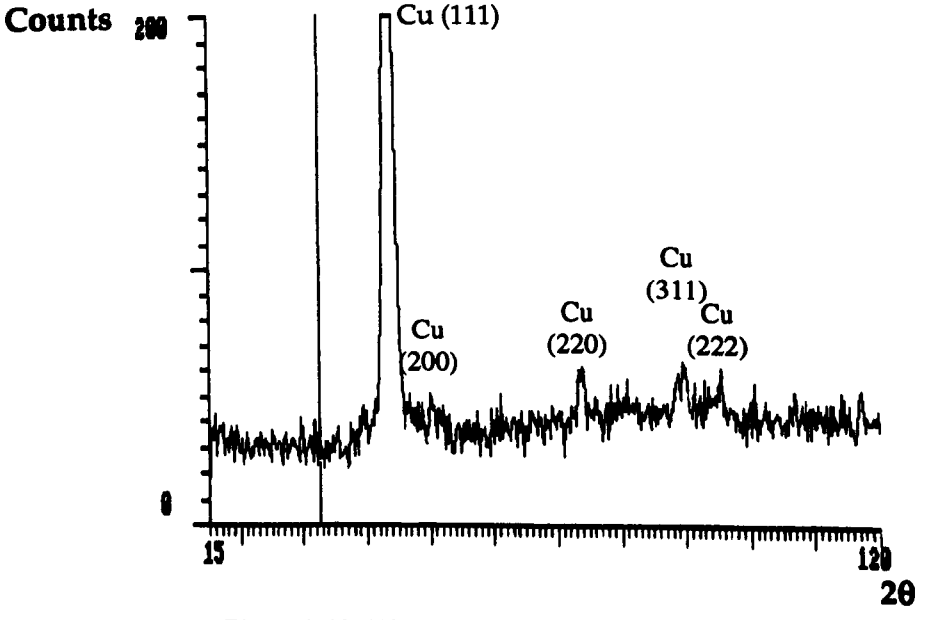


*Figure 5.19: XRD on ML3 carried out at Liverpool*

### 5.3.3 Diffraction work

Due to the small individual layer thickness of all the Cu/Al systems it was impossible to get a selected area pattern from just one of the layers. Convergent beam diffraction also proved difficult. Therefore selected area patterns were taken from many of the layers. Using the smallest SAD aperture at 20μm and considering the magnification of objective lens this translates to an area of ~1μm at the sample. For ML3 the number of layers analysed (of each material) together is ~30, even so it was thought that this technique could help characterise the coating.

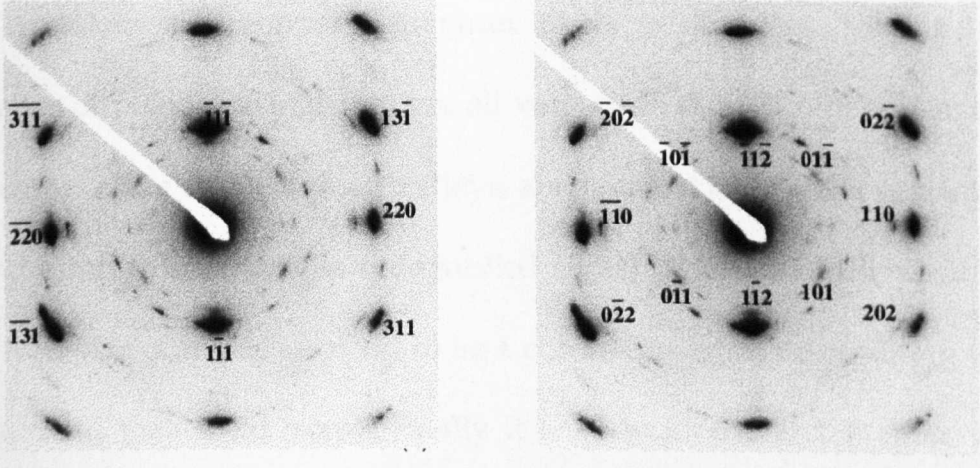


Figure 5.20 (a) and (b) show a diffraction pattern on ML3. There is a strong texture seen in the pattern even though, as explained above, many layers are contributing to the data. The copper spots are the strongest of all, and were easily indexed with the beam parallel to the $[\bar{1}\bar{1}2]$ direction (Figure 5.20(a)). The other spots however proved much more difficult to

identify. From previous X-ray analysis it was known that $CuAl_2$, an oxide and other copper aluminium alloys all could be present. Initially the next strongest points Fig 5.20(b) were indexed as aluminium. However, this did not account for the spots with spacings below that of Cu $(\bar{1}1\bar{1})$ (d~1.9Å). Other orientations of aluminium were also discounted. The spots seemed to be in a pattern more reminiscent of a hexagonal structure. Aluminium oxides were also discounted as possibilities, leaving alloys of copper and aluminium or other oxides.

The problem with copper-aluminium alloys is that they have a large number of plane spacings that are all very close to each other. Table 5.4 shows several examples of such alloys, and some of their plane spacings in comparison to some of the unidentified spots. Because of this difficulty the interplanar angles also had to be a consideration in determining what compound they were from. Finally it was decided that the spots were most likely to be originating from the rhombohedral structure of $CuAlO_2$. Figure 5.21 shows the calculated orientation of $CuAlO_2$ along a $[\bar{1}1\,1]$ zone axis using Electron Microscopy Software (EMS) [81], with parameters as reported by Jacob *et. al.* [76].

| A selection of some of the unidentified plane spacings d (Å) | Al d(Å) | $Al_2Cu_3$ d(Å) | $CuAl_2$ d(Å) | $CuAlO_2$ d(Å) | CuAl d(Å) | $Al_4Cu_9$ d(Å) | $AlCu_4$ d(Å) |
|---|---|---|---|---|---|---|---|
| **4.35** | 2.34 | 3.58 | 4.30 | | 5.66 | 3.89 | 2.80 |
| **3.64** | 2.02 | 2.93 | 3.04 | | 4.95 | 3.56 | 2.56 |
| | 1.43 | 2.07 | 2.37 | | 3.79 | 2.90 | 2.09 |
| | 1.21 | 1.79 | 2.15 | | 3.53 | 2.51 | 1.98 |
| **2.44** | 1.17 | 1.69 | 2.12 | 2.45 | 3.47 | 2.32 | 1.89 |
| **2.38** | 1.01 | 1.46 | 1.92 | 2.37 | 2.98 | 2.11 | 1.807 |
| **1.46** | | 1.36 | 1.90 | 1.43 | 2.88 | 2.05 | 1.673 |
| **1.25** | | 1.31 | 1.61 | 1.22 | 2.83 | 1.99 | 1.475 |
| | | 1.27 | 1.52 | | 2.55 | 1.95 | 1.40 |
| | | | | | 2.24 | 1.90 | 1.37 |
| | | | | | 2.06 | 1.85 | 1.34 |
| | | | | | 2.05 | 1.78 | 1.28 |
| | | | | | 2.03 | 1.70 | 1.25 |
| | | | | | 2.01 | 1.67 | |

**Table 5.4: A selection of Cu/Al/O phases with selected d spacings to compare to some unidentified plane spacings, main spacings are in bold (taken from standard powder diffraction data)**

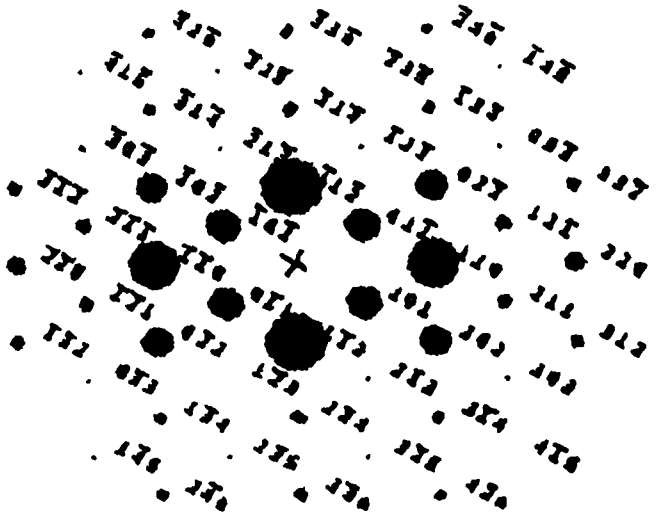

***Figure 5.21: An EMS calculation of the $CuAlO_2$ phase with the beam along the $[\bar{1}11]$ type zone axis [81]***

This pattern highlighted a fundamental oversight by assuming that ML2 and ML3 would have the same compositions in the aluminium layers

### 5.3.4 PEELS

To further establish whether the aluminium layer consists of pure copper and aluminium, or an alloy phase the PEELS fine structure was examined. This proved to be a very fruitful approach in the analysis of titanium diboride. Unfortunately, the Cu-M and Al-L edges are extremely close and hence it would be impossible to distinguish between them.

It was decided to look at the Cu L-edge at 931 eV for ML2. Figure 5.22(a) and (b) show typical spectra taken within the copper layer and aluminium layer respectively. Clear differences are seen between them (labelled 1-4)

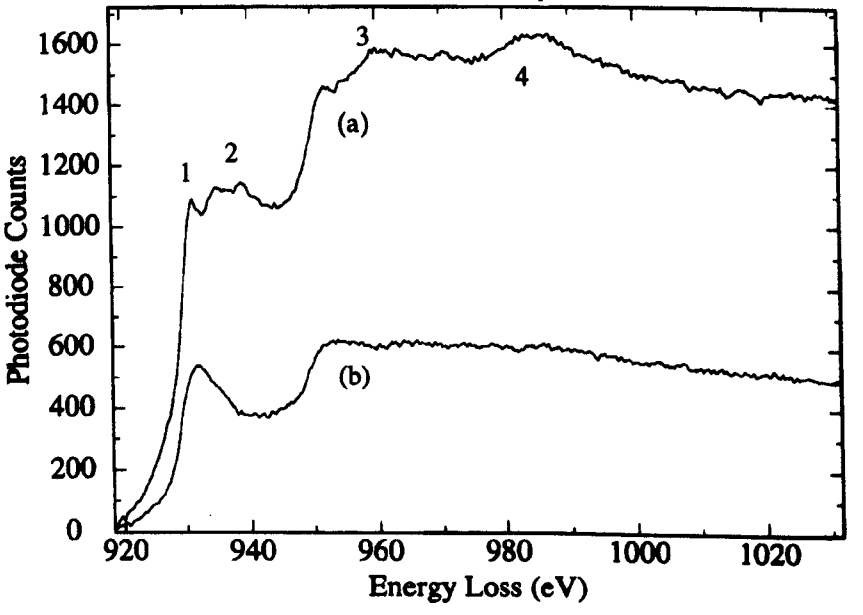


*Figure 5.22: PEELS spectra from ML2 (a) in Cu layer (b) in Al layer*

This suggests that the Cu in the Al layer is not of the same form in the Cu layer. The spectra obtained from the pure Cu layers are of the structure one would expect from pure Cu. However, the copper spectra from the Al layer are consistent with spectra in the literature for $CuAl_2$ [82].

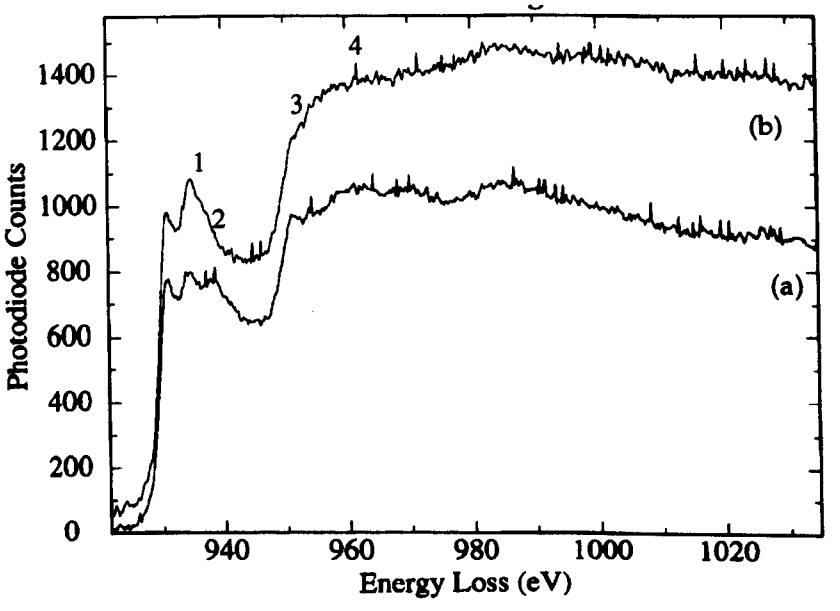


*Figure 5.23 Comparison of Cu-L edges in ML3 for the pure copper layer (a) and 'aluminium' layer (b)*

Figure 5.23 shows the PEELS data from ML3. This also shows differences (labelled 1-4) between the Cu L-edge in the Cu layer (a) and the Al layer (b). However the fingerprint seen in (b) does not relate to any edges previously reported in the literature.

Even though there is a large amount of oxygen (Figure 5.24) associated with the EELS spectra (consistent with previous X-ray analysis) this Cu L-edge is not reminiscent of those reported for copper oxides [50, 82], which have strong white lines.

The Al layer in ML3 has proven very difficult to characterise. Electron diffraction has shown that there is a presence of $CuAlO_2$ and possibly $CuAl_2$. It is not inconceivable that there are also small quantities of pure copper and/or aluminium in there too. This makes the Cu L-edge in the PEELS spectrum difficult to interpret but it could possibly be related to $CuAlO_2$. This is discussed further in Chapter 6.

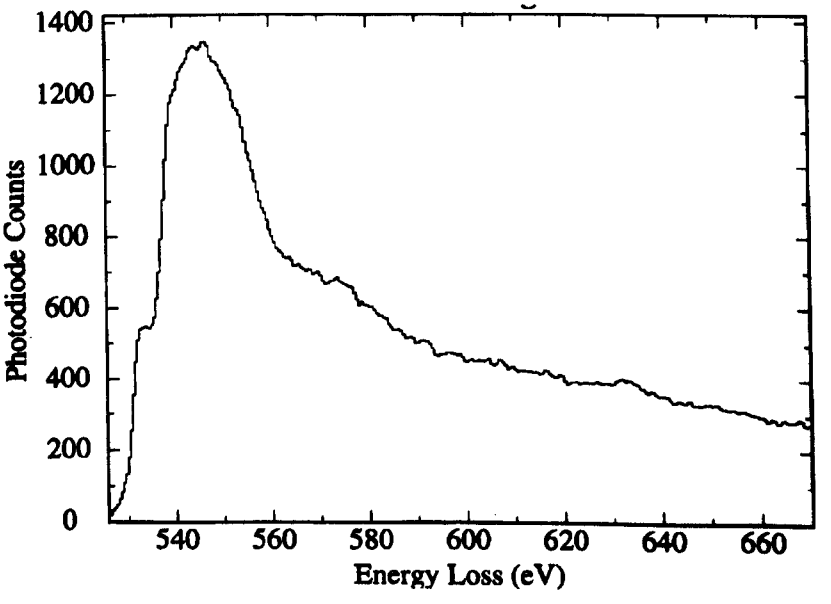


*Figure 5.24: Oxygen K-Edge from the aluminium layer in ML3*

## 5.4 Hardness Tests

Originally it was not an objective of this work to measure mechanical properties on any of the multilayer samples. This work was to be carried out by the manufacturers of the coatings, to be used as a comparison to microstructural and compositional information produced during this project. Figure 5.25 shows an example of hardness data measured by BNFL on the same batches of coatings. It shows Knoop Hardness versus

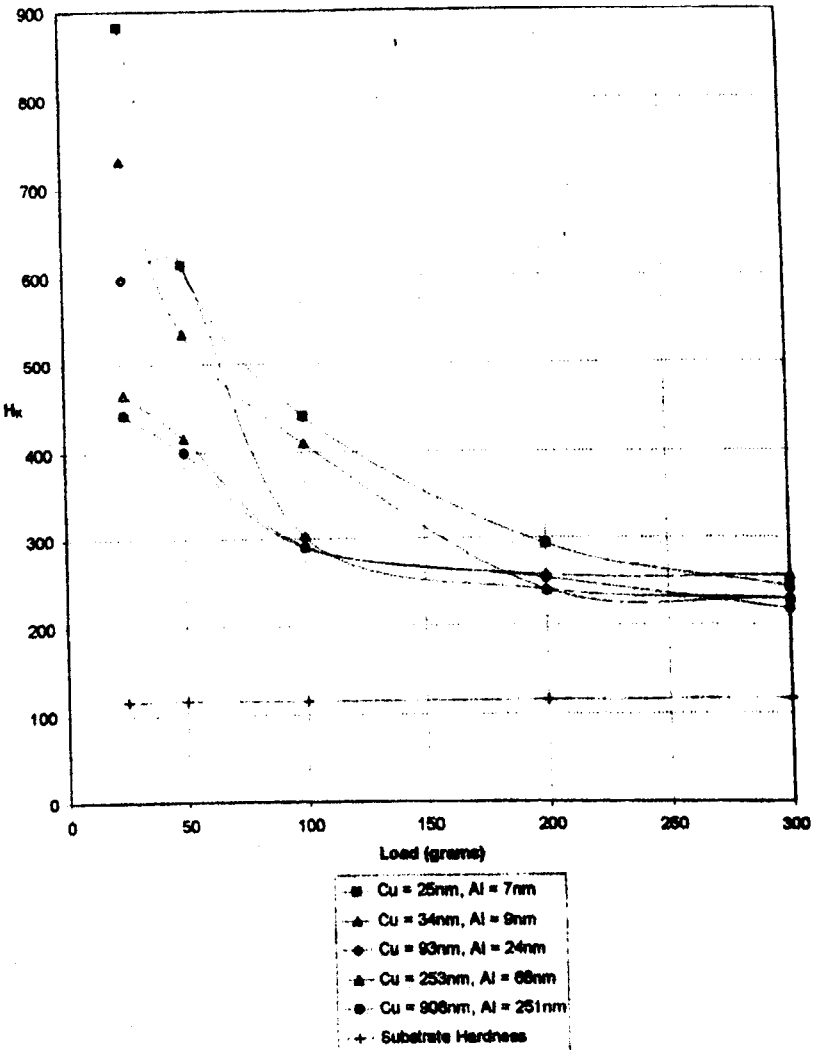


*Figure 5.25: Hardness vs. Load used for several Cu/Al multilayer sets*

the load on the indenter. All of the multilayer systems show an improvement over the hardness of the substrate, which must be the first goal of any coating.

So much information is contained in this figure that it was deemed necessary to take the data provided by BNFL and present it differently (all error bars relate to a 10% variation in either direction). Figure 5.26 shows a plot of Knoop hardness versus individual layer thickness from the smallest load of 25g (the line connecting the dots in all of the following charts is for illustration purposes only).

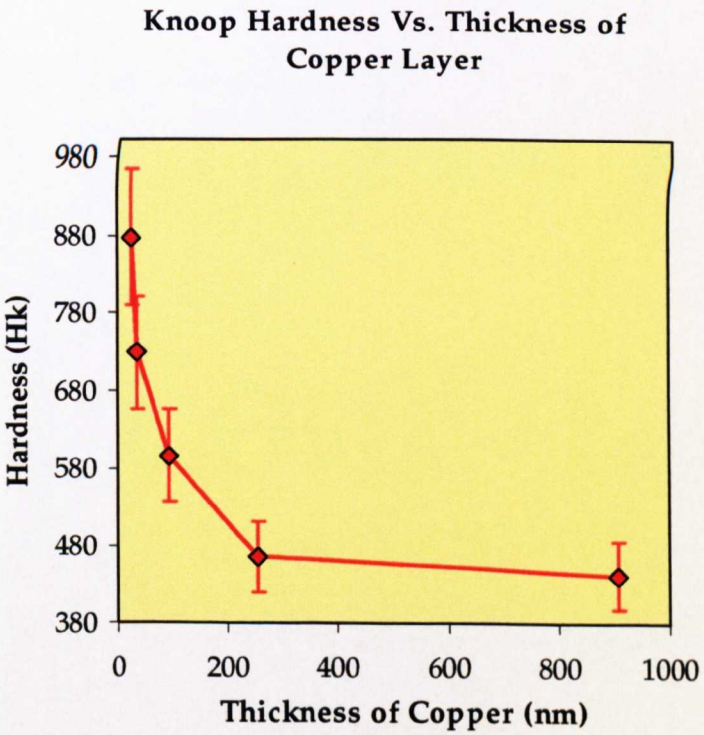


*Figure 5.26: Knoop Hardness vs. Thickness of Copper in the Multilayer*

A distinct trend of decreasing individual layer thickness producing increasing hardness is seen. The best result from the thinnest individual system at 878 Hk is phenomenal, being as hard as a tool steel [79] and more than 100% harder than a layer of monolithic sputtered copper. There was some doubt over the validity of these measurements and over the interpretation of exactly what the results were measuring. For example, in the thickest layers (ML2) there are hardly any interfaces sampled when using a load of 25g, whereas many more interfaces are sampled in the ML3 sample. Since the interface is widely considered to be central to improvements in such coatings, this was seen as a fundamental flaw in analysing such data.

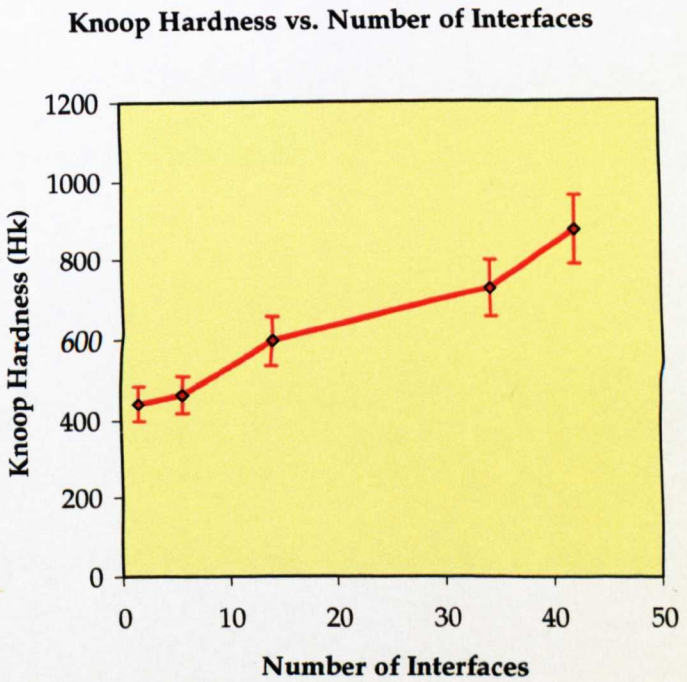


*Figure 5.27: Knoop Hardness vs. Number of interfaces sampled for 50g load.*

Figure 5.27 seems to confirm this deduction since it was decided to plot Knoop hardness versus the number of interfaces sampled for a 50g load on all of the multilayers. Hence the least number of interfaces sampled is 2 carried out on ML2, and the most is 41 in ML3.

A trend of increasing hardness with the more interfaces sampled is apparent. Another problem with the BNFL data in Figure 5.25 was that with an increasing load there is more chance of sampling the substrate. This is thought to be the reason for the drop in hardness as the load is increased. However on further study of the data (by calculating the penetration depth of the diamond) only the two lightest weights have not sampled the substrate, and only the 50g load had sampled enough interfaces to be credible. Due to all of the above reasons it was decided to carry out more hardness tests.

One way of ensuring the substrate has no influence would be to test the coatings in cross-section. Also by this method a comparative number of interfaces would be sampled and although not perfect; possibly more accurate data (providing better comparisons between each other) would be obtained.

Figure 5.28 shows indents in cross-section in the coatings, unfortunately at the time only a Vickers microhardness instrument was available for use. These indents however, do not satisfy the criteria in cross-sectional hardness tests, as described in Section 2.3. It became necessary to carry out this investigation on thicker coatings.

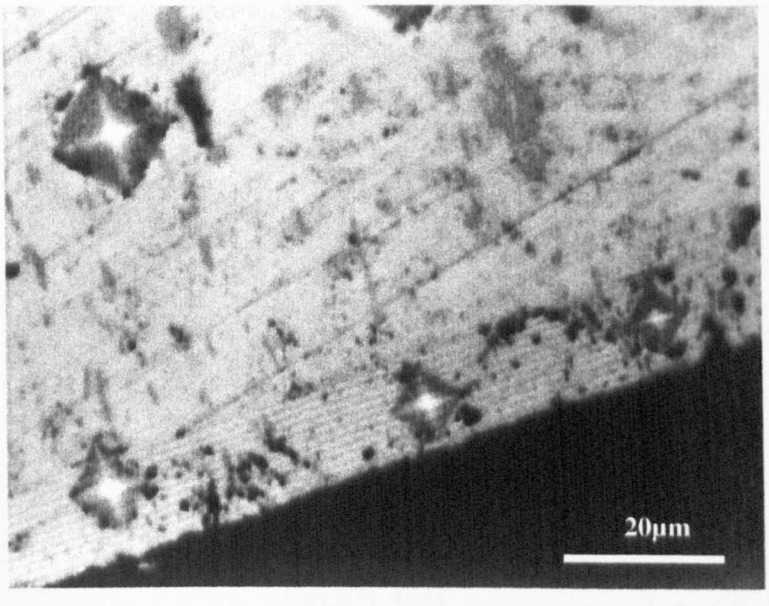


*Figure 5.28: A cross-section of a multilayer coating after hardness testing*

The only samples available that could fulfil the criteria had thick individual layers as well as a thicker overall total coating thickness. Nonetheless a comparison between cross-sectional and plan view data would be possible. Figure 5.29 shows this data.

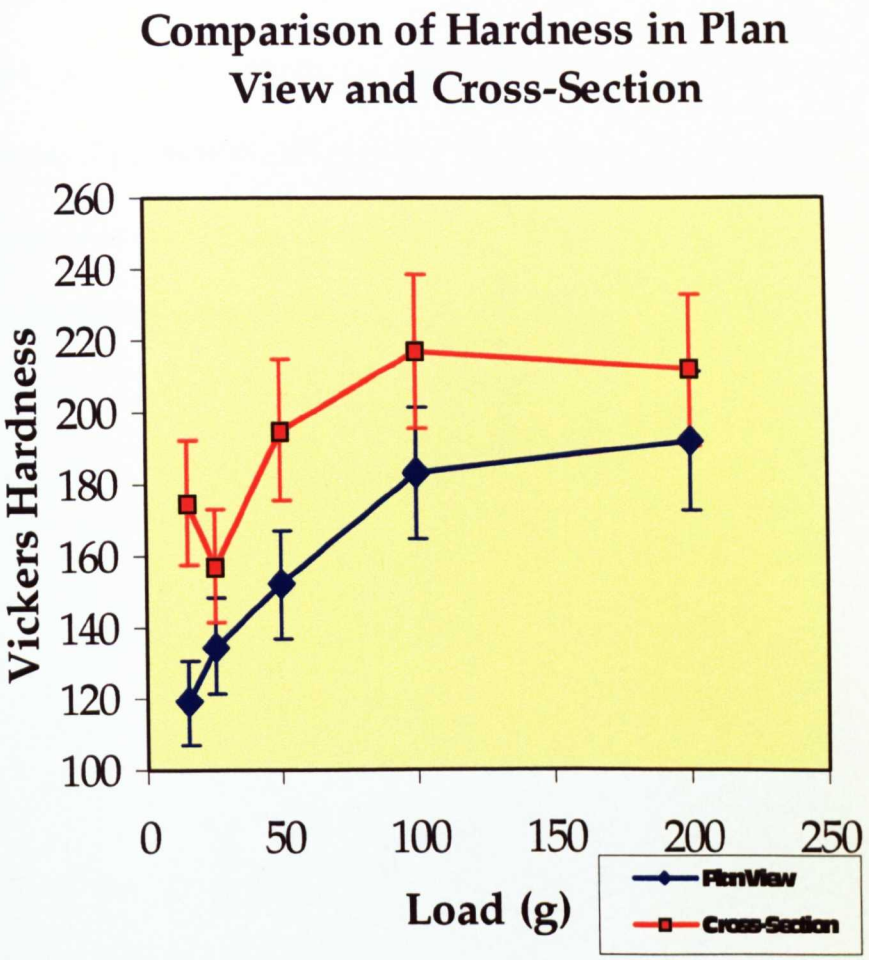


*Figure 5.29: Comparison of hardness test in cross-section and plan view (Al substrate)*

The cross-sectional data consistently produces improved hardness over the plan view. However the biggest surprise was that the substrate was harder than either. This could be as a consequence of the very thick PVD coating having too much porosity.

Also to be consistent with PVD theories and the expected resulting properties (described in Chapter 3), one would also expect the plan view sample to perform better, presuming these coatings do have a columnar structure. This would either indicate that the grains were not columnar or that interfaces are indeed contributing to the increase in hardness data, the later of which is the most likely.

## 5.5 Summary of Cu/Al Results

The Cu/Al multilayers exhibited very distinct and uniform layers with individual layer thicknesses close to those aimed for. The discrepancy was much less than for the $TiB_2$/Al coatings.

The most important discovery on studying these Cu/Al coatings was the different compositions that ML2 and ML3 exhibited (ML1 TEM sample was not considered good to analyse). The coatings are clearly not the same and the structures are much more complex than was anticipated. This, of course, is essential information for those comparing property data on such coatings, expecting the only variable to be individual layer thickness.

For these reasons, in summarising the results each coating will be considered in turn.

### 5.5.1 ML2

ML2 was the easier of the Cu/Al multilayers to analyse due to its relatively large individual layer thickness. The Cu rich layers are columnar in contrast to the $CuAl_2$ rich layers, which are mainly equiaxed.

A zone was found at the interfaces between the Cu-rich and $CuAl_2$ rich layers. This is an oxide, most probably an aluminium oxide. A schematic of the multilayer when first analysed is seen in Figure 5.30 below.

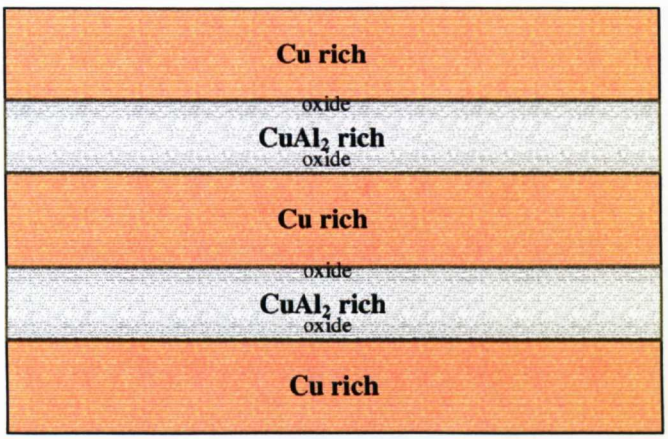


*Figure 5.30: A schematic of ML2 when first analysed.*

Another surprise with the coatings was the composition changing with time. Reasons for such changes and the effects resulting from them are discussed in Chapter 6.

### 5.5.2 ML3

ML3 was much more difficult to characterise due to it's thin individual layers. Columnar grains were not easily distinguished, however evidence of column features running throughout the whole coating were seen.

Rather than oxide concentrated solely at the interfaces, much more was detected throughout the 'Al' layer. It became possible to propose that this oxide is $CuAlO_2$, using electron diffraction. This then enabled a suggestion for a previously unreported, Cu L-edge fingerprint for this phase. As with ML2, the ML3 sample also changed structure with time. This effect was even more dramatic for this coating and is discussed in detail in Chapter 6.

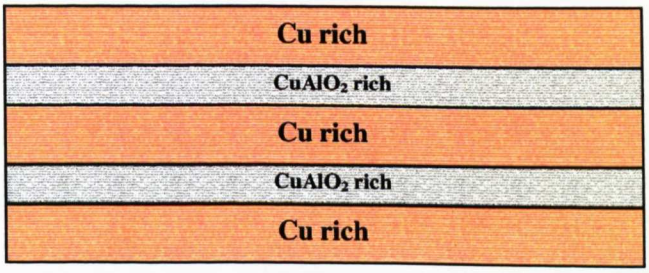


*Figure 5.31: A Schematic of ML3 as first analysed.*

This coating is very difficult to characterise. Figure 5.31 gives a proposal to the form of the coating when first analysed. The aluminium region contains $CuAlO_2$ and possibly $CuAl_2$. The presence of small amounts of copper and aluminium, either in a pure form or alloyed, can be ruled out.

However, the most important point, is that the coating examined bore little resemblance to the coating that was intended to be grown, and is different to ML2, casting a shadow of doubt over hardness correlations.

Hardness data from BNFL suggests that this ML3 coating performs on a comparable level to steel, with a vast improvement over ML2. With the differences in structure that have been confirmed, this now must be viewed with caution.

Extra hardness tests were carried out due to uncertainty of the incredible values stated for ML3. These correlate the hardness to the number of interfaces sampled. Also cross-sectional versus plan view data was taken, producing very interesting results that are discussed in Chapter 6.5.

§

# Chapter 6

## *Discussion*

Chapter 6 has been split into five sections, to discuss the main aspects of the research in this project. It starts with consideration of the *uniformity* seen in the multilayer coatings. One of the primary goals of the research was to establish how distinct and uniform the films were. Secondly the *microstructure* formed is debated, as it has already been shown in chapter 2, this is an essential part of a coating if the specific properties required are to be achieved. Section three consists of a major part of the research; studies into the *composition* of the individual layers and addresses one of the most important results, that of ML2 and ML3 unexpectedly differing. Such a dramatic result is essential to those who compare mechanical property data of such coatings. EELS studies on these coatings are included and a suggestion is made for a new Cu-L fingerprint for a copper alloy.

*EELS studies on* $TiB_2$ are addressed in a separate section as the results show important orientation effects that have not previously been thought relevant in this compound. The chapter ends with *hardness* studies.

§

## 6.1 Uniformity

The uniformity of the layers is paramount to the performance of the coatings. The type of material that is used and the processing parameters can all have an effect. Since the two different systems that have been studied were processed differently, we can get an insight into how much of an effect the preparation method has for these coatings.

Considering the $TiB_2$/Al layers first, the most important conclusion is that a multilayer coating has been achieved, rather than a multiphase coating. Distinct layers were clearly seen both in the TEM and Auger studies (Figures 4.1, 4.3). The TEM studies show a reasonable degree of uniformity; however the consequences of ion-beam thinning must be considered. The hard $TiB_2$ ion-mills at a significantly slower rate then the relatively soft aluminium. It is thought that a step-like structure is achieved as shown in the schematic, Figure 6.1.

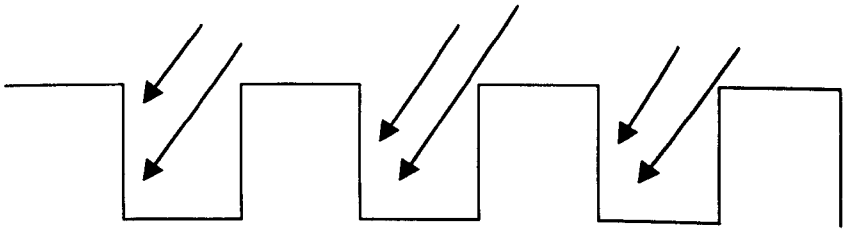

*Figure 6.1: Schematic of preferential interface milling*

It is likely that when the step created is distinct enough, preferential milling can occur at the interface. This effect is thought to create an exaggerated, uneven interface. This is backed up by Figure 6.2 which shows a thicker part of a $TiB_2$/Al multilayer coating which seems to have better uniformity.

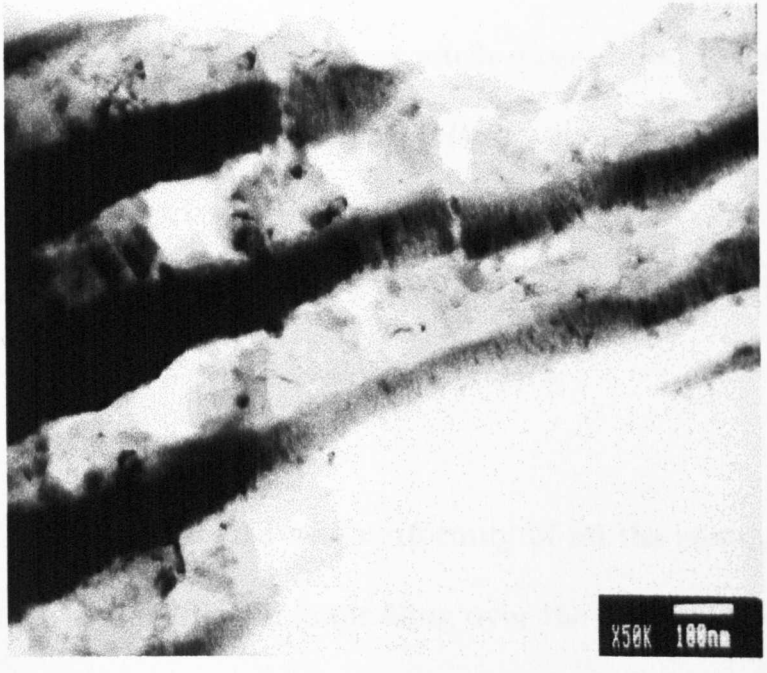


*Figure 6.2: TEM image of $TiB_2$ /Al Coating showing thicker region with more uniform interface*

For the thinner $TiB_2$/Al multilayer coating (~25nm $TiB_2$/25nm Al) ion milling cannot explain such an uneven and irregular structure (Figure 4.4). The layers, in places, are not intact and are of varying thickness. There are a number of possibilities for this phenomenon, the first of which is the processing technique. Between the sputtering of each individual layer the power supply to the targets had to be manually switched over.

On a coating with numerous thin individual layers (~100) the manufacture becomes time consuming and monotonous. It is not surprising that some layers have been sputtered out of sequence. This kind of processing is impractical and also carries a greater chance of depositing impurities at the interfaces.

The comparable Cu/Al coating shows much more uniform layers with a consistent structure. These layers are also surprisingly close in actual thickness to that calculated from the deposition rate. The benefit of continual substrate rotation is clearly demonstrated and also lessens the chance of impurity incorporation at the interfaces.

The largest Cu/Al set has the best uniformity of all the coatings studied. The shorter and more efficient ion milling over the $TiB_2$/Al set could also have contributed to this, as well as the processing differences described above. The more focussed guns and lower incidence angles in the PIPS has resulted in much wider areas of electron transparent regions that only took 20 minutes to achieve. The $TiB_2$/Al set would have benefited from this preparation method especially due to the differential milling rates of the two individual layers. Such multilayers were subjected to over 4 hours milling in a standard dual ion mill.

Errors in the size of the individual layers are more noticeable in thinner sets. Figure 5.4 shows ML3 (~25nm Cu/7nmAl), the individual layers get progressively thicker from the substrate upwards. This is as a consequence of the magnetrons not sputtering at their optimum rate as deposition commences.

The effect of thinner layers closer to the substrate could however, prove beneficial. Ruff *et. al.* [34] have reported better properties in their Ni/Cu system when the individual thickness of each layer is ~3nm. However, if any of these coatings are to prove attractive to industry then the manufacturers must produce a final product close to the original design. Consequently it has to be concluded that this is an unwanted effect.

§

## 6.2 Microstructure

One of the first considerations of the microstructures was the grain sizes and characterisation of them. In the $TiB_2$/Al multilayer coating, it proved quite easy to establish such information.

The $TiB_2$ layer has a classic zone 1 microstructure identified by the combination of columns with tapered ends as shown in Figure 4.5. Consistent with the Thornton model [18], the high melting temperature of $TiB_2$ makes such a structure difficult to overcome. Also, there was no bias applied to the substrate in this process. It has been reported [8] that if a large enough bias is applied, the momentum exchange causes depositing atoms to fill voided boundaries. This avoids zone 1 structures and zone T type structures being formed.

Conversely aluminium has a relatively low melting point and it therefore comes as no surprise that the tapered columns are no longer seen. For the Thornton model to fit (using parameters as described in Appendix 1), the substrate temperature would be between room temperature and 194°C at deposition, for a zone 2 structure to form in Al. This is also consistent with the zone 1 formation in $TiB_2$. However with the deposition of multilayer coatings it is difficult to be sure of the localised temperature at any one time, or the temperature of the substrate, which itself is constantly changing. Also, such calculations can only be used as a guide due to the lack of consideration of the inert gas pressure.

If the same considerations are applied to the ML2 coating, a higher substrate temperature is predicted. For a zone 2 copper layer to form, a temperature between 134-406°C must have been reached. It has been established that the aluminium layer actually consists of mainly $CuAl_2$ with a zone 3 structure. This would increase the lowest substrate temperature prediction from ~134°C to ~160°C. Again, these predictions are only rough estimates but perhaps indicate that the Cu/Al coatings were deposited at higher temperatures than the $TiB_2$/Al coating.

In ML3 it is much harder to establish grain sizes, forms and zone types. Such problems in identifying the boundaries were also reported by Cawley *et. al.*, [47]. The work also showed evidence of columns that are carried throughout many layers. Such columns seen in the ML3 Cu/Al multilayer are not apparent in the lower third of the film. This is in agreement with Larsson *et. al.*, [40] who also reported their absence in the lower region of the film. Columns throughout multilayers were also seen by Setoyma *et. al.*,[31] but only in those with very thin individual layers. Other column effects have been reported by De Veirman *et. al.* [83] who showed the effect of an increase in temperature on the width of the growing columns. They presented work on Co/Cu multilayers deposited at 200°C. The width of such columns were more than double the width of a similar coating deposited at 20°C.

In ML3 the width of such columns gradually increases, possibly indicating an increasing deposition temperature as the film grows. The lower region of this multilayer does not have any such columns; this is also possibly a temperature effect. Perhaps the substrate could be acting as a heat sink for the lower part of the film. Effects of columns growing through the thinner layers in the Cu/Al system, were not seen in the $TiB_2$ system. Of course the thin set of layers was difficult to image due to the magnetic nature of the substrate. The most likely explanation for the lack of such columns comes from the difference in the processing between the two systems. The targets of each material for the $TiB_2$/Al multilayer were powered down whilst the other was coating. Fig 5.4 for the Cu/Al system highlighted the fact that such targets can take time to establish optimum deposition and hence such powering down for every layer may have saved this coating from transient increases in temperature. This would influence the adatom mobility and therefore the formation of such columns.

§

## 6.3 Compositional Studies

Compositional studies of the multilayer coatings had contrasting success. The $TiB_2$/Al coatings were comparatively straightforward to study and easily characterised. This is partly due to finding results that were expected. However the same cannot be said for the Cu/Al multilayers, not only did they exhibit unexpected results with respect to composition, but also this project has highlighted inconsistencies between the ML2 and ML3 coatings themselves. As a result several different techniques have been used to try to characterise the exact compositions of the coatings. It has only been through a combination of these methods that conclusions have been made.

### 6.3.1. Auger Spectroscopy

The first technique used with the $TiB_2$/Al multilayers was Auger spectroscopy. This is purely a surface analytical technique and hence to get information from individual layers, in a plan view sample, a hole was drilled into the surface through several layers using an ion gun. Auger mapping of these gave the first indication of the composition of the layers. It became clear that the layers alternated between aluminium rich and titanium/boron rich areas. The oxygen levels seemed to rise in the aluminium layers, which is unsurprising given the high affinity of aluminium for oxygen. However it is also possible for oxygen to be

incorporated in coatings made by sputtering methods, as reported by Makous *et. al.*, [84].

The problem with this surface technique is that it is inadequate to establish whether the oxygen is in the form of a surface oxide or whether it is incorporated within the layer. However it does show that there are distinct layers of alternating composition.

### 6.3.2. X-ray Analysis

EDX analysis was carried out on a conventional TEM and a dedicated STEM. On analysis of spectra from the Cu/Al set of coatings, the first difference from the $TiB_2$/Al set, was the lack of argon present. This is rather surprising as the unbalanced processing method used for the Cu/Al should be more likely to lead to the incorporation of argon within the layers due to extra bombardment, as described in Section 2.2.2 [8]. The argon found in the $TiB_2$/Al coatings has therefore been attributed to the different ion beam thinning techniques used, and the differences in sensitivity to sputtering of the materials.

#### 6.3.2.1 ML2 Cu/Al multilayers (908nm Cu/253nm Al)

The Cu/Al ML2 set of coatings produced unexpected compositional results. The Cu layer analysis seemed quite reasonable, with around 95 at% Cu and 5 at% Al. However, spectra from the aluminium layer,

proved conclusively that it is not simple homogeneous film of pure aluminium. Possibilities for this unexpected incorporation of Cu could be due to diffusion between the layers themselves, or could have occurred because of difficulties at the processing stage. Hackney *et. al.*, [74] reported interactions between Cu/Al interfaces with the formation of theta phase ($CuAl_2$) during interdiffusion studies.

Initial TEM studies (Figure 5.13) in the centre of the layer gave X-ray quantification, that on comparison with the Cu/Al phase diagram (Figure 2.29), suggested the formation of $CuAl_2$. The presence of this phase was later confirmed by XRD analysis carried out at BNFL (Figure 5.18).

The use of a phase diagram for sputtered PVD processes, however, should really only be considered as a guideline. The effect of such processes and the local heating that occurs in the immediate area of a deposited atom is not well known. Other researchers have reported the formation of phases with a structure that does not lie within the convention of the standard phase diagram [31]. When studying AlN/TiN multilayer coatings, they found that the structure of the AlN layer adopted a NaCl form which is usually only achieved at very high pressures. What is most interesting about this work, is that they also found that the unexpected structure of AlN was not adopted for the larger period structures, where the expected wurtzite structure is seen.

On studying the TEM linescans in ML2, it is shown that as the beam traverses from the centre of the Al layer towards the interface, the ratio of Cu to Al progressively levelled out, until the beam was totally in the Cu layer (Figure 5.12). However, this is enivitable, since with a ~20nm probe, the signal must be created from both layers simultaneously in some areas.

It became apparent from this, and because of the thinner ML3 coating that STEM work was to be necessary. When available, several weeks' later, more compositional analysis was carried out to confirm the previous TEM studies.

Very unexpected results were found. The composition now was completely different and ranged between 60-66 at% Cu. For the first time, and in total contrast to the $TiB_2$/Al coatings, interactions between the layers were seen to be of vital importance.

In ML2, if diffusion *between* the layers was the underlying factor, then greater amounts of copper close to the interface would possibly be expected, as was found in the TEM results. However the Al does not seem to have diffused into the copper layer (Figure 5.15). Linescans prove that the aluminium was still concentrated within its layer and STEM

quantification in the copper layer was consistent with previous TEM results and remained unchanged at 95at% Cu.

This shows that if diffusion is occurring in this coating it is only within the aluminium layer itself. This poses two fundamental questions, firstly what is the driving force for such an interaction? Secondly, why do such interactions not occur between the individual layer themselves? These questions are addressed in Section 6.3.4, interactions and interfaces.

If there are *intralayer* interactions rather than *interlayer* interactions then Cu in the aluminium layer must be present as a result of a processing error. The processing conditions used for these coatings are described as similar to Arnell *et. al.* [9] (Figure 2.5). Unlike Ding *et. al.* [16] there were no shutters used in the processing system. This could be the major contributing factor for the Cu seen in the Al layer. Of course this poses the question why the aluminium does not also continually sputter? In fact there is always approximately 5 at% of aluminium in the copper layer, this also could be due to continual sputtering. The fact that the copper would intermix to a far greater extent than aluminium could be due to a number of reasons. Firstly due to the constant substrate rotation speed, the copper target was given a greater power to produce individual layers that were three times as thick as the aluminium. Also copper is a heavier

element and would have more momentum and hence a wider spread in the chamber.

The next priority was to establish whether the copper in the aluminium layer was pure or alloyed. XRD work at BNFL was used to establish this. Figure 5.17 clearly shows pure copper, but has no peaks of aluminium. In fact after studying powder diffraction files, the two small peaks are most likely to relate to $CuAl_2$.

XRD analysis does not provide the same spatial resolution as electron microscopy techniques but can prove one important factor. The sample is still in bulk, and effects of surface oxides can be discounted. Therefore any compositional differences derived from the EDX analysis could suggest that preparation of samples or sample geometry is a major contributing factor, this is considered in Section 6.3.4.3.

#### 6.3.2.2 Cu/Al ML3 Coating (25nm Cu/7nm Al)

Unlike ML2, conventional TEM work on this sample proved difficult due to its small individual layer thickness. However, reasonable success was obtained using selected area diffraction techniques.

Electron diffraction work was used to try and establish the identity of the phases present. The problem with such a method was that the selected area aperture allowed the signal to come from tens of individual layers,

making the pattern much more difficult to solve. However, this highlights the orientation relationship between the layers, as despite the quantity of layers that are contributing to the pattern a strong texture is seen. The copper layers are on average three times the thickness of the aluminium layers and it is therefore not surprising that the copper signal is very intense. Coatings with such periodicity have been reported on occasions to produce satellite spots [77, 85], although it is thought that the intensity of the major copper spots could hide these.

Figure 5.20(a) shows the copper reflections when the beam is parallel to the $[\bar{1}12]$ zone axis. Figure 5.20(b) shows another set of spots that show a strong relationship to the copper spots. These were originally thought to be aluminium. However the inner ring of what would have been Al {111} spots shows six spots which would be disallowed for a face-centred cubic structure. It was then considered that there could be several orientations of aluminium on the same pattern, but then this situation would also be expected for the copper crystallites. However on further inspection the pattern matched to $CuAlO_2$ with the electron beam parallel to the $[\bar{1}11]$ zone axis which also correlated with the high level of oxygen seen in this layer by EDX. In fact oxygen incorporation in the coating made in this way is no surprise since the chamber pressure whilst sputtering the coatings was no better than the order of $10^{-5}$ mbar. In 1992, Makous *et. al.* [84] reported a presence of oxygen in Ni/Mo multilayers. However their analysis by Auger depth profiling is questionable. The Mo signal seems

dampened in the Mo layers where there is a high oxygen signal. This therefore could be due to oxygen accumulating on the surface of the sample in the microscope. More discussion of the incorporation of oxygen is presented in Section 6.3.4, Interactions and Interfaces.

### 6.3.3 EELS of Cu/Al Multilayers

PEELS that proved so successful in the analysis of $TiB_2$ (discussed in Section 6.4) was used to confirm the presence of the copper aluminium alloys, as previously suggested by diffraction and EDX studies. The copper layers in both of the multilayer sets produced Cu L edges as expected, consistent with the literature profiles for pure copper [50, 69].

However, on studying the Cu L-edges taken in the aluminium layer, it is shown that these do not correlate to that which would be obtained from pure copper. This demonstrates that the copper discovered within this layer is in fact alloyed or possibly oxidised.

Not only do the PEELS analyses on these samples divulge information about the state of the copper, it also highlights differences between ML2 and ML3 (by comparing Figures 5.22 and 5.23). Such differences between the coatings were by no means anticipated. In the Literature Review, Chapter 2, many systems studied by different research groups were reviewed. Such work has been centred more on property differences of

multilayer systems with varying individual layer thickness. It is natural to expect that layers made with identical methods should produce identical compositions. For the Cu/Al system studied in this project it is clear, for whatever reason, that they are of differing compositions. It is of course difficult to obtain compositional data from layers when they become very thin such as in ML3; techniques capable of proving this are not readily available to most research groups studying them. The dedicated STEM combined with EDX and PEELS is an ideal tool to achieve such a goal.

The reasons for the compositional differences between the two coatings are not clear. One explanation could be as a result of the processing conditions. It is possible that there were differences between the two processing runs. The importance of the growth parameters on the resulting film, is explained in the processing and microstructure sections of Chapter 2. Rickerby *et. al.*, [19], warned that any slight variation of any of the deposition conditions could have a profound effect on the microstructure and hence the resulting properties.

Another reason could be related to the vastly different rotation speeds of the substrate table. This time dependent part of the process could have affected the overall temperature of the growing film, or the structure formed. More oxygen could have been present in the growth chamber for

ML3. There are so many possibilities, which could only be conclusively proven with many more samples, that further speculation is not justified. However this is a topic for further research but is beyond the scope of this project.

ML2 (Figure 5.22) shows a Cu L-edge comparable to $CuAl_2$ as reported by Sheu *et. al.* [82] (Figure 6.3), this further confirms diffraction and XRD work on this coating.

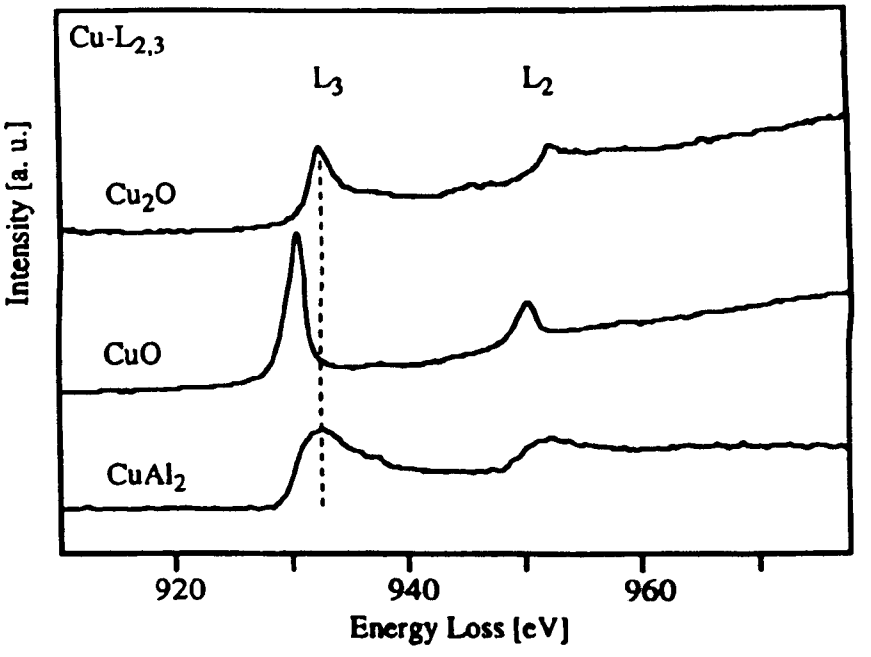


*Figure 6.3: Comparison of Cu L-edges from different compounds [82]*

ML3 however, produces a Cu L edge that is not predominately $CuAl_2$ in nature (Figure 5.23). Such an edge, at present, has not been reported in the literature. However, in comparison with other fingerprints for Cu L

shown above, it can be concluded that the copper in this 'aluminium' layer is also not CuO or $Cu_2O$ due to the lack of strong white lines that are associated with these edges.

In comparing the Cu L edges from the Cu and Al layers, two distinct differences are illustrated in Figure 6.4. The L2 feature seen in pure copper has diminished in the Cu L-edge from the Al layer, and a new strong feature at ca. 937eV becomes apparent.

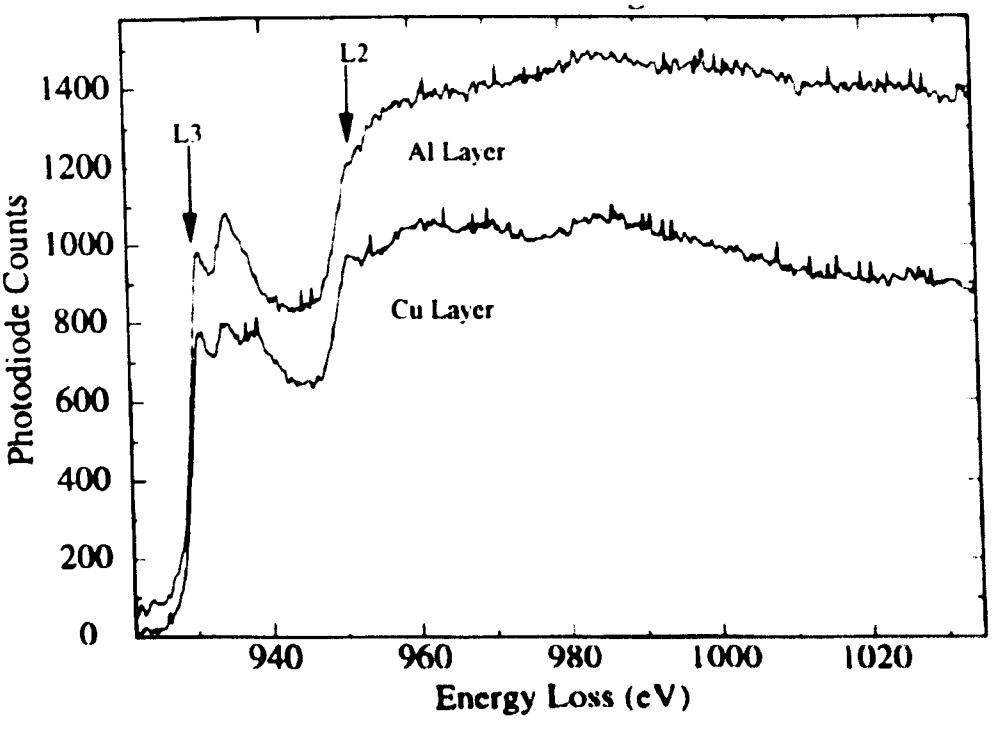


*Figure 6.4: Comparison of the Cu L-edges from the Cu layer and Al layers in ML3*

On consideration of the diffraction work explained previously (Section 6.3.2), it is suggested that this Cu L-edge could be due to the presence of $CuAlO_2$, which poses the question where are the white lines that are

usually associated with other Cu oxides? (Figure 2.21) White lines present in the Cu L-edges from copper oxides are said to be as a consequence of charge transfer from Cu to O. The d-bands that are full in pure copper become partially vacated, allowing transitions to these free states, resulting in strong fine structure peaks [50]. The effect of charge transfer cannot however, describe white line effects seen in $CuAl_2$. One would expect a transfer of charge to occur from aluminium to copper, due to the greater electronegativity of copper. However white lines are still seen in $CuAl_2$, if not as sharp as those seen in the copper oxides. This is thought to be as a result of hybridisation [82]. On consideration of these theories, one would expect in $CuAlO_2$ a transfer of charge from aluminium, which has the lowest electronegativity. However $CuAlO_2$ is a complex structure and charge transfer cannot be the only consideration.

If $CuAlO_2$ is present it poses the question is it just simply a surface effect? Does $CuAl_2$ oxidise to $CuAlO_2$? Firstly, if it does, then surely we would see such an edge for the ML2 coating also. Secondly, why do we not see a presence of copper oxide from the Cu layer if heavy oxidation has taken place? However, the best way of proving beyond doubt that the oxide present is not simply a surface effect is an XRD spectrum. Figure 5.19 shows such a spectrum. Unfortunately, only a copper signal is present, this is most likely due to the small quantities that are being considered and the number of interfaces that are present.

O K-edges were taken at the same time as the Cu-L edges in ML3. Figure 5.24 shows such an edge. On comparison with Figure 2.31 [69] this indicates a possible presence of Cu-O bonds. However, this is not reflected in the Cu L-edges themselves. One would expect the presence of strong, sharp white lines as shown in Figure 2.21. This could imply that there is some association of copper with oxygen, but without free Cu d-bands, possibly as a consequence of bonding with aluminium.

### 6.3.4 Interactions and Interfaces

Unlike the $TiB_2$/Al multilayers the Cu/Al set appeared to have interesting interfaces. Early images (Figures 5.5 and 5.7) seemed to show some kind of zone in-between the layers, initially thought to be a mixing zone. Holleck *et. al.*, [36], also reported interface zones in their multilayers. Setomya *et. al.*, [31] reported that their interfaces between AlN/TiN were incomplete and 'wavy' due to slight interdiffusion of mixing.

Figure 5.15 shows a linescan across the ML2 coating. Consistent with compositional studies, the copper signal is very high within the Al layer, whereas the Al itself is concentrated within its own layer. Sharp peaks of aluminium and oxygen are seen at the interface between the two layers, indicating this region could be an oxide layer. Such a region is ~50-100nm wide in places.

The presence of oxygen is also reflected in linescans from the ML3 coating. In this instance, it is present throughout the entire layer. This oxide layer is unlikely to be a surface oxide on the TEM sample, as the relative amount of oxygen seen with respect to *Al is high. This again* suggests that oxygen has been incorporated within the layer during processing.

All of the coatings were processed in chambers with vacuums no better than $10^{-5}$ Torr. Under such pressures it is quite feasible that all the oxygen in the oxide layers could from within the chamber itself. It is thought that the active surface layer of the growing film is oxidised whilst travelling between one target and the next.

In the ML2 Cu/Al film, the oxide layer has time to grow to ~100nm before reaching the next target. This thick layer is due to the relatively slow substrate rotation speed in this case, allowing time for substantial oxidation. It is thought that the substrate rotation speed is the major factor in determining the oxide layer thickness (assuming similar processing conditions are used).

Even though the substrate rotation speed is much quicker for ML3 coating, the Al layer is so thin (~7nm) that all of it has the time to become oxidised.

In contrast, an incorporation of oxygen is not seen in the $TiB_2$/Al system, even though it too has an aluminium target, and had a far inferior vacuum. This could be due to a number of process dependent reasons, the most likely of which is that the power to one target is switched off whilst the other is sputtering. It is possible that the inactive target acts as a sponge to impurities in the vacuum. Of course, there are many other reasons, such as how long the targets were running before sputtering commences. It is clear that in the Cu/Al case for ML3 that this run up time was not long enough as demonstrated by Figure 5.4, which shows the individual layers, getting progressively thicker.

#### 6.3.3.1 Layer Interactions

The $TiB_2$ multilayer system did not show any evidence of interaction between the layers. Also no reaction zones were seen at the interface. However some caution is needed, as it is clear that the ion milling process has damaged the appearance of such interfaces. This problem was not apparent for the Cu/Al system.

However, the Cu/Al multilayers do seem to interact. This was much more apparent for ML3 and the thickness of the individual layers is thought to be paramount to this effect.

The first compositional data taken on any of the coatings was using TEM on the larger separated ML2 layers. It has been suggested that this coating consists of copper layers sandwiched between $CuAl_2$ layers. An interface zone is seen between the layers, which is thought to be an oxide layer, most probably alumina. There also seems to be a possibility of a higher copper concentration closer to the interface. Of course, the spot size in the conventional TEM is as much as ten times larger than that in the STEM. Hence, any copper signal close to the interface could actually be from the copper layer when using a ~20nm probe.

Over time the Al layer in ML2, seems to have a more even distribution of copper throughout the layer. The last data taken confirms this with a 66wt% Cu level in the layer. The compositional changes that have occurred over time seem to have finally reached an equilibrium at this point. Such changes have evened out any chemical gradient that was present from the higher proportion of copper initially close to the interface.

Interactions in the ML2 coating only seem to be apparent within the Al layer itself, and not between the individual layers. *Interlayer* diffusion could have been prevented by the ~50-100nm oxide layer at the interface.

The thinner ML3 coatings seem to have a more profound interaction. Even though an oxide layer also seems to be present, it is seen throughout the layer. Even so, the total thickness of the Al layer is only ~7nm. This could be thin enough to allow interlayer interactions to occur.

The last data taken from ML3 showed that the levels of copper and aluminium *throughout the whole coating* had levelled out to 75at% Cu/ 25at% Al, irrespective of which layer the analysis came from. This relates to the 3:1 ratio of Cu:Al material which was sputtered in the first place.

Such interactions could have been enhanced by the columnar structure, which is reported to provide fast diffusion paths throughout a coating [21].

Barzen *et. al.*, [39], when studying $Cr_3C_2$/SiC multilayers, highlighted problems with interface structures. This was particularly significant below an individual thickness of 10nm, when comparatively poor mechanical property results were obtained. These poor results, for multilayers with thinner individual thicknesses, is in complete contrast to the majority of research in this area. Such effects were thought to be as a result of the interface zone becoming more significant in such thin layers.

### 6.3.3.2 Interface oxide

Why is the oxide at that is suggested to reside at the multilayer interfaces not more apparent? For example, why is it not detected in the XRD data.

Of course, one could say that this is evidence of an interfacial oxide resulting from surface oxidation. However, it is more likely that detection is beyond the limit of such a technique. It is suggested that there is at least twice the quantity of $CuAl_2$ present in the film over oxide, and the $CuAl_2$ signal is relatively low.

The oxide at the interface is thought to be essential to the interactions that occur between the layers. It is assumed that once the oxide reaches an unknown critical thickness, then interlayer diffusion is greatly reduced. However if the oxide layer is thin enough then it is clear that such layers together in a multilayer film will diffuse across boundaries.

Since the thickness of the oxide layer is thought to be dependent on rotation speed of the substrate table, then it could also be true that when Cu/Al multilayer coatings of this kind are produced below a critical individual layer thickness, interlayer diffusion is likely.

### 6.3.3.3 Effect of Sample Preparation and Geometry

Interactions that have occurred over time have more than likely been accelerated by making them into thin foils, to enable analysis by TEM. Analysing the samples in the STEM has also undoubtedly enhanced this effect. The sample is heated under vacuum, prior to entry into the chamber. This is to minimise contamination of the sample in the near UHV conditions. The temperature reached is estimated at 150 °C for at least 10minutes.

Airlock heating in thermally stable materials is essential in the STEM. Contamination of the sample greatly reduces the resolution of the data, as beam broadening becomes more significant under the growing carbon film on the surface.

On initial consideration of the Cu/Al phase diagram this temperature was considered to be low enough for these samples not to undergo a phase change. However, the effect of diffusion between the layers is still possible, especially since the layers may not be in the lowest energy equilibrium state after deposition. The airlock heating would undoubtedly enhance any movements.

The sample geometry would not have caused the interactions, but greatly accelerated its effect. Such interactions would surely be mirrored in bulk samples if left for a long enough time.

### 6.3.5 Trial DSC experiment.

To try and illustrate the sensitivity of heating over a period of time, a DSC experiment was carried out. Such a technique heats the sample at a specific rate, in this case 10°C/min to 300°C, and compares with a standard sample. The heat flow (W/g) is plotted against the temperature.

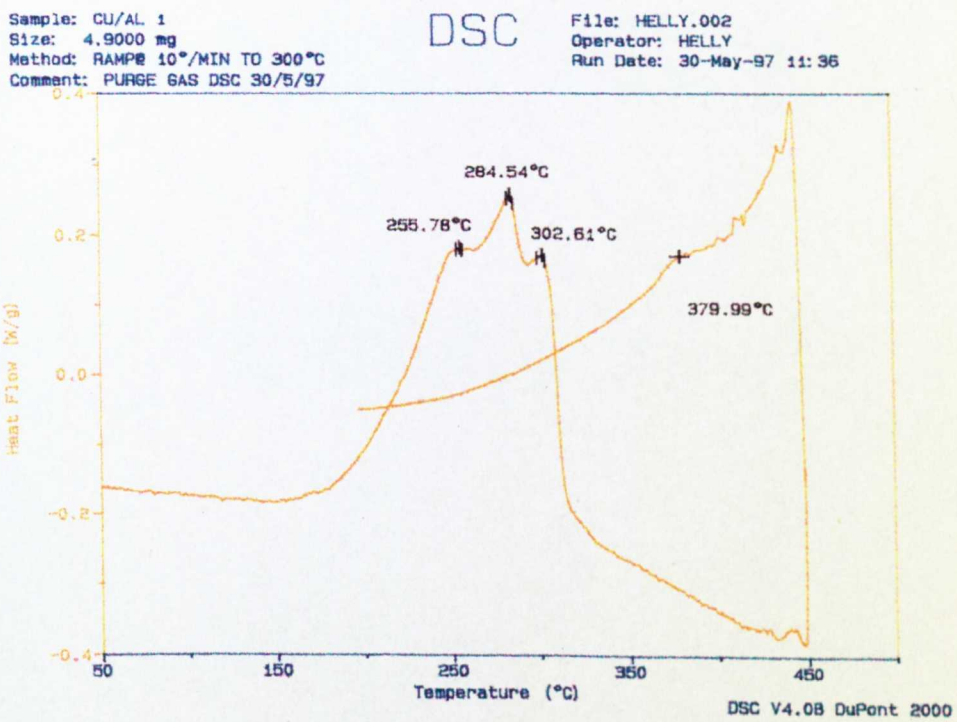


*Figure 6.5: DSC profile of ML2*

The peaks that appear between 255 and 302°C relate to an exothermic energy change, possibly due to a phase transformation. The temperature reaches a maximum of 450°C, however no significant peaks are recorded under the cooling process.

This was just an initial study, but it does prove the instability of ML2 under heating. Such analysis has much scope for further application in future research.

§

## 6.4 PEELS of $TiB_2$

The results of PEELS analysis on $TiB_2$ are discussed in this section. It was thought necessary to dedicate a section on its own, due to the importance of this work. All of the possible effects that could result in B K-edge shape changes in $TiB_2$, are addressed in turn.

### 6.4.1 Effect of Electron Beam Damage

One of the first reasons thought of for the variation in the B K-edge was the effect of the electron beam on the sample. Sauer *et. al.* [53] highlighted the problems with beam damage on boron-containing compounds. Figure 2.25 shows the extent of the effect with increasing electron dose. They found the larger the electron dose, the higher the $\pi^*$ peak is. For their work this was particularly relevant as they were comparing the heights of the $\pi^*$ to $\sigma^*$ peaks, in an attempt to quantify the presence of $BO_3$ relative to $BO_4$. However these samples were minerals and also contained OH groups that could be removed under the heat generated by the probe. Also the $BO_4$ groups were thought to revert to $BO_3$ groups. However, in 1995 Garvie *et al.* [54] reported that anhydrous materials showed minimal damage even after long exposures. From those compounds studied, the majority of compounds were stable enough to analyse for around 10s in a HB5 STEM. For the purpose of this project, the acquisition time was

usually 10secs. However, even when studied for 20secs, as shown in Figure 4.16, no effect on the B K-edge in $TiB_2$ is seen.

For the multilayer sample OH groups are inconceivable, however the incorporation of some oxygen in sputtered $TiB_2$ is very possible. Sauer *et. al.*, [53] showed the presence of a $\pi^*$ sharp peak with trigonally co-ordinated boron oxide.

### 6.4.2 Effect of Ion-Beam Thinning

Compositional analysis, using EDX on the STEM had highlighted the effect of ion milling on the sample, by determining the presence of argon and copper. Of course, some incorporation of argon within the layer could easily occur during the sputtering process. On the other hand this level of Ar was not seen in the Cu/Al layers. Incorporation of Ar in the multilayer would be more expected from an unbalanced method due to the associated ion bombardment of the substrate.

The main difference between the multilayer and the $TiB_2$ standard was that the multilayer had been subjected to, what we have established as heavy ion beam thinning. In order to check that this was not modifying the structure, a thin electron transparent film of $TiB_2$ was made. Figure 4.15 shows the data from this standard; once again a range of fine

structure is produced with features that are more pronounced than in the powder standard, suggesting that the ion beam thinning is not the principal cause of the modifications to the spectra.

### 6.4.3 Effect of Impurity Incorporation

Because ELNES is so dependent on nearest neighbours and bonding, there is a possibility of impurity atoms causing the different spectra. Fig. 4.18 shows a series of X-ray maps of the multilayer coating which indicates that there is oxygen associated with the $TiB_2$ layer. However this result was treated with caution due to the overlap between the oxygen K-edge and the titanium L-edge. Also if oxygen was present it could just be a surface layer.

XRD work (Figure 4.8) confirmed that within the limits of detection, there was only titanium diboride and aluminium present in the multilayer. However, since the B K-edge of trigonally co-ordinated boron oxide gives rise to a $\pi^*$ feature at ca. 194 eV (Sauer *et. al.* [53]) it is important to consider the possibility of oxygen incorporation. The oxygen edges are shown in Figure 4.20. The oxygen/boron ratios remain constant within experimental error and hence the incorporation of oxygen was not considered the major factor in producing variations in the B K-edge in $TiB_2$.

### 6.4.4 Effect of Orientation

Orientation effects in PEELS spectra have been previously studied. These have revealed the sensitivity of $\pi^*$ and $\sigma^*$ features to the orientation of the scattering vector and hence direction of the incident beam. BN is such an example, (Garvie *et. al.* [54]). The relative $\pi^*$ intensity is a maximum for the electron beam perpendicular to the c-axis while the relative $\sigma^*$ intensity is a maximum for an electron beam direction parallel to the c-axis. Large c/a ratios have been thought to be central to such effects [54, 86]. In $TiB_2$ c/a ~1, hence orientation was not initially considered as an important factor.

The ideal study would be to establish what zone axes produce what kind of spectra and why. However, the amount of tilt available in the STEM is limited to 14 degrees (as a compound angle) so a study from chosen zone axes is impossible.

Figure 4.19(a) shows a spectrum from the single crystallite $TiB_2$ sample, that was orientated with the beam along the $<1\bar{2}1\bar{3}>$ direction. Figure 4.19(b) shows the spectrum with the beam tilted several degrees away from the $<1\bar{2}1\bar{3}>$direction. The change in the ELNES between them indicates that there is a dependency of the B K-edge in $TiB_2$ on the orientation of the sample with respect to the electron beam.

It is thought that there are a number of reasons for this effect. Firstly $TiB_2$ has a hexagonal structure like BN, but in contrast to BN consists of monoelemental layers i.e. boron layers sandwiched between layers of titanium in the a-b plane. It therefore has anisotropic bonding within the whole structure, as the bonding within the layers will be different to any interlayer bonding. These differences are very directional and hence it is perhaps not surprising that orientation effects are seen.

However, $TiB_2$ standards in the literature do not show such orientation effects. There could be several reasons for this: Firstly, it is thought that in a polycrystalline fine grained sample of $TiB_2$ any ELNES differences could be averaged out. Secondly, another reason is thought to be due to the combination of a very small STEM probe in a highly textured sample. Finally in the $TiB_2$ {0001} multilayer cross-section, the beam is sampling the a-b planes, or very close to them. Any buckling of the foil could result in slight changes in orientation close to this zone axis, where this effect could be very sensitive.

After initial multiple scattering (MS) simulations [87] the B K-edge from $TiB_2$ was assigned features at ca. 190 eV to transitions to $\pi^*$ states, while features at ca. 195 eV (sharp) and ca. 202 eV (broad) were associated with transitions to $\sigma^*$ states.

McCulloch *et. al.,* [88] reported the sensitivity of the sharp σ* feature in graphite to interlayer correlations. $TiB_2$ is a layered structure (Figure 2.28) and this was thought a possibility for the feature at ca. 195 eV in the B K-edge of $TiB_2$.

### 6.4.5 Theoretical Calculations of the effects of Orientation

Sauer *et. al.,* [53] showed the benefits of theoretical calculations of ELNES. Their calculations showed a good resemblance to the experimental data, with all the major features being predicted. Even though the XANES method of calculation did not have the same success as other calculations such as Gavrie *et.al.,* [54], it does show a clear difference on the spectra orientation dependence.

Initial B K-edge calculations [87] enabled the ELNES in $TiB_2$ to be understood further. This was further extended by Lie *et. al.,* [89], this time calculated using full potential linear augmented plane wave (FLAPW) method. This method has an advantage over the LMTO approach as no shape approximations are made to the potential or charge density. The result is seen in Figure 6.6; Pz relates to c-axis px+py to the a-axis and the top calculation is the combined calculation. It is now thought from this more accurate calculation the first feature in the B K-edge ca. 190eV is possibly not due simply to transitions to π* as originally thought, but a

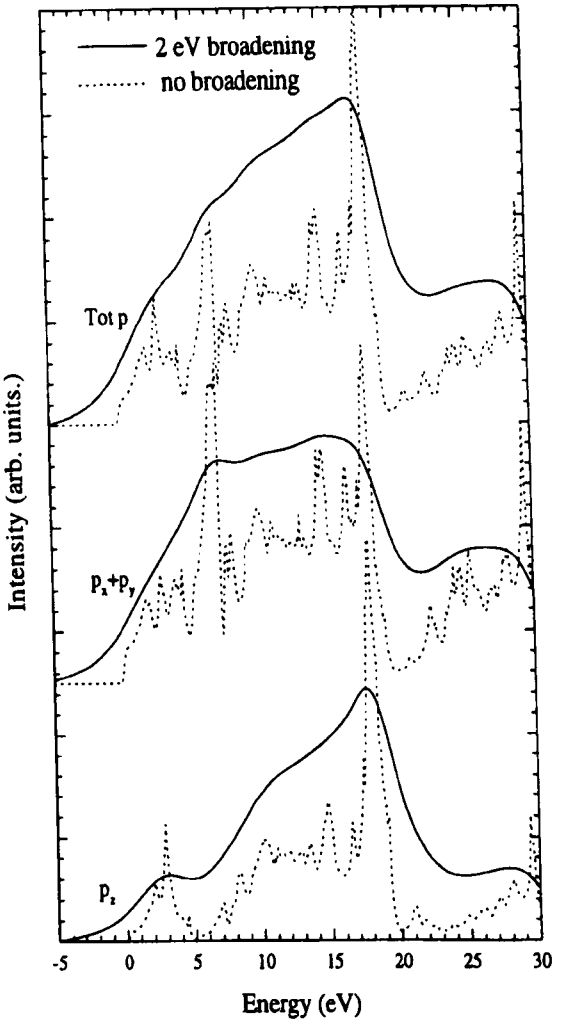


*Figure 6.6: Calculation of the ELNES in B K-edge in $TiB_2$ [89]*

feature due to hybridisation, and possibly a charge transfer between Ti d and $Bp_z$ orbitals. Tain [57] highlighted the importance of the interaction between the titanium and boron atoms and cited the higher melting point and hardness of $TiB_2$ with respect to HCP titanium as evidence. They reported a strong hybridisation of Ti 3d and B 2p states, even though from differing layers, indicating strong interlayer bonding.

The combination of the textured multilayer coating and high spatial resolution PEELS in the STEM analysis has highlighted orientation effects in the B K-edge in $TiB_2$. However it has not been possible to use large enough tilts to compare the edge at the a-axis to the c-axis. This type of experiment has also recently been carried out at Leeds by Lie *et. al.* [89] and the results are shown below in Figure 6.7 (labels A,B,C and D denote the main features)

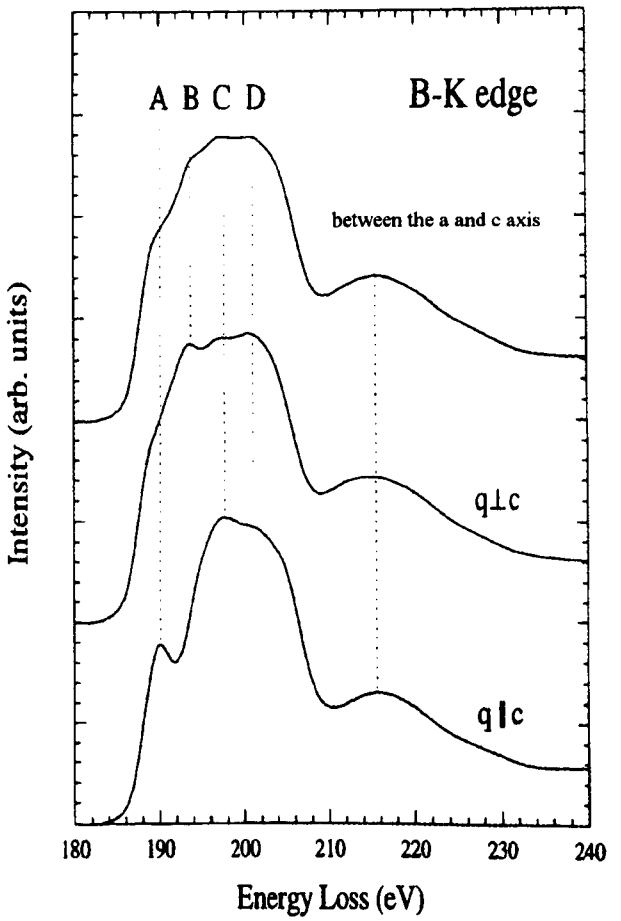


*Figure 6.7: Experimental analysis of $TiB_2$ in a conventional TEM [89]*

The experimental data shown in Figure 6.7 shows a good correlation with the corresponding calculation in Figure 6.6.

It was thought possible at first that channelling effects could also be at least part of the reason that the differences in the B K edge are seen. This was because of the relatively small angles required to produce such changes. However, it is suggested that such a dramatic effect is seen in the STEM analysis due to the texture. When probing along the a-axis with the beam, intense features are seen due to the bonding between the nets several degrees away from this axis, and result in dramatic changes. It would be easy to consider that at the a-axis and the c-axis two extremes are seen and in between it is a combination of the two. It is thought that several orientations in this crystal could result in the pronouncing of certain features and the diminishing of others. The a-axis and c-axis are just two such examples.

The consequences of these results are clear; the sensitivity of the scattering vector to orientation must not be overlooked, even in a sample that previously would not have been considered. This is especially important when comparing details in ELNES in a quantitative manner. The anisotropic nature of the bonding in $TiB_2$ is central to the effects that have

been reported, as is the texture in the film and resolution of the technique used.

§

**6.5 Hardness**

It was beyond the original objectives of the work to carry out any mechanical property analysis on the coatings. However to compare the multilayers it became necessary to compile some data in the form of microhardness testing. A Knoop hardness study was carried out by BNFL on their Cu/Al system. If a coating was to be produced to give hardness improvements relatively soft metals such as copper and aluminium seem a strange choice. The use of at least one very hard material such as $TiB_2$ would perhaps seem a preferred option. However at over £3000 pounds per target $TiB_2$ is an expensive option, especially for trials on different sets of multilayer coatings. Copper and aluminium are relatively cheap, widely available targets and ideal to gain some idea of the effects of lowering the individual layer thickness. Figure 5.25 shows the Knoop hardness data taken by BNFL on five Cu/Al multilayers with different individual layer thickness ranging from ~900nm to as small as 7nm. The two multilayer sets (ML2 and ML3) that microstructural and compositional studies were carried out on are included this data.

The most striking feature of this figure is that one of the coatings (25/7nm Cu/Al) denoted by a square shows at its peak a Knoop hardness of almost 900 $H_k$, as hard as tool steel [79]. This vast improvement of the multilayer over its single layer counterparts is incredible, and has to be viewed with a great deal of scepticism.

However, in 1989 Ruff *et. al.* [32], also saw vastly improved properties in multilayers of Ni/Cu as the individual layer thickness became small. Similar results demonstrating the dependency of properties on individual layer thicknesses have been reported by many others [31, 36, 38].

The hardness of all of the coatings decreases with increasing load. This of course, could be a consequence of a greater influence from the substrate. The 300g load is far too much in most cases, it samples a large quantity of the substrate. This explains why all of the coatings demonstrate similar results for this load. It is thought that when measuring the hardness of a film then the indent should penetrate no deeper than a tenth of the overall thickness to eliminate substrate influences. This is shown in Figure 3.11.

Complying with this criterion, the most reliable data has been obtained using the 50g load. The 25/7nm set still produces a hardness of over 600 Hk.

On consideration of the data obtained with the 50g load a distinct trend is seen. The thinner the individual layer is, the harder the coating seems. Also, there does seem to be a large jump in hardness when the layers became thinner than 100nm. The larger layers i.e. 908/251 and 253/68

perform almost identically throughout the data. For the thinner layers there is a jump in hardness improvement.

Section 2.3.2 highlights the significance of the interface on improvements in properties. Therefore using the data from BNFL the hardness was plotted against the number of interfaces sampled. Figure 5.27 confirms the relationship between the number of interfaces and hardness.

The whole process of hardness analysis on multilayer coatings has many areas where the data could have errors introduced. What is the effect of number of interfaces that are sampled? What is the influence of the substrate? Which layer is on the surface? Such questions led to an experiment to compare plan view hardness tests against cross-section tests. The latter test is unaffected by the substrate and the surface layer. Figure 5.29 shows the results.

Firstly the cross-sectional data produces consistently harder results than that in plan view. This is unusual, on consideration of the columnar microstructure theories, since it has been reported that PVD coatings are significantly harder when tested parallel to their growth direction compared with values derived from the other two orthogonal directions [20]. However, there are reports [30] that an additional factor that must be considered, that the structure of PVD films becomes less dense as it grows outwards. Consequently thicker coatings of otherwise similar material

might be expected to appear softer than thinner coatings since the indentation will be sampling greater porosity [20, 30].

Also as the load increases in both cases the hardness increases. This is thought to be from the effect of the higher number of interfaces that are seen with a higher load. The cross-sectional data has a greater influence from the interfaces, this is thought to be the reason for the slightly higher values obtained.

§

# Chapter 7

## *Conclusions and Further Work*

§

### 7.1 Uniformity

- Uneven interfaces in the $TiB_2$/Al coating are thought to be partly due to the large amount of ion-milling required to produce the TEM specimen. Step-like regions are thought to be created at the interfaces, hence inducing preferential ion milling, which has a detrimental effect on the apparent uniformity.
- ML58 has an irregular individual layer thickness. This is most likely to be due to processing errors and sputtering out of sequence.
- Samples ML3 and ML2 of Cu/Al multilayers have good uniformity and consistency. Continual substrate rotation has helped with this. The $TiB_2$/Al multilayer has less accurate individual layer thickness than the Cu/Al multilayer system. This is thought to be due to the greater amount of automation in latter process.
- Thinner layers are present in ML3 close to the substrate, due to the magnetrons not reaching their optimum power before coating begins.

#### 7.1.1 Further Work and Suggestions

- The $TiB_2$/Al samples would have benefited from ion beam thinning using the PIPS. More samples made in this manner could enable a more accurate measurement of individual layer thickness to be made.
- Production of the $TiB_2$ /Al coatings to be attractive to industry, should have a continuously rotating substrate; for both speed of production and an accurate final product. Comparison of such coatings to the samples studied in this project would be interesting.

### 7.2 Microstructure

- The $TiB_2$ layer in the $TiB_2$ /Al coating exhibited a columnar zone 1 - like structure. The Al layer was also columnar but due to the lack of tapered ends is classified as zone 2.
- Use of PVD models and phase diagrams can only be used as a guide for predicting the existence of specific structures and phases, as little is known or understood about local heating and interactions when coating multilayers.
- ML3 has column features running through many layers in the top region of the film. The increase in width of such features indicates an increasing coating temperature.

#### 7.2.1 Further Work and Suggestions

- Studies on the temperature achieved during the coating process would prove interesting. It would be beneficial to establish whether local heating effects are influenced by the rotation speed of the substrate. If differences are found, then it lead to one explanation of why there are structural and compositional differences between ML2 and ML3.
- Tailoring the deposition conditions to produce an optimum coating would be the ultimate goal. Had more time been available, it would have proved a good study to alter deposition conditions and analyse any changes in layer microstructure/composition. However, this would have to be carried out concurrently with mechanical property tests.

### 7.3 Composition

- The $TiB_2$/Al multilayer consisted of the expected compositions and there was no evidence of interactions between the two sandwiched layers
- The Cu/Al multilayers not only consist of compositions that were unexpected but ML2 and ML3 are different from each other.
- ML2 consists of Cu/$CuAl_2$ rich layers with an interfacial oxide (most probably alumina).
- It is suggested that ML3 consists of Cu/$CuAlO_2$ rich layers, with possibly other phases such as $CuAl_2$
- It is possible that such compositional differences could contribute to the vast improvement in hardness properties seen for ML3 over ML2.
- The presence of some of the copper in the aluminium layers is thought to be as a consequence of continual sputtering during deposition. Oxygen that has been discovered mainly at interfaces, is most likely to be deposited in passing between the targets.
- The formation of $CuAlO_2$ rather than $CuAl_2$ in ML3 could be due to the time the substrate spends spent under the aluminium target. For this coating the rotation speed of the substrate is much quicker that that for ML2.
- The interfacial oxide in ML2 is thought to prevent interaction between layers. However interactions are thought to occur within the aluminium layer itself. It seems that this coating is not in an equilibrium state when deposited.

- The oxide layer in ML3 is very thin, and possibly incomplete in parts, this could have enabled interlayer interactions to occur.
- All interactions in the Cu/Al coatings are likely to have been accelerated, due to the geometry of the TEM sample and the heating encountered in the STEM.

### 7.3.1 Further Work and suggestions

- Cu/Al coatings, to be commercially viable, have to produce a predicted composition. More experiments need to be carried out to prove that different individual layer thicknesses do not have a bearing on the composition/structure obtained.
- More PEELS analysis on ML3 is an area for extensive research. The Cu L-edge obtained for this coating needs to be studied much more to prove beyond doubt what structure that it relates to. This would then lead to studies on the origin of such fine-structure, as with the B K-edge in $TiB_2$.
- Further work needs to be carried out to discover the effect of time and temperature on the coatings. Initial DSC experiments show that there is some scope for experiments in this area. Many more coatings would need to be produced and the phases characterised before and after heating. It would be useful to carry out some in-situ heating experiments in the STEM.

### 7.4 PEELS of $TiB_2$

- The B K-edge in $TiB_2$ is sensitive to the orientation of the sample with respect to the electron beam.
- Extra fine structure features could to be a result of interlayer bonding correlations. Although more recent theoretical calculations suggest an extra feature in the PEELS spectra could be due to due to hybridisation.
- Care must be taken when comparing relative heights of $\sigma^*$ to $\pi^*$ peaks without knowledge of such orientation effects. Orientation effects were not previously thought to effect the B K-edge in $TiB_2$

#### 7.4.1 Further Work and Suggestions

- Further work is currently being carried out by Lie *et al.,* [89] on theoretical calculations of the B-K edge of $TiB_2$ and the origin of fine structure changes.
- Work on hexagonal or other layered materials and their sensitivity to orientation or layering effects would also be a field for further studies.

### 7.5 Hardness Tests

- The $TiB_2$/Al coatings had an overall thickness that was too thin to carry out any hardness data without sampling the substrate.
- The Cu/Al multilayers showed a trend of thinner individual layer thicknesses producing superior results. However, with the differences in composition, described above, this must be viewed with caution, as such data does not compare coatings with individual layer thickness difference as the only variable.

- Initial studies on multilayer coatings tested in cross-section produce even more encouraging results. Error from the influence of the substrate could possibly be less important in such a case. However, care should be taken when analysing columnar films as one could introduce errors due to the anisotropic behaviour of such structures.

### 7.5.1 Further work and Suggestions

Many more samples need to be tested in both plan view and cross-section. A preferred load for analysis and an optimum overall thickness should be determined to achieve better results.

All the samples need to be characterised before comparing different individual layer thickness coatings.

# Chapter 8

## *References*

§

## 8.0 References

[1] D. R. Gabe, *Principles of Metal Surface Treatment and Protection*, (1972) Pergamon Press.

[2] C. Subramanian and K. N. Strafford, *Wear*, 165 (1993) 85-95.

[3] A. Schulz, H.-R. Stock and P. Mayr, *Materials Science and Engineering*, A140 (1991) 639-646.

[4] K. A. Pischow, A. S. Korhonen, M. Adamik and P. B. Barna, *Surf. Coat and Tehcnol.*, 67 (1994) 95-104.

[5] A. A. Voevodin, C. Rebholz, J. M. Schneider, P. Stevenson and A. Mattews, *Surf. Coat. and Technol.*, 73 (1995) 185-197.

[6] S. Dullaire and G. Cliche, *Surf. Coat. and Technol.*, 50 (1992) 233-239.

[7] Chen Fu-Tzao, *Microstructure and Properties of Modified TiN coatings. Ph. D. Thesis* (1994).

[8] R. F. Bunshah, *Deposition Technologies For Films and Coatings*, IBSN: 0-8155-0906-5.

[9] P. J. Kelly, R. D. Arnell and W. Ahmed, *Materials World*, March (1993) 161-165.

[10] B. Window, *Surf. Coat. and Technol.*, 71 (1995) 93-97.

[11] B. Window, *Surf. Coat. and Technol.*, 81 (1996) 92-98.

[12] R. K. Waits, *J. Vac. Sci. Technol.* 15(2), (1978) 179-187.

[13] B. Window and G. L. Harding, *J. Vac. Sci. Technol. A*, 10 (1992) 3300.

[14] B. Window and N. Savvides, *J. Vac. Sci. Technol. A*, 4 (1986) 565

[15] R. D. Arnell, *Surf. Coat. and Technol.*, 59 (1993) 105-109.

[16] Y. Ding, D. O. Northwood and A. T. Alpas, *Surf. Coat. and Technol.*, 62 (1993).

[17] K. J. Lawson, *School of Industrial and Manufacturing Science, Cranfield University, Bedford MK43 OAL.*

[18] J. A. Thornton, *J. Vac. Sci. Technol.*, 11(4) (1974) 666-671

[19] D. S. Rickerby and S. J. Bull, *Surf. Coat. Technol.*,39/40 (1989) 315-328.

[20] P. J. Burnett and D. S. Rickerby, *Thin Solid Films*, 148 (1987) 51.

[21] N. Kumar, M. G. Fissel, K.Pourrezaei, B.Lee and E. C. Douglas, *Thin Solid Films*, 153 (1987) 287.

[22] R. Messier, *J. Vac. Sci. Technol.*, A4 (1986) 490.

[23] B. A. Movachhan and A. V. Demchishin, *Fizika Metyall, 28,* 653 (1969).

[24] J. A. Thornton, *Ann Rev. Mater. Sci., P. 239* (1977)

[25] R. Messier, A. P. Giri and R. A. Roy, *J. Vac. Sci. Technol.*, A2 (1984) 500.

[26] K. H. Muller, *Phys. Rev. B*, 35 (1987) 7906.

[27] K. H. Muller, *Surf. Sci.*, 184 (1987) L375.

[28] D. S. Rickerby and P. J. Burnett, *Thin Soid Films*, 157 (1988) 195.

[29] J. E. Sundgren, *Thin Solid Films*, 128 (1985) 21.

[30] P. J. Burnett and D. S. Rickerby, *Thin Solid Films*, 148 (1987) 41.

[31] M. Setoyama, A. Nakayama, M. Tanaka, N. Kitagawa, T. Nomura, *Surf. Coat. Technol.*, 86-87 (1996) 225-230

[32] A. W. Ruff and N. K. Myshkin, *TriboL, 111* (1989) 156-160.

[33] A. W. Ruff and Z. X. Wang, *Wear, 151* (1989) 259-272.

[34] A. W. Ruff and D. S. Lashmore, *Wear,* 151 (1991) 245-253.

[35] Y. Yang, Z. Zheng, X. Wang, X. Lui, J. G. Han, J. S. Yoon, *Surf. Coat. Technol.*, 84 (1996) 404-408.

[36] H. Holleck and H. Schulz, *Surf Coat. and Technol,* 36 (1988) 707-714.

[37] G. Hilz and H. Holleck, *Mat. Sci. and Eng.*, A139 (1991) 268-275.

[38] E. Quesnel and Y. Pauleau, *Surf Coat. and Technol.*, 62 (1993) 474-479.

[39] I. Barzen, M. Edinger, J. Scherer, S. Ulrich, K. Jung and H. Ehrhardt, *Surf. Coat. and Technol,* 60 (1993) 454-457.

[40] M. Larsson, P. Hollman, P. Hedenqvist, S. Hogmark, U. Wahlstrom, L. Hultman, *Surf. Coat. and Technol.*, 86-87 (1996) 351-356.

[41] R. Hübler, A. Schröer, W. Ensinger, G. K. Wolf, W. H. Schreiner and I. J. Baumvol, *Surf. Coat. and Technol.*, 60 (1993) 561-565.

[42] J. S. Koehler, *Phys. Rev. B.*, 2 (1970) 547-551.

[43] Z. Renji, L. Ziwei, C. Zhouping and S. Qi, *Wear,* 147 (191) 227.

[44] H. Holleck, M. Lahres and P. Woll, *Surf. Coat. and Technol.*,41 (1990) 179-190.

[45] J. S. Jang and C. C. Koch, *Scripta. Metall.*, 24 (1990) 1599-1604.

[46] A. W. Ruff and Z. X. Wang, *Wear, 151* (1989) 259-272.

[47] J. Cawley, J. M. Titchmarsh, L. A. Donohue, *Surf. Coat. Technol.*, 86-87 (1996) 357-363.

[48] C. R. M. Grovenor, H. T. G. Hentzell and D. A. Smith, *Acta Metall.*, 32 (1984) 773-781

[49] H. T. G. Hentzell, B. Anderson and S. E. Karlsson, *Acta Metall.*, 31 (1983) 2103.

[50] R. Egerton, *Electron Energy-Loss Spectroscopy in the Electron Microscope.*

[51] R. Brydson, *ESMA Bullitin*, 21:2 November (1991) 57-68.

[52] C. C. Ahn and O. L. Krivanek, *EELS Atlas, Gatan.*

[53] H. Sauer, R. Brydson, P. N. Rowley, W. Engel and J. M. Thomas, *Ultramicroscopy*, 49 (1993) 198-209.

[54] L. A. J. Garvie, A. J. Craven and R. Brydson, American Mineralogist, 80 (1995) 1132-1144.

[55] D. W. McComb, P. L. Hansen and R. Brydson, *Microscopy, Microanalysis and Microstructures*, 2, (1991) 561-568.

[56] D. D. Vvedensky, D. K. Saldin and J. B. Pendry, *Comput. Phys. Commun.*, 40 (1986) 421.

[57] D. C. Tian and X. B. Wang, *J. Phys.: Condens. Matter*, 4 (1992) 8765-8772.

[58] R. Lohmann, E. Österschulze, K. Thoma, H. Gärtner, W. Herr, B. Matthes, E. Brozeit and K. –H. Kloos, *Mat. Sci. and Eng.*, A139 (1991) 259-263.

[59] K. B. Shim, J. Kwiencinski, M. J. Edirisinghe and B. Ralph, *Materials Characterization*, 31 (1993) 39-46.

[60] A. Worsley, Ph. D. Thesis, Submitted (1996)

[61] L. Wang and R. J. Arsenault, *Phil. Mag. A*, 63 (1991) 121-130.

[62] E. Parthe, *Intermetallic Compounds (New York: Wiley)*, (1967) 212.

[63] F. Laves, *Theory of Alloy Phases (American Society for Metals), (1956).*

[64] J. P. Riviere, P. H. Guesdon, J. Delafond and M. F. Denanot, G. Farges and D. Degout, *Thin Soild Films*, 204 (1991) 151-161.

[65] H. O. Pierson and A. W. Mullendore, *Thin Solid Films*, 117 (1981) 13.

[66] R. F. Bunshah, R. J. Schramm, R. Nimmagadda, B. A. Movachan and V. P. Borodini, *Thin Solid Films*, 40 (1977) 169.

[67] T. Shikama, Y. Sakai, M. Fukutomi and M. Okada, *Thin Solid Films*, 156 (1988) 282.

[68] J. J. Wert and S. J. Oppliger, *Mat. Sci. Technol.*, 8 (1992) 825.

[69] G. Dehm, C. Scheu, G. Mobus, R. Brydson and M. Ruhle, *Ultramicroscopy*, 67 (1997) 207-217.

[70] G. S. Was, J. W. Jones, C. E. Kalnas, L. J. Parfitt and M. Goldiner, *Surf. Coat. Technol.*, 65 (1994) 77-83

[71] J. L. Murray, *Binary Alloy Phase Diagrams*

[72] V. A. Philips, *Acta Metallurgica.*, 23 (1975) 751-767.

[73] Rollason, *Metallurgy for Engineers*, Arnold

[74] S. A. Hackney, *Scripta Metallurgica et Materialia*, 26 (1992) 1125-1130

[75] K. A. Rogers, K. P. Trumble, B. J. Dalgleish and I. E. Reimanis, *J. Am. Ceram. Soc.*, 77 [8] (1994) 2036-2042.

[76] K. T. Jacob and C. B. Alcock, *J. Am. Ceram. Soc.*, 58 [54] (1975) 192-195.

[77] D. B. Williams and C. B. Carter, *Transmission Electron Microscopy*, Plenum Press.

[78] D. Briggs and M. P. Seah, *Practical Surface Analysis*, Vol 1.

[79] Leitz, *Miniload Hardness Teater Handbook.*

[80] H. K. Schmid, *Micros. Microanal. Microstruct.*, 6 (1995) 99-111.

[81] EMS http:\\cimewww.epfl.chl\

[82] C. Scheu, G. Dehm, M. Ruhle, *In Press.*

[83] A. E. M. De Veirman, F. J. G. Hakkens and A. G. Dirks, *Ultramicroscopy*, 51 (1993) 306-315.

[84] J. L. Makous, R. T. Lareau, S. M. Hues, *Thin Solid Films*, 216 (1992) 259-267.

[85] K. P. G. Leifer, *Ph. D. Thesis* (1997)

[86] H. J. Davock, G. J. Tatlock, R. Brydson, K. J. Lawson and J. R. Nicholls, *Electron Microscopy and Analysis Group Conf. EMAG97 (1997)*

[87] R. Brydson, *University of Leeds*, unpublished work.

[88] D. G. McCulloch and R. Brydson, *J. Phys.: Condens. Matter*, 8 (1996) 3835-3841.

[89] K. Lie, R. Brydson, H. Davock, *In press*

## APPENDIX 1

Estimation of predicted structural zone models as Thornton [14]
As the function:

$T/T_m = x$

where T = Substrate temperature (K)
$T_m$ = Melting temperature of coating material (K)
X= The value of this number gives an indication of the predicted zone when compared to Thorntons model

| Coating Material | Melting Temp | |
|---|---|---|
| | °C | K |
| $TiB_2$ | 3225 | 3498 |
| Al | 660 | 933 |
| Cu | 1085 | 1358 |
| $CuAl_2$ | 590 | 863 |

*Nil Satis Nisi Optimum*

§